Results of the LIVE-L3A Experiment

X. Gaus-Liu, B. Fluhrer, A. Miassoedov,
T. Cron, J. Foit, S. Schmidt-Stiefel, T. Wenz

KIT Scientific Publishing

X. Gaus-Liu, B. Fluhrer, A. Miassoedov, T. Cron, J. Foit,
S. Schmidt-Stiefel, T. Wenz

Results of the LIVE-L3A Experiment

Karlsruhe Institute of Technology

KIT SCIENTIFIC REPORTS 7542

Results of the
LIVE-L3A Experiment

by
X. Gaus-Liu
B. Fluhrer
A. Miassoedov
T. Cron
J. Foit
S. Schmidt-Stiefel
T. Wenz

Institut für Kern- und Energietechnik
Programm Nukleare Sicherheitsforschung

Abstract

The sequence of a postulated core melt down accident in the reactor pressure vessel (RPV) of a pressurised water reactor (PWR) involves a large number of complex physical and chemical phenomena. The main objective of the LIVE program is to study the core melt phenomena during the late phase of core melt progression in the RPV both experimentally in large-scale 3D geometry in supporting separate-effects tests and analytically using CFD codes in order to provide a reasonable estimate of the remaining uncertainty band under the aspect of safety assessment.

The main objective of the LIVE-L3A experiment was to investigate the behaviour of the molten pool and the formation of the crust at the melt/vessel wall interface influenced by the melt relocation position and initial cooling conditions. The test conditions in the LIVE- L3A test were similar to the LIVE-L3 test except the initial cooling conditions. In both tests the melt was poured near to the vessel wall. In the LIVE-L3 test the vessel was initially cooled by air and then by water; in the LIVE-L3A test the vessel was cooled by water already at the start of the experiment.

The information obtained in the test includes horizontal and vertical heat flux distribution through the RPV wall, crust growth velocity and dependence of the crust properties on the crust growth velocity and cooling conditions. Supporting post-test analysis contributes to the characterization of solidification processes of binary non-eutectic melts. The results of the LIVE-L3 and LIVE-L3A tests are compared in order to characterize the impact of transient cooling condition on the crust solidification characteristics and melt pool behaviour including interface temperature, time to reach thermal hydraulic steady-state and the steady-state heat flux distribution.

The report summarizes the objectives of the LIVE program and presents the main results obtained in the LIVE-L3A test compared to the LIVE-L3 test.

Zusammenfassung

Der Ablauf eines hypothetischen Kernschmelzunfalls in einem Reaktordruckbehälter (RDB) eines Druckwasserreaktors (DWR) beinhaltet eine große Anzahl komplexer physikalischer und chemischer Phänomene. Das Hauptziel des LIVE Programms ist es, das Verhalten der Kernschmelze während der späten Phase der Kernzerstörung und –verlagerung im RDB sowohl experimentell in großem 3-dimensionalen Maßstab und in begleitenden Einzeleffekt-untersuchungen als auch analytisch mit CFD Codes zu untersuchen. Dadurch soll eine bessere Einschätzung der Bandbreite der verbleibenden Unsicherheiten unter dem Aspekt der Sicherheitsbewertung ermöglicht werden.

Das Hauptziel des LIVE-L3A Versuches war die Untersuchung des Verhaltens eines Schmelzesees und der Krustenbildung an der Kontaktfläche Schmelze/Wand, worauf die Position des Eingusses und die anfänglichen Kühlungsbedingungen Einfluss haben. Die Versuchsbedingungen waren ähnlich zu denen des Versuches LIVE-L3, es herrschten jedoch unterschiedliche anfängliche Kühlungsbedingungen. In beiden Versuchen wurde die Schmelze in der Nähe der Behälterwand eingegossen. In LIVE-L3 wurde die Behälterwand jedoch anfänglich durch Luft gekühlt und erst später durch Wasser, in LIVE-L3A wurde hingegen die Behälterwand von Anfang an durch Wasser gekühlt.

Die aus den Experimenten gewonnenen Informationen beinhalten Wärmestromverteilungen durch die Behälterwand, Wachstumsgeschwindigkeit der Kruste und Abhängigkeit von Krusteeigenschaften von der Wachstumsgeschwindigkeit und den Kühlungsbedingungen. Begleitend wurden Nachuntersuchungen der Kruste zur Charakterisierung des Erstarrungsprozesses der binären nicht-eutektischen Schmelze durchgeführt. Der Vergleich der Ergebnisse von LIVE-L3 mit LIVE-L3A zeigte den Einfluss der transienten Kühlungsbedingungen auf die Charkteristik der Kruste-Erstarrung, auf das Verhalten des Schmelzesees einschließlich der Kontakt-Temperaturen, auf die Zeit bis zum Erreichen eines stationären hydraulischen Zustandes und die Zeit bis zu Erreichen stationärer Wärmeströme.

Der vorliegende Bericht fasst die Ziele des LIVE Versuchsprogramms zusammen und präsentiert die wichtigen Ergebnisse von LIVE-L3A, verglichen mit LIVE-L3, auf.

TABLE OF CONTENTS

LIST OF TABLES

LIST OF FIGURES

vi

1 Introduction

The behavior of the corium pool in the lower head is still a critical issue in the understanding of Pressurized Water Reactors (PWR) core meltdown accidents. A number of studies have already been performed to pursue the understanding of a severe accident with core melting, its course, major critical phases and timing, and the influence of these processes on the accident progression. The thermal behavior of a single-phase melt pool during steady-state can be well modeled by now [1-3]. However, uncertainties still exist in the description of the transient melt behavior, such as e.g. formation and growth of the in-core melt pool, characteristics of corium arrival in the lower head, and molten pool behavior after the debris re-melting, which are plant and accident sequence dependent [4].

These phenomena have a strong impact on a potential termination of a severe accident. It is therefore necessary to study the core melt phenomena both experimentally and analytically to provide a reasonable estimate of the remaining uncertainty band in regard to safety assessment.

To complement the experimental data on melt pool behavior in the vessel lower head Karlsruhe Institute of Technology (KIT) performs large-scale tests in the LIVE program [5], [6]. The LIVE tests are designed to investigate the core melt behavior in the lower plenum of the reactor pressure vessel and the influence of the cooling of the vessel outer surface with water in the conditions that may occur during core meltdown accident in PWRs [7]. To simulate the corium melt a non-eutectic binary mixture of sodium nitrate $NaNO_3$ and potassium nitrate KNO_3 is used.

The information obtained from the LIVE experiments includes the melt temperature evolution during different stages of the test, the heat flux distribution along the reactor pressure vessel wall in transient and steady-state conditions, the crust growth velocity and the influence of the crust formation on the heat flux distribution along the vessel wall. In the post-test analysis crust thickness profile along the vessel wall, the crust composition and the morphology are determined.

Complimentary to other international programs with real corium melts, the results of the LIVE activities provide data for a better understanding of in-core corium pool behavior. The experimental results are being used for the development of mechanistic models for the description of in-core molten pool behavior and their implementation in the severe accident codes like ASTEC.

2 LIVE-L3A test design

2.1 Test facility description

The LIVE test facility consists of 3 main parts: the test vessel with cooling system, the volumetric heating system and a separate heating furnace. All parts of the LIVE test facility are arranged in a scaffold having three levels. On level 0 (the floor of the experimental hall), all signal cables come together in different control cabinets. Here the measurement signals are collected and transmitted to the control room which is located next to the experimental hall. In the control room, the data acquisition system and online monitoring systems are arranged. On level 0, also the power supply of the heating system and the corresponding hardware to control the heating system is located.

On level 1, the LIVE test vessel is positioned. The LIVE test vessel is a 1:5 scaled RPV of a typical pressurised water reactor (PWR). For the first and second phase of the LIVE experimental program, only the hemispherical bottom of the RPV is used (Figure 1). The inner diameter of the test vessel is 1 m and the wall thickness is ~ 25 mm. The test vessel is fabricated from stainless steel. To investigate the influence of different external cooling conditions on the melt pool behaviour, the test vessel is enclosed by a second vessel (cooling vessel) to be able to cool the test vessel at the outside. The cooling water inlet is located at the bottom of the cooling vessel and the outlet is positioned at the top of the vessel.

Figure 1: LIVE test vessel with volumetric heating system.

The volumetric heating system located in the LIVE test vessel is also shown in Figure 1. More details on the heating system are given in the section 2.3.

The top of the LIVE test facility just before the start of a test is shown in Figure 2. The LIVE test vessel and the cooling vessel are installed on three steel beams and are enclosed by an insulation layer. The test vessel is covered with a lid at the top. The lid consists of a layer of 102 mm insulation material surrounded by 20 mm stainless steel plate at the top and 1 mm stainless steel at the sidewall and the bottom of the lid. Additionally, there is a 1 mm shield plate mounted 5 mm below the insulation layer to protect the lid from the radiation of the hot melt (Figure 3).
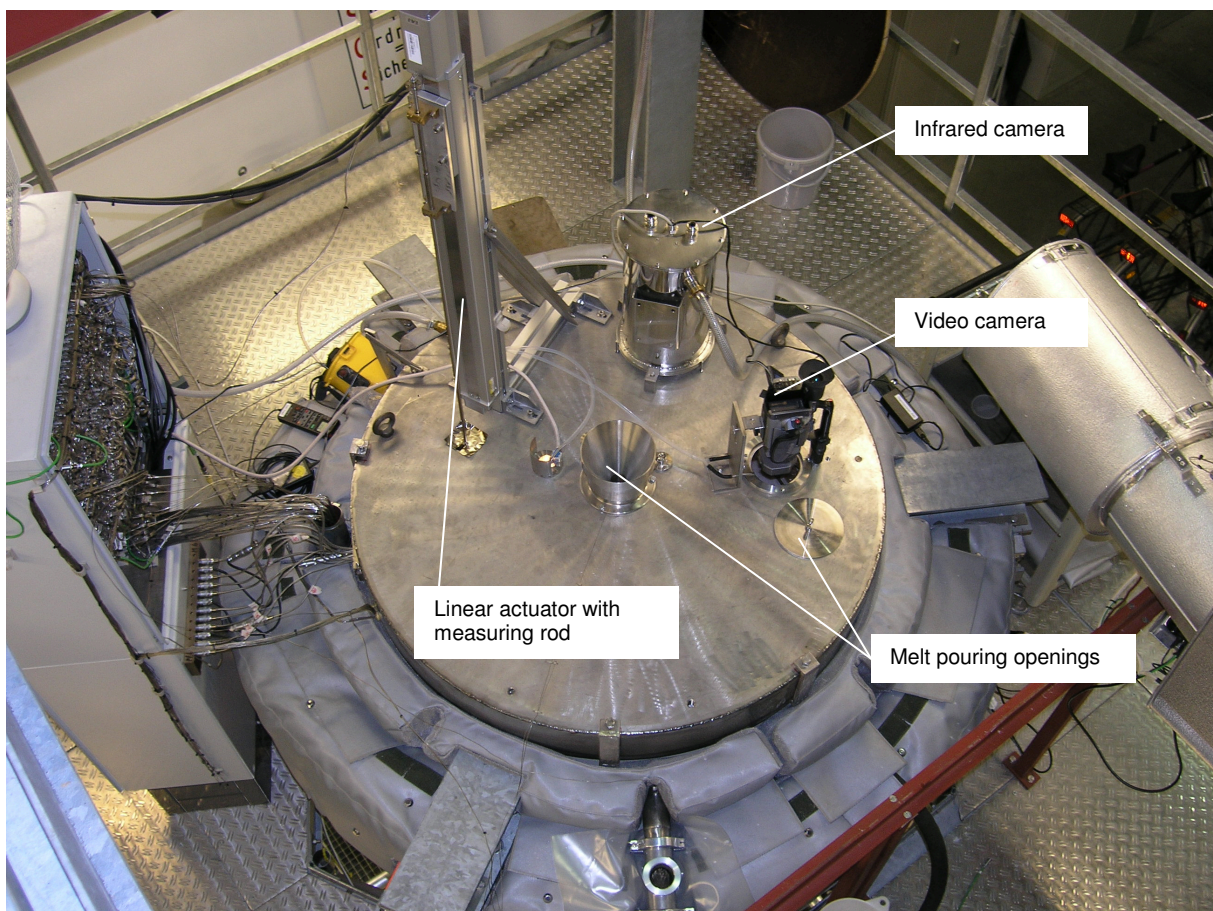
Figure 2: Top view of the LIVE test vessel before the start of the test.

The lid has several openings. There are two melt pouring openings to allow pouring of the melt either centrally or close to the sidewall of the lower head. The pouring position near the wall is located at the polar angle of 65.5°, and the azimuth angle between 112.5° and 202.5°. There are different small openings to light up the vessel or to take melt samples during the test. These small openings can also be used for the crust detection system. Additionally there are two openings for video observation of the melt surface. The atmosphere between

the melt surface and the upper lid is filled with nitrogen. The flow rate of nitrogen flushing is 2 l/min.
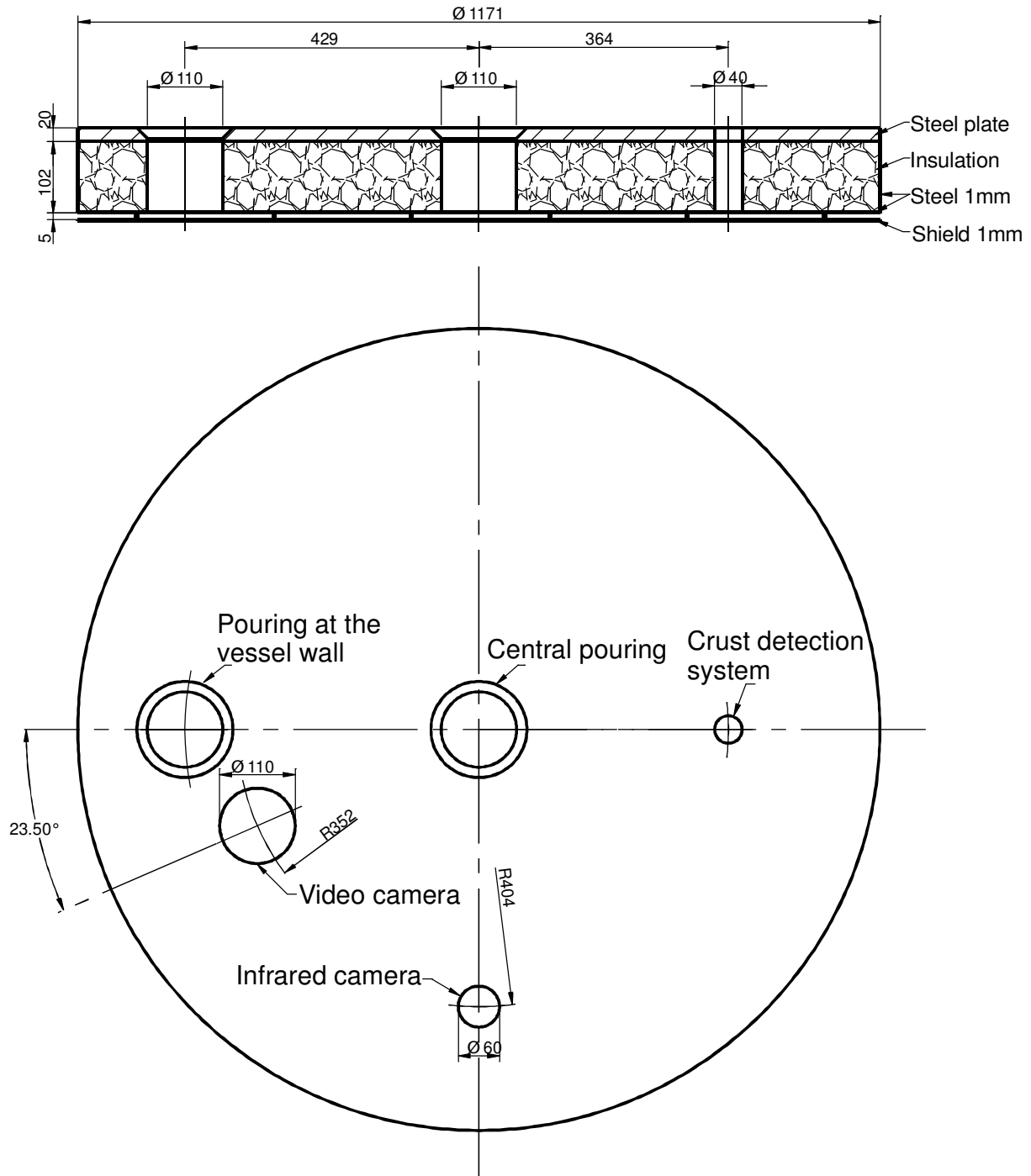
Figure 3: Scheme of the insulation lid.

To allow transient pouring of the melt into the test vessel, the melt is produced in the external heating furnace (Figure 4). The capacity of this tilting furnace is 220 l. If scaled to reactor case, this amount corresponds to the most conservative core melt down situation with 100%

anticipated melting of the core inventory including both oxidic and metallic components [8]. The maximum temperature of the heating furnace is 1100 °C. The heating furnace is mounted on a lifting device and is controlled independently in a separate scaffold, which is integrated into the scaffold of the test facility. During the pouring process the furnace can be tilted and moved upwards at the same time so that the pouring orifice always remains at the same position.

charging orifice

pouring orifice

Figure 4: Heating furnace for melt generation.

When the melt reaches the desired temperature, the furnace is tilted and the melt is discharged with a specified pouring rate into the test vessel via a heated pouring spout. The amount of the discharged melt is defined by the tilting angle and the melt mass flow rate depends on the tilting velocity. There are two pouring spouts available for the melt pouring either centrally or near the vessel wall, as shown in Figure 5. In addition, the heating furnace is equipped with a vacuum pump; so it is possible to extract the residual melt out of the test

vessel back into the heating furnace at the end of the experiment to uncover the crust formed during the test. In this way, the crust thickness profile and the total mass of the crust can be measured after the test. The atmosphere in the heating furnace is filled with nitrogen during the melt preparation.

The control panel of the heating furnace is installed at level 2 of the LIVE test facility. From this level the heating furnace is charged with melt components.
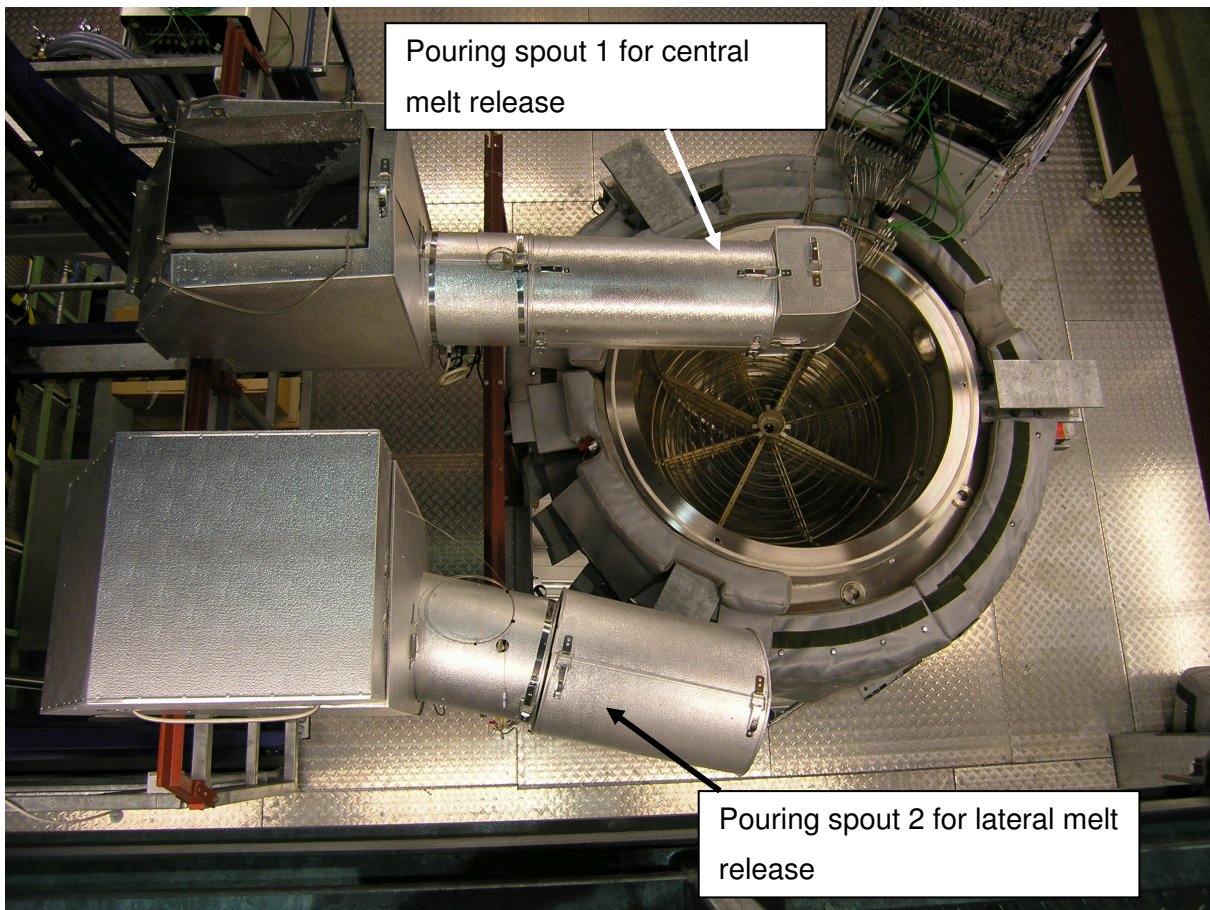
Figure 5: Top view of the LIVE test vessel with two pouring spouts.

2.2 Melt composition and melt generation

2.2.1 Selection of simulant materials

Simulant materials used in the LIVE program should, to the possible greatest extent, represent the real core materials in important physical properties and in thermo-dynamic and thermo-hydraulic behaviour. Therefore, the applicability of several binary melt compositions as a simulant for the oxidic part of the corium has been investigated. Important criteria for the selection are that the simulant melt should be a non-eutectic mixture of several components with a distinctive solidus-liquidus range of about 100 K, and that the simulant melt should have similar solidification and crust formation behaviour as the oxidic corium. Moreover, the

7

simulant melt should not be toxic and aggressive against steel and vessel instrumentation. And finally, the temperature range of the simulant melt should not exceed 1000 °C distinctively because of the technical handling and the selection of the volumetric heating system and the heating furnace.

For the first series of experiments a binary mixture of sodium nitrate $NaNO_3$ and potassium nitrate KNO_3 is used. However, since nitrate salts are soluble in water, the applicability of such melts is restricted to dry conditions inside the test vessel. The eutectic composition of this melt is 50-50 mole% and the eutectic temperature is 225 °C [9]. The maximum temperature range between solidus and liquidus is ~60 K and corresponds to a 20/80 mole% $NaNO_3$-KNO_3 mixture. This melt can be used in a temperature range from 224 °C (solidification) to 370 °C (chemical decomposition). Figure 6 shows a cited phase diagram from [10]. Although mixtures of KNO_3 and $NaNO_3$ are often used as a corium melt simulant in nuclear engineering, the exact phase diagram, especially the position of the solidus line, is still under discussion [14]. Therefore, the liquidus temperatures of this simulant with the heating up method was measured at KIT. The measured liquidus temperatures from 100% KNO_3 to 50 mole% KNO_3 / 50 mole% $NaNO_3$ are given in Table 1. The liquidus temperatures of the 20/80 mole% $NaNO_3$-KNO_3 composition from our measurements amounted to 284 °C [5].
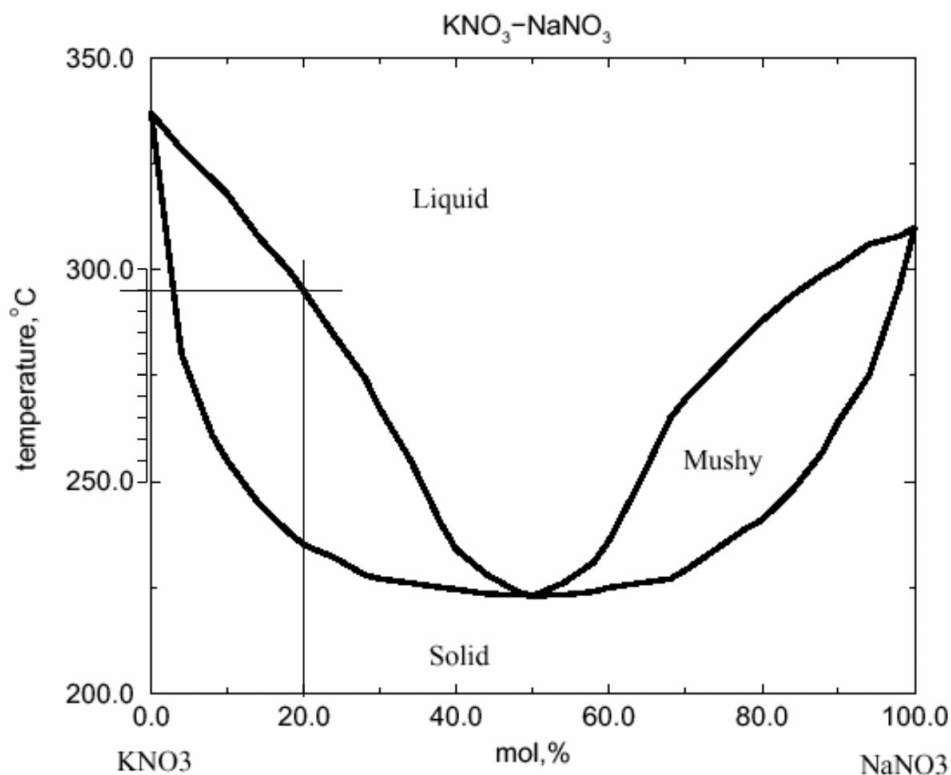
Figure 6: KNO_3-$NaNO_3$ phase diagram given in the reference [10].

Table 1: Liquidus temperature of KNO_3-$NaNO_3$ mixture (100 mole% to 50 mole% range).

KNO_3 mole%	Liquidus °C	KNO_3 mole%	Liquidus °C
50	223.8	76	275.2
52	223.7	78	278.0
54	224.4	80	284.4
56	227.2	82	290.1
58	231.4	84	297.8
60	236.7	86	300.7
62	240.4	88	306.0
64	245.0	90	310.1
66	250.0	92	314.2
68	253.5	94	319.0
70	258.3	96	324.1
72	262.2	98	328.5
74	267.9	100	336.0

2.2.2 Melt composition, preparation and generation

The non-eutectic 20/80 mole% $NaNO_3$-KNO_3 melt was used in the LIVE-L3A experiment. The melt characteristics are described In Table 2. For the melt preparation, the residual melt of the previous experiment LIVE-L4, which used the same melt composition, was recycled. At the end of the test LIVE-L4, the residual melt in the test vessel was extracted from the test vessel back into the heating furnace. The composition of the residual melt was not identical to the original melt composition due to crust formation in the test vessel. The crust remains in the test vessel and is normally enriched in KNO_3, the high melting temperature component of the melt. So the composition of the residual melt has to be determined. Moreover, only part of the melt generated in the furnace was poured into the test vessel during the LIVE-L4 test. Therefore, two melt samples were taken, one at the beginning of the test from the pouring spout and the other one from the melt pool just before the melt extraction from the test vessel. Analysis of these melt samples and known mass of the residual melt in the heating furnace allowed to determine the values of $NaNO_3$ and KNO_3 additives needed to obtain the desired 20/80 mole% $NaNO_3$-KNO_3 melt composition. The determination showed that 8.16 kg of $NaNO_3$ and 38.84 kg of KNO_3 had to be added to achieve the desired total mass of 392 kg or 210 l of the melt respectively in the heating furnace.

Table 2: Melt characteristics and preparation.

Type	NaNO$_3$	KNO$_3$
Mole %	20%	80%
Mass %	17.37%	82.63%
Mass	68 kg	324 kg
Total mass	392 kg	
T$_{liquidus}$	284 °C	
T$_{solidus}$	224 °C	
Loading of the furnace	~455 l powder (for T=20 °C) ~210 l melt (for T=350 °C)	
Pouring mass	120 l (corresponds to ~31 cm melt height)	
Initial temperature	350 °C	
Flow rate of nitrogen flushing	2 l/min	

After loading of the heating furnace, the mixture was heated up for about 3 days to a temperature of 350 °C before the test initiation and was kept at this temperature until the start of the experiment. During this time the atmosphere in the heating furnace was flushed with nitrogen at 2 l/min to avoid the chemical decomposition of the melt.

2.3 Decay heat simulation

The volumetric heating system has to simulate the decay heat released from the corium melt. Consequently, the heating system has to produce the heat in the melt as homogeneously as possible. Therefore a heater grid with several independent heating elements was constructed, as shown in Figure 7. The heating elements consist of shrouded electrical resistance wires. The maximum design temperature of the heating system is 1100 °C. To allow a quasi-homogeneous heating of the melt pool, the heating system has six heating planes at different elevations with a distance of about 45 mm. Each heating plane consists of a spirally formed heating element with a distance of ~40 mm between each winding. The heating elements are located in a special cage to ensure the correct positioning. To realise a quasi-homogeneous heating of the melt, each plane is controlled separately.

The power, which the heating coil of each plane can provide, is determined by the length of the heating wire, the corresponding resistance and the supplied voltage. For the dimensioning of the heating system, an input supply voltage of 230 V was assumed. However, the voltage measured at the heating elements varies from 209 to 211 V so that the total maximum power of all heating planes amounts to 24.5 kW [5].
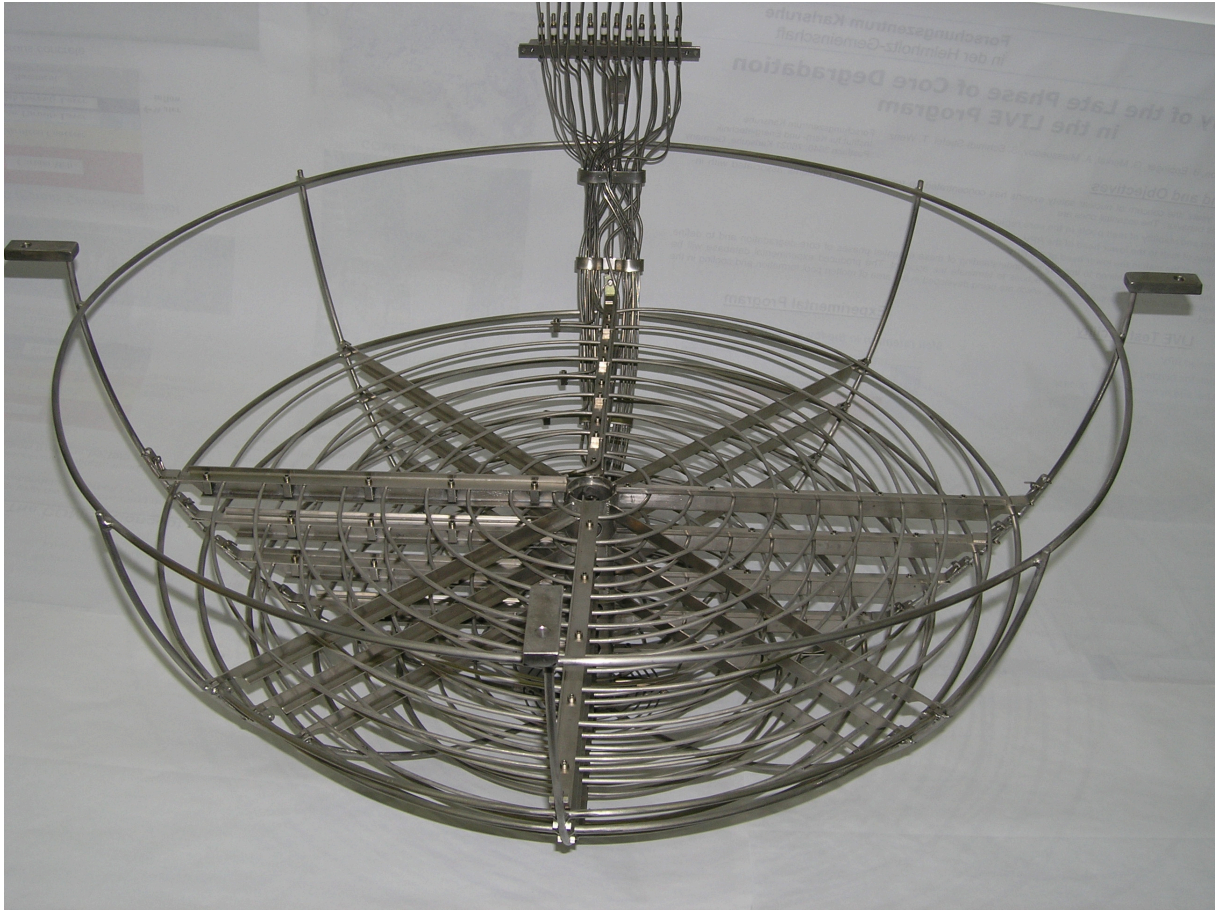
Figure 7: LIVE volumetric heating system.

The maximum power of the heating planes is given in Table 3 as an average value determined by different measurements. The vertical position of the heating planes in the test vessel is also given, related to the bottom of the test vessel. For the quasi-homogeneously heating of the melt the maximum heating power is limited to about 18.5 kW.

Table 3: Characteristics of the LIVE heating system.

Heating plane	Distance of the heating planes to the test vessel bottom, mm	Diameter of the heating elements, mm	Maximum power measured during commissioning, W
6	36.4	2	1080
5	90.4	3	2338
4	135.4	4	2715
3	182.4	4	6624
2	233.4	4	6407
1	278.4	4	5300
			Σ 24464

Before the test LIVE-L3A, the heating plane 4 was replaced because of the damage during the previous test. The new heating plane provides a comparable maximum power as the previous one.

To control the heating system and to avoid overheating of the heating elements, two monitoring thermocouples are installed at each heating element: one at the outer region and the other one at the inner region of the heating element coil. The power automatically switches off when the temperature exceeds 380 °C to avoid the overheating and chemical decomposition of the melt.

The heating system is controlled by a separate PC control system, which is independent from the PC data acquisition system. The programme Visual Designer 4.0 is used to store and to display the data of the heating system. Here, the actual performance of the heating system and also the temperature of the monitoring thermocouples are stored.

2.4 Facility instrumentation and data acquisition

The LIVE test facility is extensively instrumented to monitor and control the experiment and to collect data for subsequent evaluation. In Figure 8 a scheme of the LIVE test vessel with some instrumentation is shown. All data is stored on a PC data acquisition system running under the Visual Designer 4.0.

To measure the temperature at the inner and outer surface of the vessel wall, 17 thermocouples are installed at five levels and along 4 azimuth angles at 22.5°, 112.5°, 202.5° and 292.5° on the inner wall surface (named IT) of the test vessel and 17 thermocouples at the same positions on the outer wall surface (named OT) of the test vessel. The position of the IT and OT thermocouples is given in the Figure A-3 in the Annex A.2. Temperatures measured at these locations are used to calculate the heat flux through the vessel wall.

Furthermore, 36 thermocouples are positioned in the melt pool to measure the melt pool temperatures at different positions (named MT). The position of the MT thermocouples is given in the Figures A-5 and A-6 in the Annex A.2. The thermocouples are uniformly distributed in the melt at a distance of 100 mm in horizontal and vertical direction between each other. The thermocouples are mounted at the cage of the volumetric heating system.
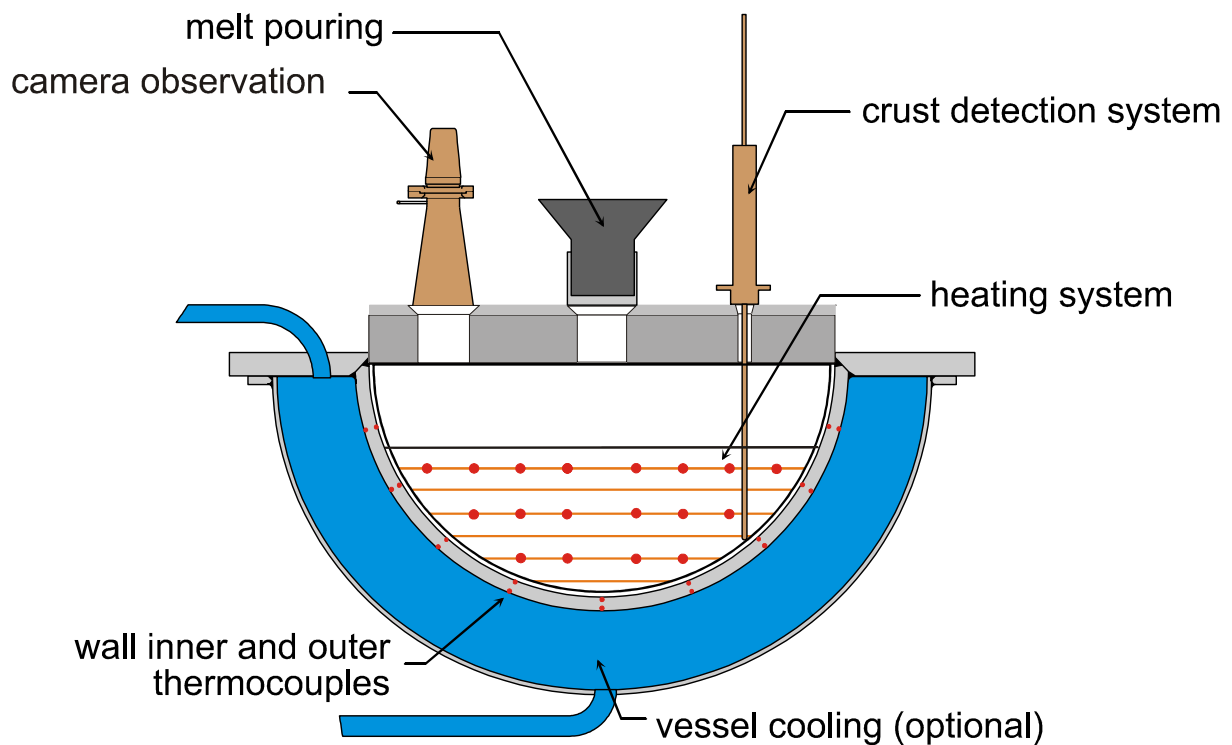
Figure 8: Scheme of the LIVE test vessel with some instrumentation.

To quantify the crust growth at the vessel wall/melt pool interface three thermocouple trees were installed. The thermocouple trees were attached at the inner vessel wall along the azimuth angle of 35°. Each thermocouple tree consists of 7 thermocouples, which are arranged parallel to the vessel wall. For the first thermocouple tree CT4, which is located at the most lowest point, 100 mm above the bottom of the test vessel, the distance of the thermocouples from the inner vessel wall into the melt is 0, 9, 18, 27, 36, 45, 54 mm. For the other two thermocouple trees CT2 and CT3, which are positioned 200 and 300 mm above the vessel bottom of the test vessel respectively, the distance of the thermocouples from the inner vessel wall is 0, 3, 6, 9, 12, 15, 18 mm. Here the distance between the thermocouples is smaller comparing to the first thermocouple tree, since thinner crust growth is expected at these positions.

In addition, several video systems are installed to observe the pouring process and the behaviour of the melt surface during one experiment. They include:

- a conventional video camera directed from the upper lid of the test vessel onto the surface of the melt;
- an infrared (IR) video camera directed from the upper lid of the test vessel onto the surface of the melt, viewing through a ZnSe window on the surface of the melt near the vessel wall. The view area of the camera is 22x17 cm. This camera operates in

the IR wavelength range from 7.5 to 13.0 µm and produces a real-time infrared re-cording with a frequency of 0.25 s to 5 s according to the needs of the experiment. Motion pattern and flow velocity at the melt surface can be recorded by the IR cam-era;

- a video camera installed at the side of the test vessel. With this camera, the pouring process of the melt can be observed in more detail.

Decay power input in the melt is recorded and melt samples are extracted during each test. Different openings in the upper lid of the test vessel allow pouring of the melt to the central region or close to the sidewall of the lower head. To be able to investigate the crust, which is formed at the wall of the vessel, the residual melt is extracted out of the vessel at the end of the test.

The melt pool vertical temperature profile and the boundary temperature at the melt/crust interface can be measured by the crust detection system. The crust detection system con-sists of a linear actuator and a measuring lance. The linear actuator is mounted on the lid of the test vessel. The measuring lance is attached to the linear actuator. The lance can be driven at 0.1 mm accuracy. The position of the crust detection system on the lid is at radius 365 mm and azimuth angle 340°.

At the bottom of the lance 5 thermocouples are installed. The distance between each ther-mocouple is 5 mm. When the measuring lance touches the crust front, the temperature of the lowest thermocouple remains at a constant level. In this way the boundary temperature and the position of the crust can be measured. By moving the lance stepwise, the thickness of the thermal boundary and the temperature gradient within the boundary layer ahead of the crust can be determined. A picture of the crust detection system mounted on the lid of the test vessel is shown in Figure 9.

At the outer surface of the cooling tank three thermocouples are installed to measure the temperature between the cooling tank and the insulation layer.

All the details on the channel assignment and the instrumentation of the facility are given in the Annex A.
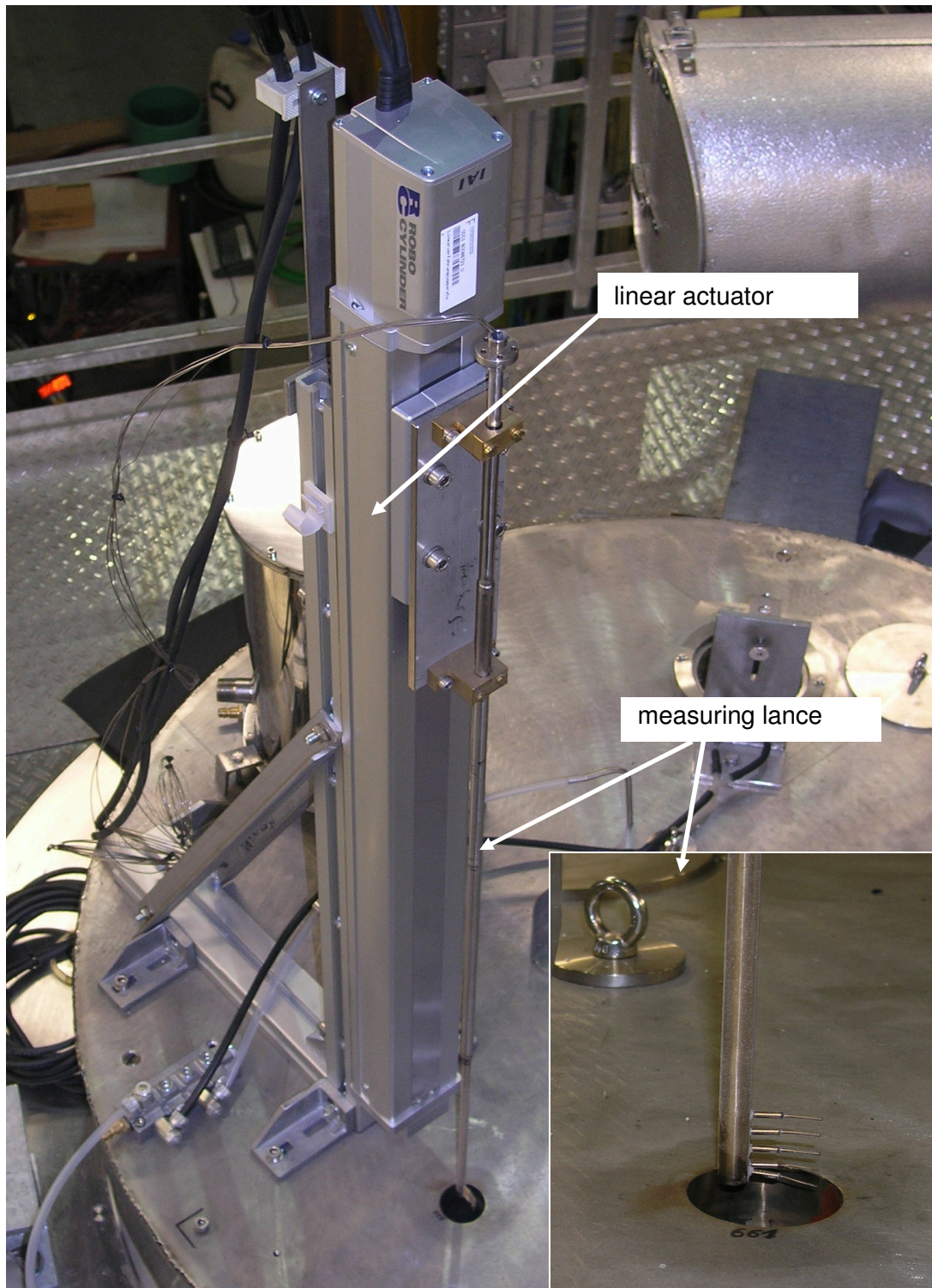
Figure 9: Crust detection system mounted on the lid of the test vessel.

3 Preparation and performance of the LIVE-L3A test

The experiment LIVE-L3A was successfully conducted on April 23-25, 2008. It was prepared and performed nearly identically in comparison with the experiment LIVE-L3 [5]. The simulated core melt was generated in the heating furnace as described in the section 2.2.2. The experiment started with the melt pour from the heating furnace into the test vessel. In Table 4 the planned main test parameters and the test phases of the experiment are summarised. The melt was discharged in one single lateral pour and the planned initial temperature of the melt was 350 °C. The pouring mass was 224.4 kg (corresponds to 120 l volume). The only difference between the LIVE-L3A and LIVE-L3 experiments was the outside cooling conditions. In LIVE-L3 the water cooling of the outside of the test vessel was started about 7200 s after the melt pouring. Therefore in this experiment the initially formed crust layer was partially re-molten in the first phase of the test due to insufficient cooling by air and the increase of the melt temperature. In the second phase of the test after the water cooling initiation the new crust formed at the vessel wall and grew symmetrically. In contrast with LIVE-L3, the test vessel in the LIVE-L3A was cooled by water already 2 minutes before the melt pouring with ~47 g/s water flow rate. These conditions allow fast crust formation also influenced by the lateral melt pouring position, which can lead to asymmetry in the heat flux distribution and crust thickness.

Table 4: Designed test parameter and test phases of the experiment LIVE-L3A.

Melt characteristics and preparation		
Type	NaNO$_3$	KNO$_3$
Mole %	20 %	80 %
Mass %	17.37 %	82.63 %
Mass	68 kg	324 kg
Total mass	392 kg	
Loading of the furnace	~455 l powder (for T=20 °C) ~210 l melt (for T=350 °C)	
Pouring mass	120 l or 224.4 kg (corresponds to ~31 cm melt height)	
Initial melt temperature	350 °C	
Flow rate of nitrogen flushing	2 l/min	
Melt pour		
Position	lateral	
Number of pours	1	
Furnace tilting velocity	0.5°/s	
Furnace target angle	76°	

Pouring rate	6 kg/s
Pouring spout temperature	360 ℃
Phase 1: Homogeneous heat generation with continuous outer vessel wall cooling	
Start time	145 s
Boundary conditions	water, continuous cooling
Cooling water flow rate	~0.047 kg/s
Heating planes	all
Heating power	10 kW
Heat generation	homogeneous
Initial melt temperature	350 ℃
Phase 2: Reduction of heat generation	
Test conditions	reaching of steady-state conditions in phase 1
Start time	90237 s
Boundary conditions	water, continuous cooling
Cooling water flow rate	~0.047 kg/s
Heating planes	all
Heating power	7 kW
Heat generation	homogeneous
Phase 3: Test termination and melt extraction	
End time	181400 s
Test conditions	reaching of steady-state conditions in phase 2
Heating power	switched off

The measured flow rate of the cooling water after the melt pouring is shown in the Figure 10. The planned flow rate of ~47 g/s was kept very well throughout the whole test.
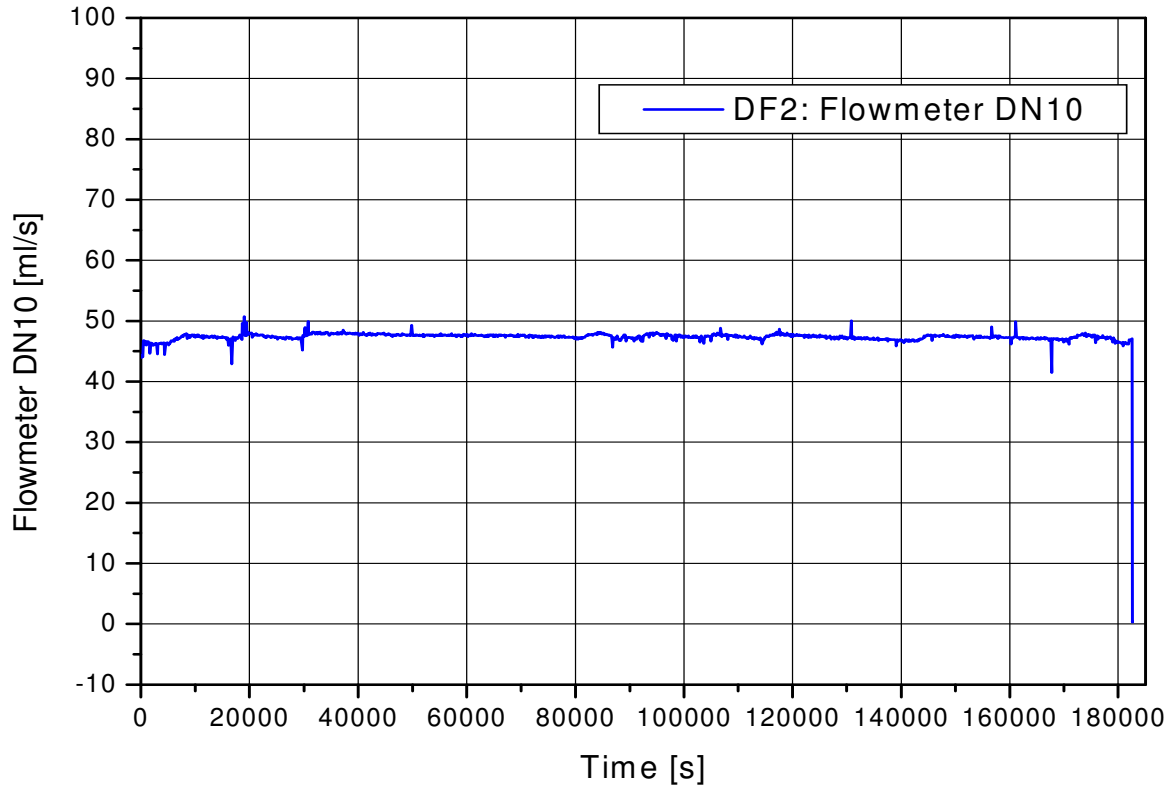
Figure 10: Cooling water flow rate in the LIVE-L3A experiment.

After the completion of the pouring process, the first test phase with a homogeneous heat generation in the melt started. A heating power of approximately 10 kW was applied by switching all six heating planes simultaneously. This volumetric homogeneous heating of the melt was continued for about 25 hours to reach the steady-state conditions in the melt pool.

After about 90237 s the test phase 2 was started, in which the heating power was reduced to 7 kW to observe the influence of the power reduction on the crust growth and heat flux distribution. This power level was kept for another 25.5 hours. In the last test phase the heating power was switched off and the extraction of the residual melt from the test vessel back into the heating furnace was initiated. The duration of melt extraction was 55 seconds.

The course of the test LIVE-L3A test in chronological order is described in the Table 5.

Table 5: Sequence of events of the LIVE-L3A experiment.

Time of day	Event
23.04.2008	
8:06	Melt temperature in the heating furnace 349.5 °C and 342 °C
8:30	Start of the PC data acquisition system
8:55	Weight of test vessel: 2017 kg (incl. pouring spout)
8:56	Start of the external vessel cooling, cooling water flow rate ~0.047 kg/s
8:58	Start of the video recording of the pouring process
8:58:30	Start of the video recording of the melt surface (top and side view)
8:59	Start of the IR camera recording
9:00:03	Start of the pouring program of heating furnace
9:03:44	End of the pouring process, furnace returned to the original position
9:04	Weight of test vessel 2241 kg (incl. pouring spout)
9:04:10	Start of the heating system, 10 kW, homogeneous heat generation
9:08:20	Heating furnace power switched off
9:10:30	Pouring spout removed, weight of the test vessel: 2242 kg
10:00	Condenser – cooling water on
24.04.2008	
9:08	Start of the crust thickness measurement with measuring rod
10:01	End of the crust thickness measurement with measuring rod
10:05	First melt sample extraction through central pouring opening in the lid
10:06	Reduction of heating power to 7 kW, homogeneous heat generation
25.04.2008	
9:10	Start of the crust thickness measurement with measuring rod
10:33	End of the crust thickness measurement with measuring rod
10:38	Second melt sample extraction through central pouring opening in the lid
11:09	Weight of test vessel: 2249 kg (incl. extraction funnel)
11:19:30	Start of the video recording of the test vessel
11:24	Weight of test vessel: 2250 kg (incl. extraction tube)
11:24	Heating power switched off, start of extraction of the residual melt
11:25:30	End of the extraction
11:28	Weight of test vessel: 2071 kg (without extraction tube)
11:44	Cooling water flow switched off
11:45:18	PC data acquisition switched off

4   LIVE-L3A test results

4.1   Mass and initial temperature of the melt

The experiment LIVE-L3A started with the pouring of the simulated corium melt from the heating furnace into the LIVE test vessel near to the vessel wall via the preheated pouring spout. The experimental time t = 0 s is determined by the first response of the thermocouple located in the pouring spout (ST1).
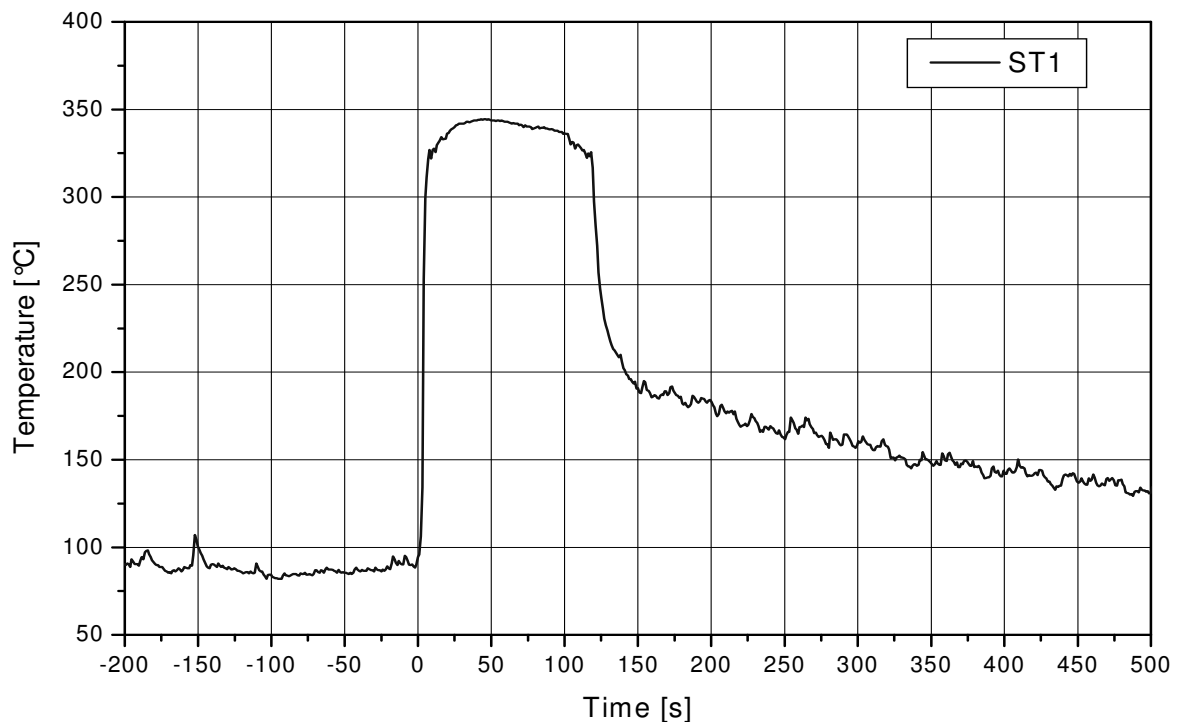
Figure 11: Initial melt temperature measured in the pouring spout in LIVE-L3A.

The temperature measurement of the thermocouple ST1 is shown in Figure 11. The initial temperature of the $NaNO_3$-KNO_3 melt in the pouring spout was about 344 °C, which is in good agreement with the planned 350 °C.

The mass of the test vessel during the pouring of the melt increased from about 2017 kg to 2241 kg (Figure 12). Therefore about 224 kg of nitrate melt has been poured into the test vessel. With a density of about 1870 kg/m^3 for the 20/80 mole% $NaNO_3$-KNO_3 melt with a temperature of 344 °C, determined in [11], a volume of ~119.7 l was released into the test vessel which is very close to the planned volume of 120 l.
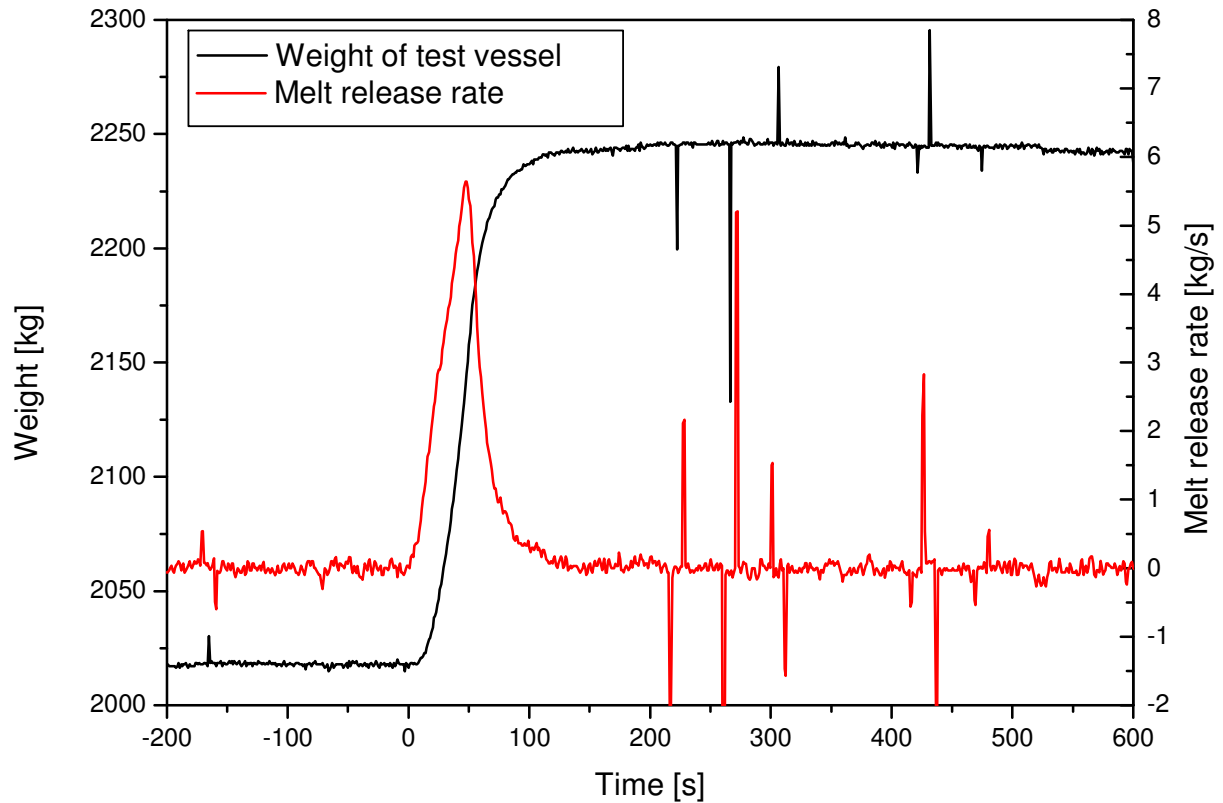
Figure 12: Weight of the test vessel and melt release rate in LIVE-L3A.

The vessel weight and the melt release rate are shown in Figure 12. The maximum pouring rate derived from the analysis of the weight of the test vessel was ~6 kg/s.

4.2 Decay heat simulation in LIVE-L3A

In order to compare the LIVE-L3A and LIVE-L3 test results the same power generation history was applied. The heating power generated by each of the six heating planes is shown in Figure 13.

About 145 s after pouring initiation the upper heating plane was covered with melt and a heating power of approximately 10 kW was applied to heat the melt homogeneously by switching all six heating planes simultaneously. The measured total heating power of two-minute average was 10025 W at 50000 s. The volumetric homogeneous heating of the melt was continued for about 25 hours.

After 90237 s the second phase of the test was started and the heating power was reduced to 7 kW. This power level was kept for another 25.5 hours. The measured total heating power was exactly 7000 W in two minute average at 150000 s. At 181395 s of the experiment time the heating power was switched off and the residual melt was extracted from the test vessel back into the heating furnace.

22
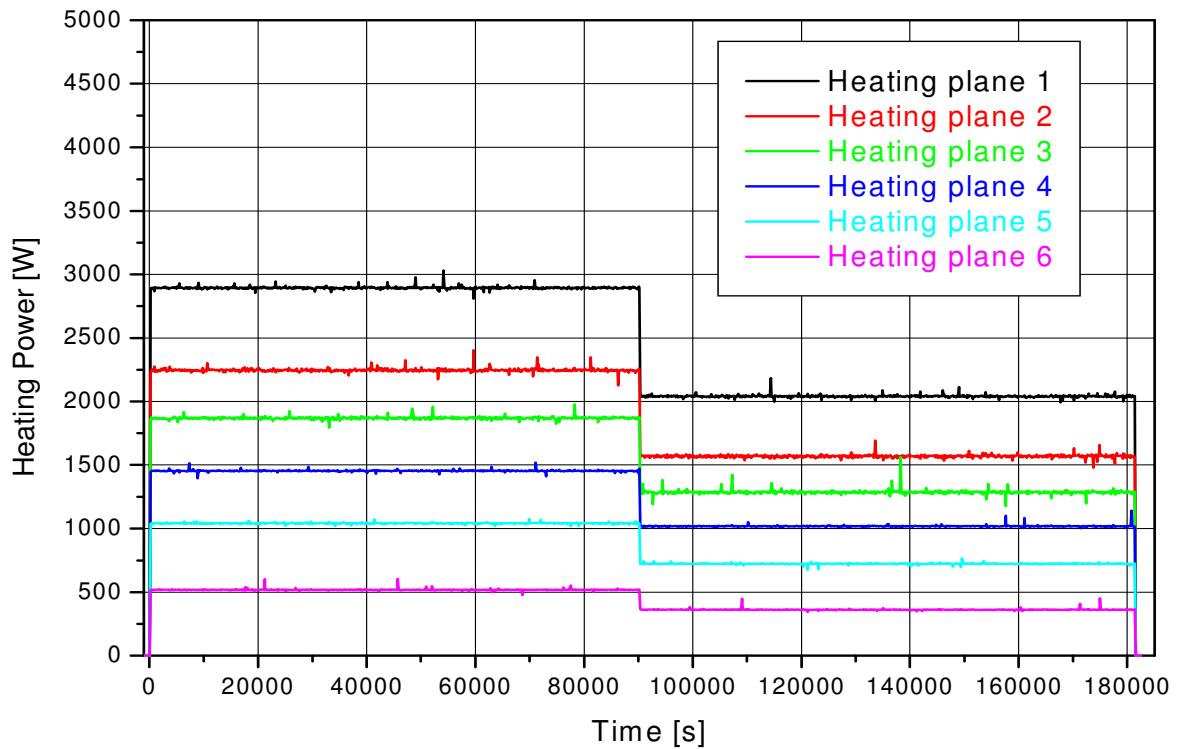
Figure 13: Heating power generated by each of the six heating planes in LIVE-L3A.

4.3 Melt behaviour in LIVE-L3A

The development of the melt temperature during the initial test period is shown in Figure 14. After the melt pouring the melt temperature in the middle and the lower part of the vessel decreased immediately, whereas the melt temperature in the upper part of the melt pool increased slightly and then decreased to a constant value. The melt temperature in the lower part of the vessel decreased faster and it took shorter time to reach a constant value compared to the melt temperatures in the middle and upper regions in the vessel. The time periods of the melt temperature at vessel height 70 mm, 170 mm and 270 mm to reach the quasi steady value were 800 s, 1500 s and 2000 s respectively. The melt pool temperatures at different elevations at the azimuth angle 0° during the whole test period are shown in Figure 15. The steady-state melt temperatures ranged from 290 °C in the vessel bottom area to 321 °C near the melt surface. Only at the position of the MT5 thermocouple, which is located close to the vessel bottom and near to the vessel wall, the temperature decreased below the liquidus temperature of the melt. This indicates the crust formation at this position. The temperature measurements along the azimuth at 90°, 180° and 270° are similar to the temperature measurements along the azimuth at 0° and the diagrams are shown in Figure C-1 to Figure C-3 in the Annex C. After 90237 s the heating power was reduced to 7 kW. The melt pool temperatures decreased to constant values between 285 °C and 310 °C.
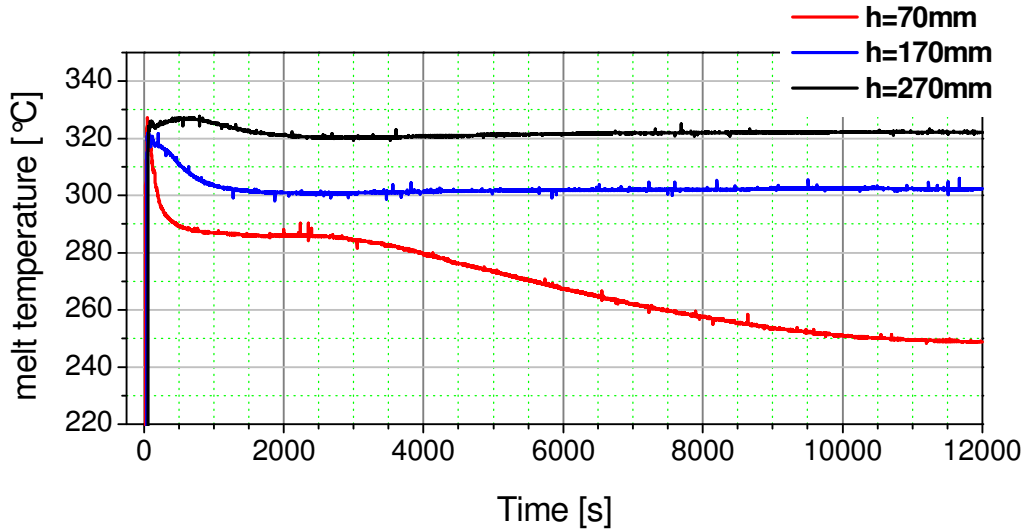
Figure 14: Initial melt temperature during LIVE-L3A.
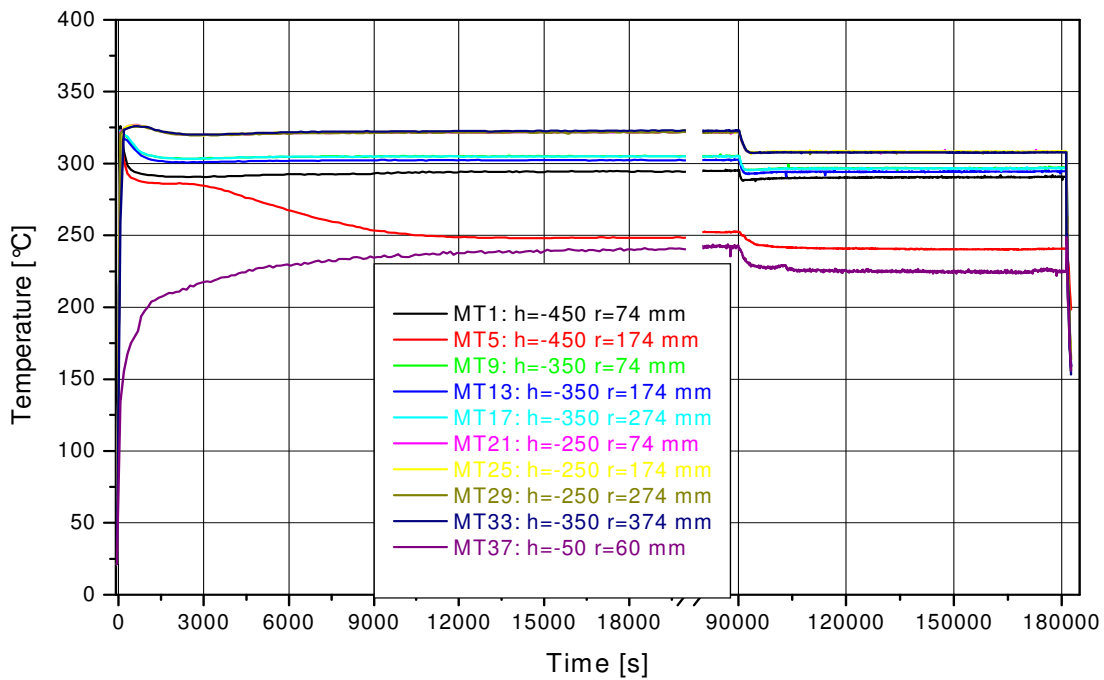
Figure 15: Melt pool temperatures at different elevations along
the azimuth anlge 0° in LIVE-L3A.

Table 6 presents the melt temperatures at different locations during 10 kW and 7 kW heating periods. The given values are averages over 2 minutes, i.e. the average of all values 60 s before and 60 s after the given time. No significant differences in the horizontal distribution of the melt temperature could be observed in spite of asymmetric melt relocation at the beginning of the test. The temperatures at the same radius and the same depth but different angles are always very similar.

Table 6: Temperatures measured in the melt pool during 10 kW and 7 kW test phases (values are averages over 2 minutes).

Thermocouple number	Position			Temperature during 10 kW [°C] 50000s	Temperature during 7 kW [°C] 150000s
	Azimuth angle φ	Radius [mm]	Depth from flange upper range / Vessel height [mm]		
MT1	0	74	450/70	**295**	**290**
MT2	90	74	450/70	**291**	**287**
MT3	180	74	450/70	**296**	**292**
MT4	270	74	450/70	**293**	**288**
MT5	0	174	450/70	**252**	**240**
MT6	90	174	450/70	**263**	**239**
MT7	180	174	450/70	**293**	**286**
MT8	270	174	450/70	**250**	**245**
MT9	0	74	350/170	**305**	**297**
MT10	90	74	350/170	**306**	**298**
MT11	180	74	350/170	**303**	**295**
MT12	270	74	350/170	**308**	**299**
MT13	0	174	350/170	**302**	**294**
MT14	90	174	350/170	**304**	**296**
MT15	180	174	350/170	**305**	**297**
MT16	270	174	350/170	**303**	**295**
MT17	0	274	350/170	**305**	**297**
MT18	90	274	350/170	**305**	**297**
MT19	180	274	350/170	**304**	**296**
MT20	270	274	350/170	**305**	**297**
MT21	0	74	250/270	**322**	**308**
MT22	90	74	250/270	**324**	**310**
MT23	180	74	250/270	**323**	**309**
MT24	270	74	250/270	**321**	**308**
MT25	0	174	250/270	**322**	**308**
MT26	90	174	250/270	**323**	**309**
MT27	180	174	250/270	**322**	**308**
MT28	270	174	250/270	**322**	**309**
MT29	0	274	250/270	**322**	**308**
MT30	90	274	250/270	**322**	**308**
MT31	180	274	250/270	**322**	**308**
MT32	270	274	250/270	**322**	**308**
MT33	0	374	250/270	**323**	**308**
MT34	90	374	250/270	**323**	**308**
MT35	180	374	250/270	**323**	**309**
MT36	270	374	250/270	**321**	**307**

The development of the melt temperature vertical profile is shown at radial location 174 mm in Figure 16. The temperature of the melt at the bottom of the test vessel was always lower than the temperature of the melt at the upper part of the test vessel. The melt temperatures in the upper part of the melt pool were very similar during the whole test duration. The melt temperature in the lower part differed after ~5000 s. Except at the azimuth angle 180°, in other positions in the lower part of the pool the melt temperatures were below the melt liquidus temperature.
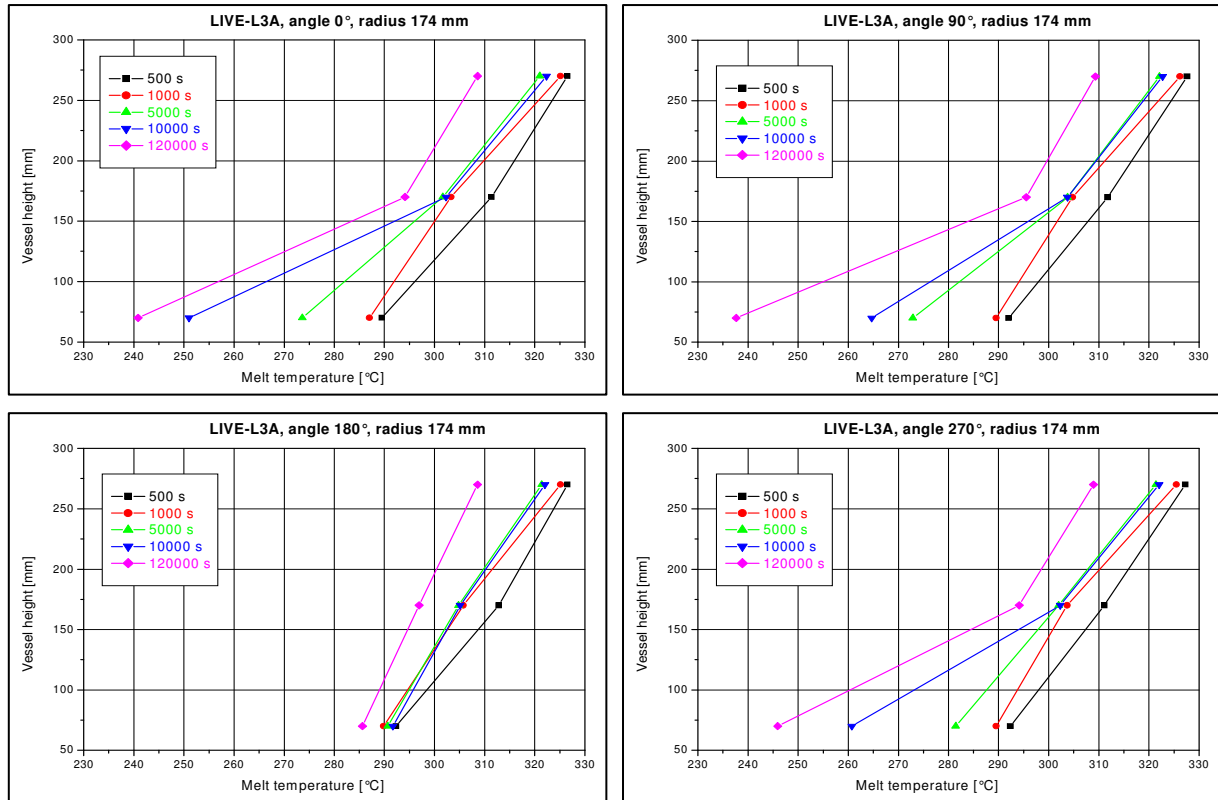
Figure 16: Melt pool temperatures at different positions at the radius 174 mm at different times in LIVE-L3A.

4.4 Heat flux and heat balance in LIVE-L3A

4.4.1 Calculated heat fluxes in LIVE-L3A

The heat flux through the vessel wall can be calculated based on the temperature difference between the inner and outer surface of the test vessel wall. The heat flux q through a plane wall is given by:

$$q_{pla} = -k \cdot (T_o - T_i)/L \tag{1}$$

where

q_{pla}: heat flux, W/m^2,

k: thermal conductivity of the wall, W/mK,

T_o: outer wall temperature (measured by OT thermocouples), K,

T_i: inner wall temperature (measured by IT thermocouples), K,

L: wall thickness, m.

To calculate the heat flux through a spherical wall, q_{sph}, as in the case of the LIVE test vessel, the heat flux expressed in the Eq. (1) should be corrected accordingly. Assuming the inside area of a spherical wall is the same as that of a plane wall, and the spherical wall also has the same thickness as the plane wall one can obtain:

$$q_{sph} = q_{pla} \cdot (R_i / R_o) \qquad\qquad (2)$$

where

R_i: inner spherical wall radius, m,

R_o: outer spherical wall radius, m.
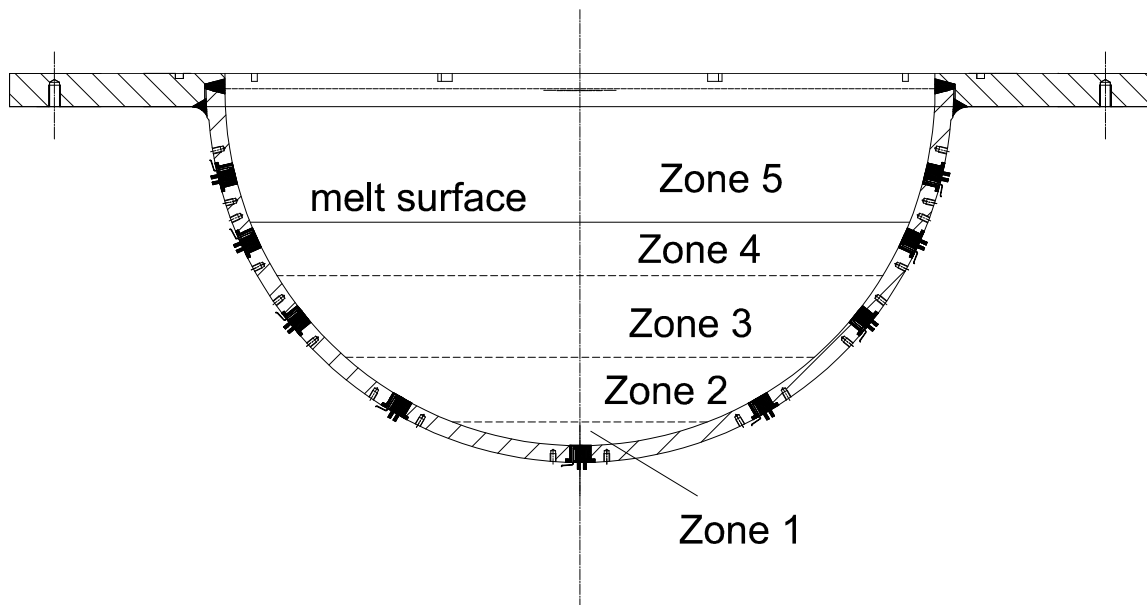
Figure 17: Definition of heat flux zones on the test vessel wall surface.

Wall inner (IT thermocouples) and outer (OT thermocouples) temperatures at 17 positions were measured during the test at five levels. For the calculation of the heat fluxes through the vessel wall, five horizontal heat flux zones are defined on the test vessel wall surface, as shown in Figure 17. Each zone has its own local heat flux and surface area. The boundary between each zone under the melt surface is at the middle of the height between two levels of IT and OT thermocouples. The two upper zones are divided by the melt surface. The geometric data of the zones are given in Table 7.

Table 7: Geometries of the heat flux zones.

	Thermocouples	Position to flange upper edge [mm]	Height of zone [mm]	Zone inner area A_i [m²]
Zone 1	IT/OT 1	-520	32.5	0.1014
Zone 2	IT/OT 2-5	-455	91.5	0.2855
Zone 3	IT/OT 6-9	-337	112.5	0.3510
Zone 4	IT/OT 10-13	-230	83.2	0.2387
Zone 5	IT/OT 14-17	-140	176.9	0.5729

Table 8: Correction factor for spherical form and wall thickness.

	Zone 1	Zone 2	Zone 3	Zone 4	Zone 5
thermocouples	IT/OT 1	IT/OT 2-5	IT/OT 6-9	IT/OT 10-13	IT/OT 14-17
polar angle, °	0	30	51	65.5	76.5
Ri/Ro	0.957	0.956	0.956	0.956	0.955
wall thickness, mm	23.3	23.5	23.63	23.76	23.9

The temperature measured by the IT and OT thermocouples are shown from Figure C-4 to Figure C-11 in Annex C. In Table 8, the local wall thickness and correction factor "*Ri/Ro*" for the five horizontal heat flux zones are given. The wall thickness is measured at the local positions of IT/OT thermocouples. The IT and OT thermocouples are mounted in grooves in the vessel wall. The height and diameter of the groves are equal to the diameter of the thermocouples. The groove depth for the IT thermocouples is 0.5 mm, and that for the OT thermocouples is 1 mm. Therefore the half of the total groove depth is deducted from the wall thickness for the heat flux calculation.

The wall of the test vessel is made of stainless steel AISI316Ti, the material number is X6CrNiMoTi17-12-2. The thermal conductivity of this material is taken from [12] and is presented in Table 9.

Table 9: Heat conductivity of the AISI316Ti steel.

Temperature, K	300	400	600
Heat conductivity, W/(mK)	13.4	15.2	18.3

Since the working temperature of the test vessel for the LIVE-L3A test was between 300 K and 400 K, the following equation can be obtained from the data given in the Table 9. The temperature is given in K.

$$k(T) = 13.4 + 0.018 \cdot (T - 300) \tag{3}$$

In the following, the results of the calculation of the heat fluxes based on the measurement of the inner and outer wall temperature are described in more detail. The thermocouple IT1 was destroyed during the test, therefore the thermocouple PT11 was used for the calculation of the heat flux for the heat flux zone 1. The value of PT11 is given in Figure C-12. The calculated heat fluxes during the whole test LIVE-L3A are also shown in Annex C from Figure C-13 to Figure C-16. The average heat flux in each heat flux zone is shown in Figure 18.
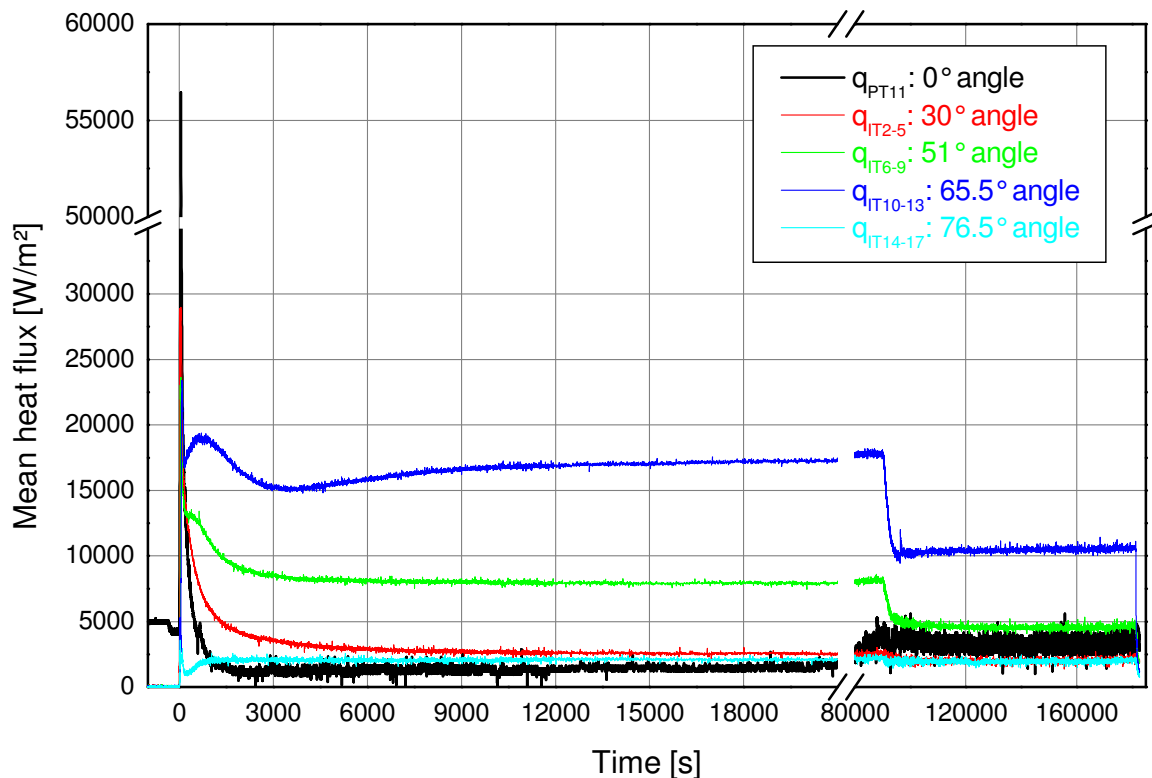
Figure 18: Average heat flux values for the five heat flux zones in LIVE-L3A.

The results show that the highest heat flux during the thermal hydraulic steady-state was in the zone 4 (heat flux $q_{IT10-13}$), which is just below the melt surface (the melt surface was located at the vertical angle of ~69°). The second highest heat flux zone was in the zone 3 (q_{IT6-9}), the level below the zone 4, followed by the zone 2 (q_{IT2-5}). The lowest heat fluxes were calculated for the heat flux zones 1 (q_{IT1}) and 5 ($q_{IT14-17}$).

In Table 10, the heat fluxes calculated with IT/OT measurements as 2 minutes average values at the steady-state during the 10 kW (time 50000 s) and 7 kW (time 150000 s) heating periods are listed.

Table 10: Calculated heat fluxes (W/m^2) during pouring and during steady-state of 10 kW and 7 kW heating power in LIVE-L3A.

Plug Nr.	Area zone	Heat flux position q_{IT}	q at 10 kW steady-state 50000 s	q at 7 kW steady-state 150000s	Max. transient q at pouring
1	1	q_{PT11}	1983	2873	56461
2-5	2	q_{IT2} (22.5°)	2432	1911	24351
		q_{IT3} (112.5°)	2425	1905	44432
		q_{IT4} (202.5°)	2529	2128	58690
		q_{IT5} (292.5°)	2131	1616	18303
6-9	3	q_{IT6} (22.5°)	6884	4068	25178
		q_{IT7} (112.5°)	6664	3615	20770
		q_{IT8} (202.5°)	9897	4988	29325
		q_{IT9} (292.5°)	8555	5311	38009
10-13	4	q_{IT10} (22.5°)	14205	9138	14672
		q_{IT11} (112.5°)	19002	11669	29914
		q_{IT12} (202.5°)	19825	11348	28261
		q_{IT13} (292.5°)	17564	9707	28664
14-17	5	q_{IT14} (22.5°)	1879	1769	4989
		q_{IT15} (112.5°)	2906	2693	12098
		q_{IT16} (202.5°)	2112	1929	3511
		q_{IT17} (292.5°)	1650	1769	1632

The mean value of the heat flux for each zone is shown in Figure 19. The results indicate that by increasing the heat generation in the melt pool the corresponding heat flux increases mainly in the upper part of the melt, whereas the heat flux in the lower part of the melt remains almost constant.

The horizontal heat flux distribution during the 10 kW heating period is shown in Figure 20. Considerable asymmetry in horizontal heat flux distribution is observed in the upper part of the vessel, where the contact area of the melt jet with the vessel wall was located. The opening for the melt pouring in the upper lid is 80 mm in diameter. The contact area of the wall with melt is positioned at polar angle between 52°-72° and at azimuth angle between 112.5°-202.5°. Figure 20 shows that the heat flux through the melt pouring area during the steady-state was about 1.4 times higher than the one at the opposite side. The asymmetric horizontal heat flux distribution could result from the asymmetric melt relocation position. Probably the crust at the melt pouring area solidified in different cooling condition during the melt pour-

ing period, which led to different crust properties such as crust thickness and crust thermal conductivity.
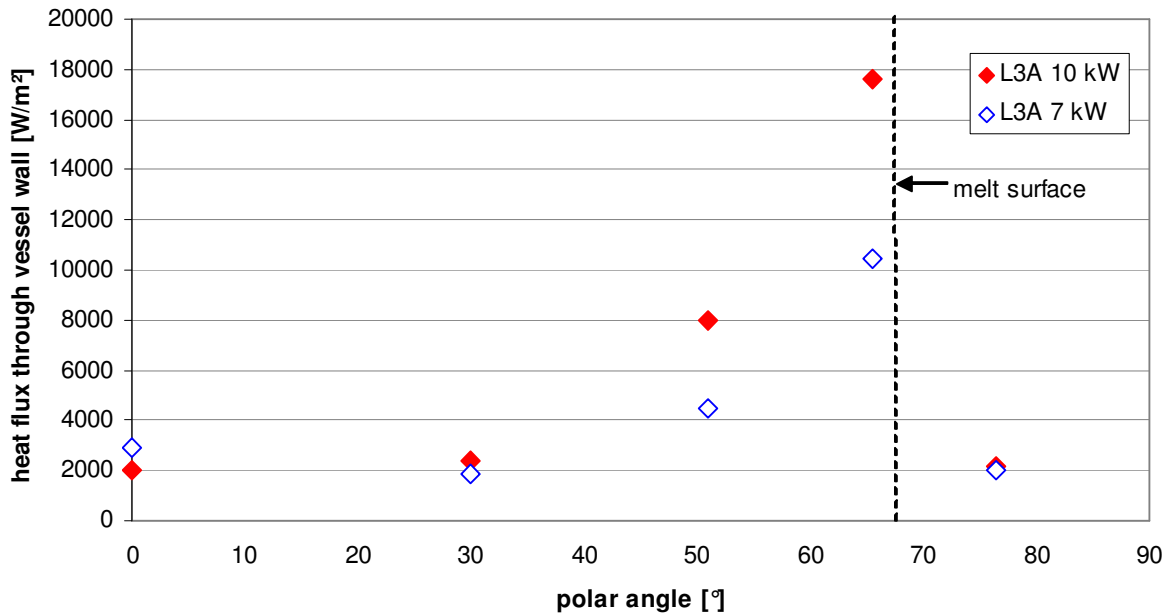
Figure 19: Calculated heat flux distribution along the vessel wall in LIVE-L3A.
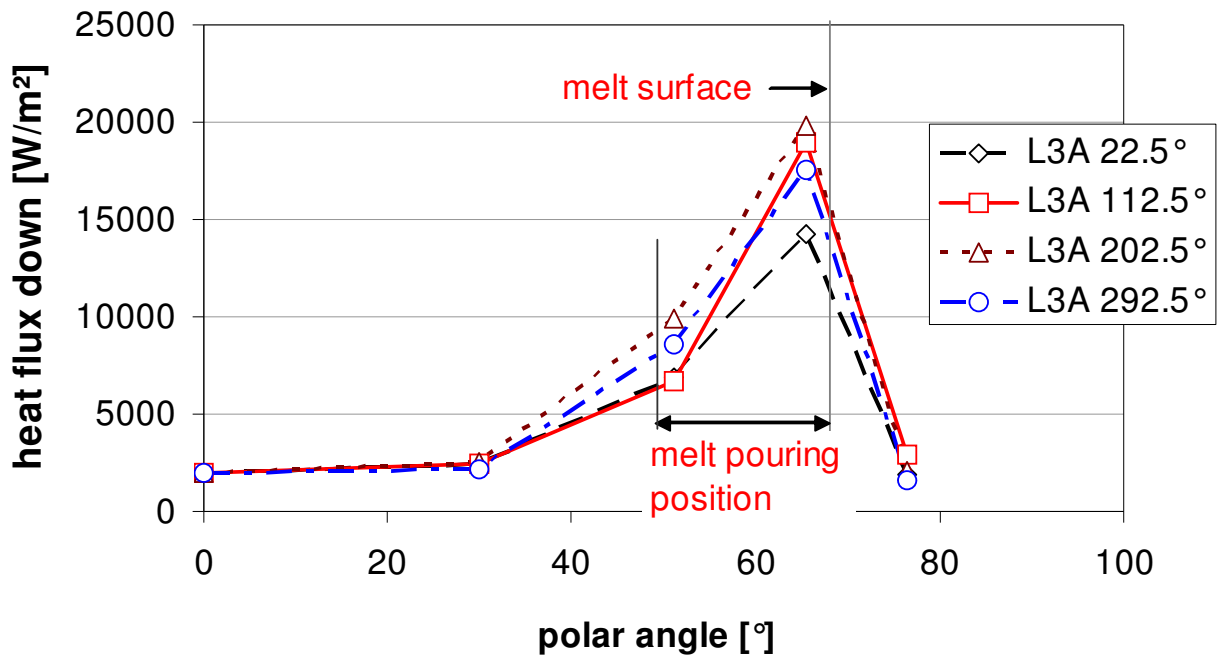
Figure 20: Heat flux distribution at four azimuth angles during 10 kW steady-state in LIVE-L3A.

The maximum transient heat fluxes during pouring are also shown in Table 10. The transient heat fluxes during pouring were significantly higher than the heat fluxes during steady-state. All heat flux values during melt pouring are illustrated in Figure 21. The maximum heat flux values were in the zone 2 and zone 1 with ~59 kW/m^2 and 57 kW/m^2 respectively. After the melt pouring, the heat flux decreased rapidly in about 3 minutes, and then further decreased slowly to constant values.
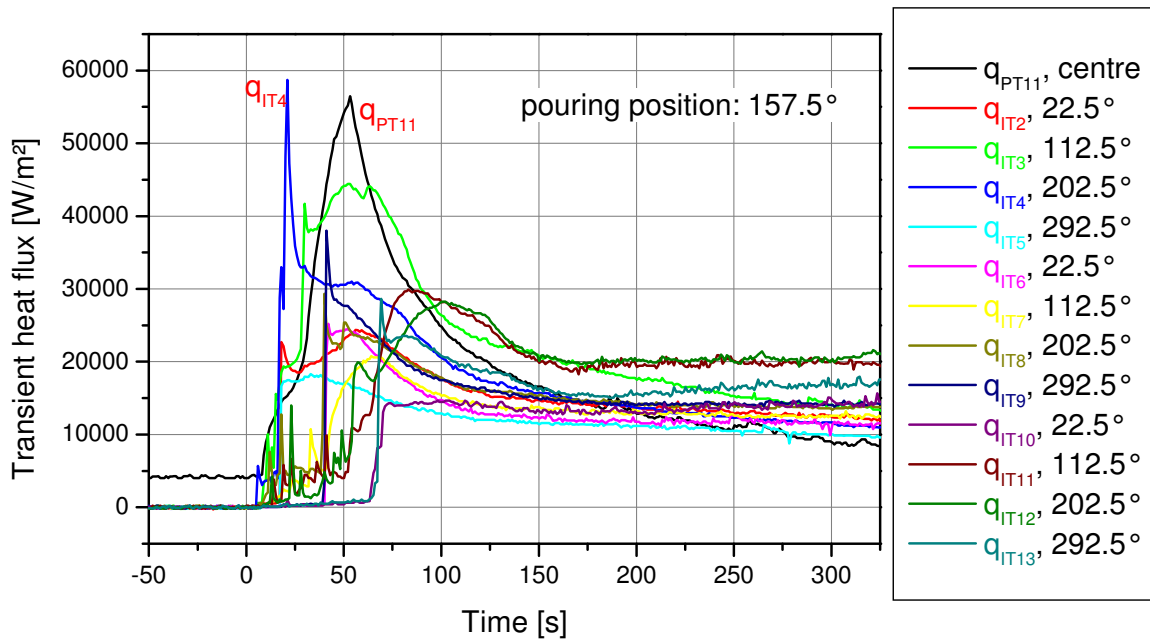
Figure 21: Calculated transient heat fluxes during the initial period of 10 kW in LIVE-L3A.

4.4.2 Heat balance during the steady-state in LIVE-L3A

During the thermal hydraulic steady-state of a severe accident in the lower head of the RPV a part of the decay heat generated in the melt pool is removed through the bottom hemispheric vessel wall and the rest of the decay heat is released from the melt pool upper surface. The fraction of the heat transferred through the vessel wall is extremely important to determine the cooling effectiveness by external flooding for different heat generation and cooling rates.

In the LIVE test facility the heat through the vessel wall (Q_{wall}) is removed by water which flows from the bottom to the top opening of the cooling vessel. The heat through the test vessel wall can be calculated from the heat flux estimation, and the heat removed by water (Q_{water}) can be calculated based on the water inlet and outlet temperature and the water flow rate. The aim of the heat balance calculation in the test LIVE-L3A is a) to determine the Q_{wall} for different heat generation levels and b) to check the reliability of the measurements in the LIVE facility by comparing Q_{wall} with Q_{water}.

The total heat transfer through the vessel wall Q_{wall} is the sum of the local heat flux multiplied by the corresponding surface area of the vessel wall:

$$Q_{wall} = \sum q_i \cdot A_i \tag{4}$$

where

q_i: local heat flux, W/m^2,

A_i: surface area of the of the corresponding local heat flux zone, m^2.

The heat flux of each zone was calculated in section 4.4.1 and the corresponding surface areas are shown in Table 7.

The heat removed by cooling water (Q_{water}) is calculated according to equation (5):

$$Q_{water} = c_p \cdot f_w \cdot (T_{out} - T_{in}) \tag{5}$$

where

c_p: specific heat capacity of water, 4.193 J/gK at 10 °C,

f_w: water mass flow rate, g/s,

T_{out}: outlet temperature of the cooling water, K

T_{in}: inlet temperature of the cooling water, K

In order to calculate the fraction of the heat transferred through the vessel wall at steady-state conditions, two times are selected: 50000 s (10 kW period) and 150000 s (7 kW period). The 2 minute average value of the heat transferred through the vessel wall (Q_{wall}) and the heating power ($Q_{heating}$) at these times are listed in Table 11.

The results in the Table 11 show that more than 80 % of the total heat was removed through the vessel wall to the cooling water. This high value of Q_{wall} resulted from the good insulation of the vessel upper lid. Furthermore, heat generation leads to a higher fraction of Q_{wall}. About 91 % of the heat was released through the vessel wall to the cooling water during the steady-state phase with 10 kW heating power compared to about 86 % during the steady-state phase of 7 kW heating power. Most of the rest heat was removed through the shortcuts in the vessel flange and openings in the upper lid.

Table 11: Heat balance between the heat transfer through the vessel wall and heating power

Heating period	Time	Q_{wall}	$Q_{heating}$	$Q_{wall}/Q_{heating}$
10 kW	50000 s	9125 W	10025 W	91 %
7 kW	150000 s	6053 W	7000 W	86 %

To calculate the Q_{water}, the water inlet T_{in} and outlet T_{out} temperatures were measured during the test. It was found out after the test that the thermocouples used to measure these temperatures (designated as ZT and AT) slightly deviated from the real values in the working temperature range. After the post-test calibration of these two thermocouples, following equations are obtained to correct the measured values of the water inlet and outlet temperatures.

$$T_{in}^{real} = -0.3389 + 1.0089 \cdot T_{in}^{measured} \tag{6}$$

$$T_{out}^{real} = 0.1419 + 0.9518 \cdot T_{out}^{measured} \tag{7}$$

The temperature of the cooling water at the inlet was about 11 °C, the temperature of the cooling water outflow during the 10 kW steady-state was ~51 °C and during the 7 kW steady-state it was reduced to ~37 °C. The corresponding temperature plot is given in Figure C-20. The heat balance between the heating power, Q_{wall} and Q_{water} for the whole test duration is shown in Figure 22.
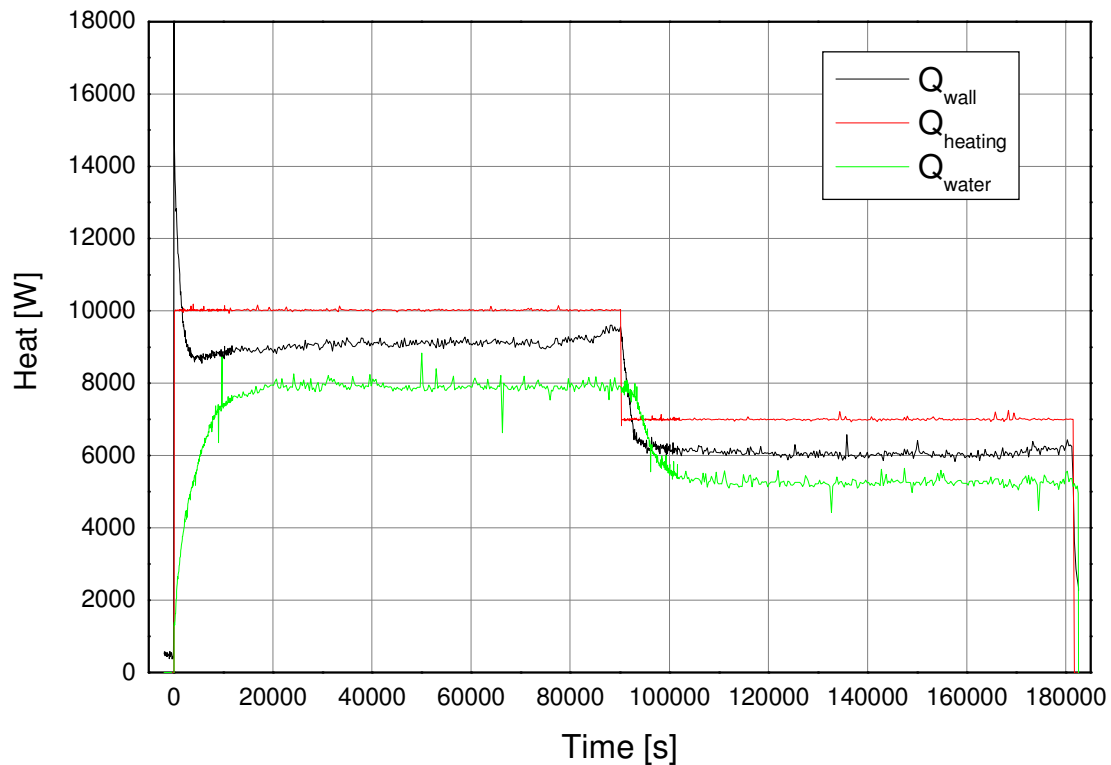
Figure 22: Heat balance between heating power, heat transfer through the vessel wall and heat removed by the cooling water in LIVE-L3A.

The heat removed by cooling water (Q_{water}) was ~7% lower than the total heat transferred through the vessel wall (Q_{wall}). No noticable measurement errors can be detected for the water flow meter and water temperatures, as well as for the wall inner (IT) and outer temperatures (OT) for the Q_{wall} determination. Therefore realistic value of the Q_{wall} should be in the range between 0 % and 7 % of the measured Q_{wall}.

4.4.3 Behaviour of the melt surface

As it is described in the section 2.4, an infrared camera is installed at the lid of the facility to observe the melt surface behaviour near to the vessel wall. The recorded thermograms are used to measure the temperature distribution on the surface of the molten pool and to identify the convection patterns in the fluid during different stages of experiments (Figure 23).
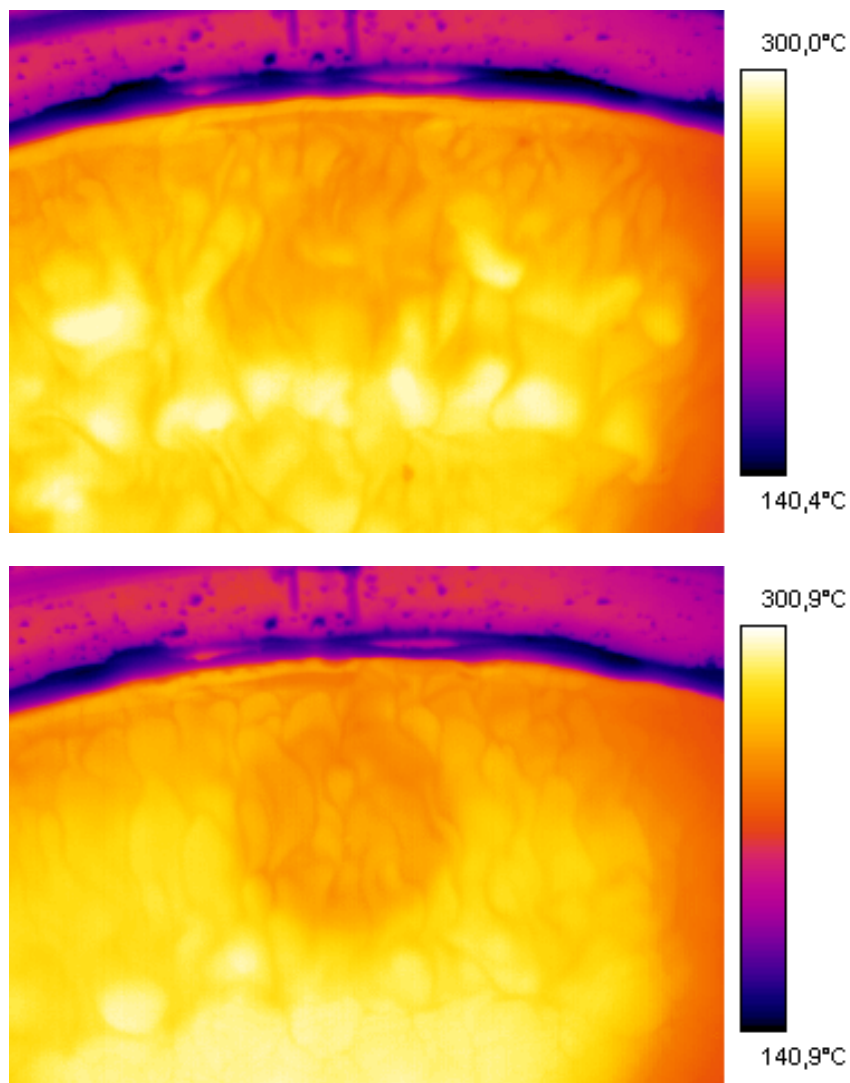
Figure 23: IR images on the melt surface:
top: 3 min after the melt pouring; bottom: steady-state during 10 kW.

The analysis of the recordings shows a complex picture of the fluid motion at the upper surface. The general trend is that the fluid is transported from the center of the pool to the vessel outer wall. To quantify the flow velocity, the IR pictures were analysed similarly to particle image velocimetry (PIV). Instead of seeds used in PIV, moving areas of the melt surface with distinctive patterns were used, assuming that they follow the flow dynamics. The displacement of the patterns after 2 seconds was determined and the flow velocity was calculated. In the LIVE-L3A the flow velocity of the upper surface has been analysed during the transient phase and during the steady-state phase of 10 kW heat generation.

The results of the measurements are presented in Figure 24 and Figure 25. The X-axis is given in the dimensionless term R/R_{ves} where R is the starting radial position of the analysed point and R_{ves} is the vessel radius (50 cm). The complex motion pattern leads to a large scatter of the results, the calculated flow velocities during the transient phase of the test are within the range 0.3-0.4 cm/s. During the steady-state the flow velocity increases to the value of ~0.5 cm/s.
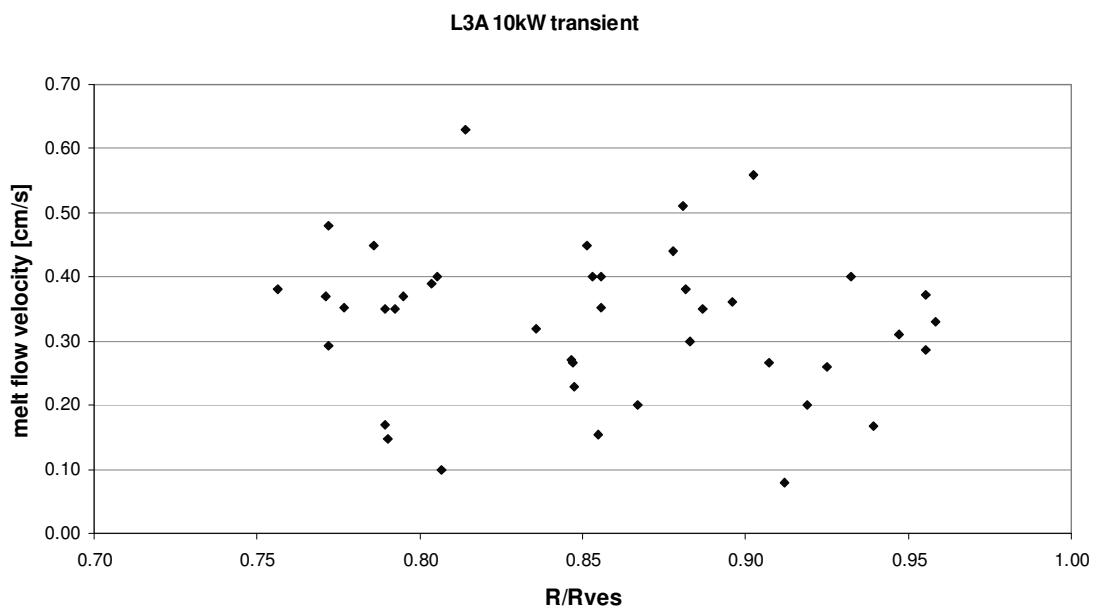
Figure 24: Flow velocity measured at the upper surface during the transient phase of the test.
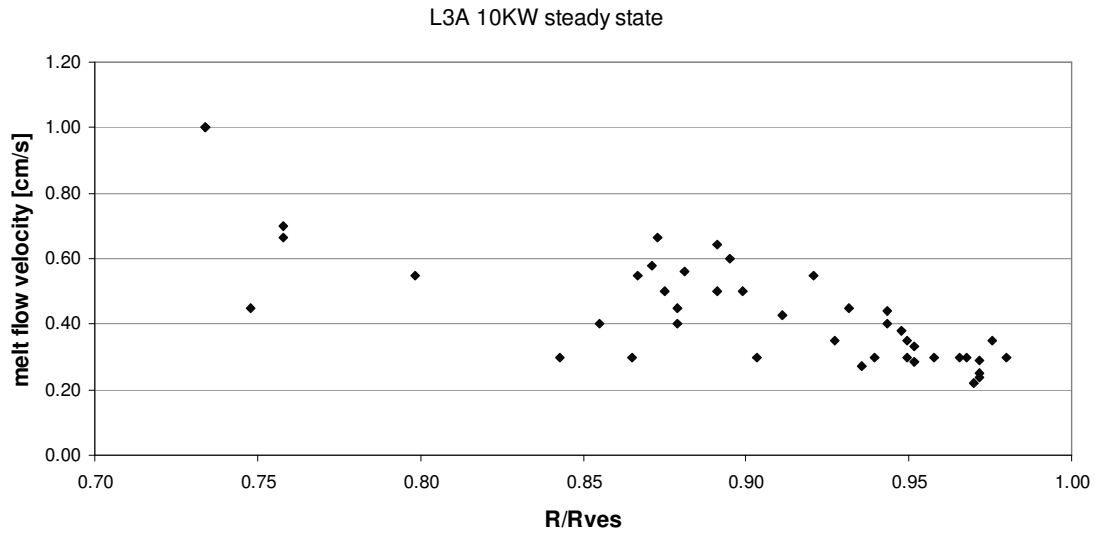
Figure 25: Flow velocity measured at the upper surface during the steady-state of 10 kW.

4.4.4 Melt pool temperature profile and boundary layer temperature

The vertical melt pool temperature profile, the crust thickness and the melt/crust boundary temperature can be measured with the crust detection system shown in Figure 9. Without crust layer at the wall, the lance can touch the vessel wall at polar angle 47°. In Figure 26 the position of the crust detection lance is illustrated.
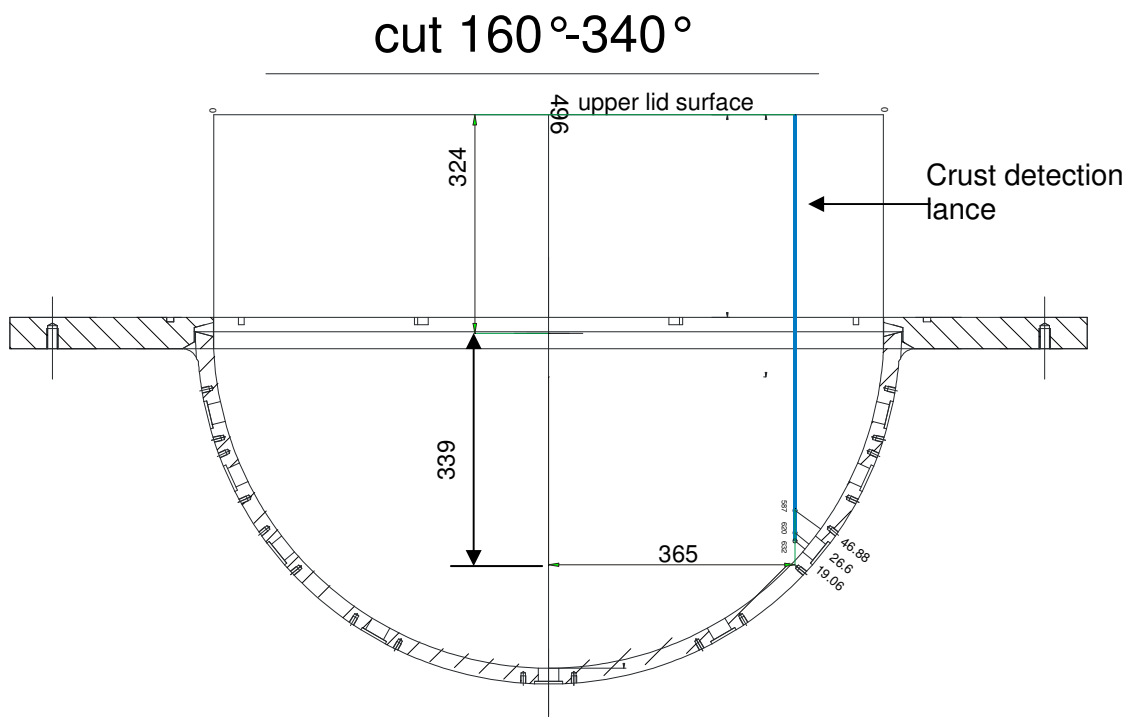
Figure 26. Position of the crust detection lance used for crust thickness and vertical temperature profile measurements.

The experimental data obtained from the crust detection lance provide important information for the understanding of solidification character and melt pool behaviour. The temperature gradient ahead of the crust front is an important parameter to evaluate the melt solidification process which is discussed in the section 4.5.2. A detailed melt temperature vertical profile gives information about the heat transfer and flow pattern in the melt.

The crust thickness detected with the lance at the polar angle 47° in the LIVE-L3A was 9.9 mm during the steady-state of 10 kW and 17.4 mm during the steady-state of 7 kW. The melt pool temperature profiles during 10 kW and 7 kW heating period are shown in Figure 27. The vertical temperature profiles measured at the position shown in Figure 26, have four characteristic temperature regions in the bulk of the melt pool: the first region was the temperature boundary layer, whose thickness was about 3 mm during the steady-state and the temperature gradient was ~9.5 K/mm; the second region was a down flow of the melt, the temperature in this area was very fluctuating; the third region was a stagnant zone with stratified temperature profile; the last region was a turbulent zone with almost homogenous melt temperature distribution. Reducing the heating power from 10 kW to 7 kW led to a decrease of melt temperature about 10 °C in the down flow zone and the centre zone.
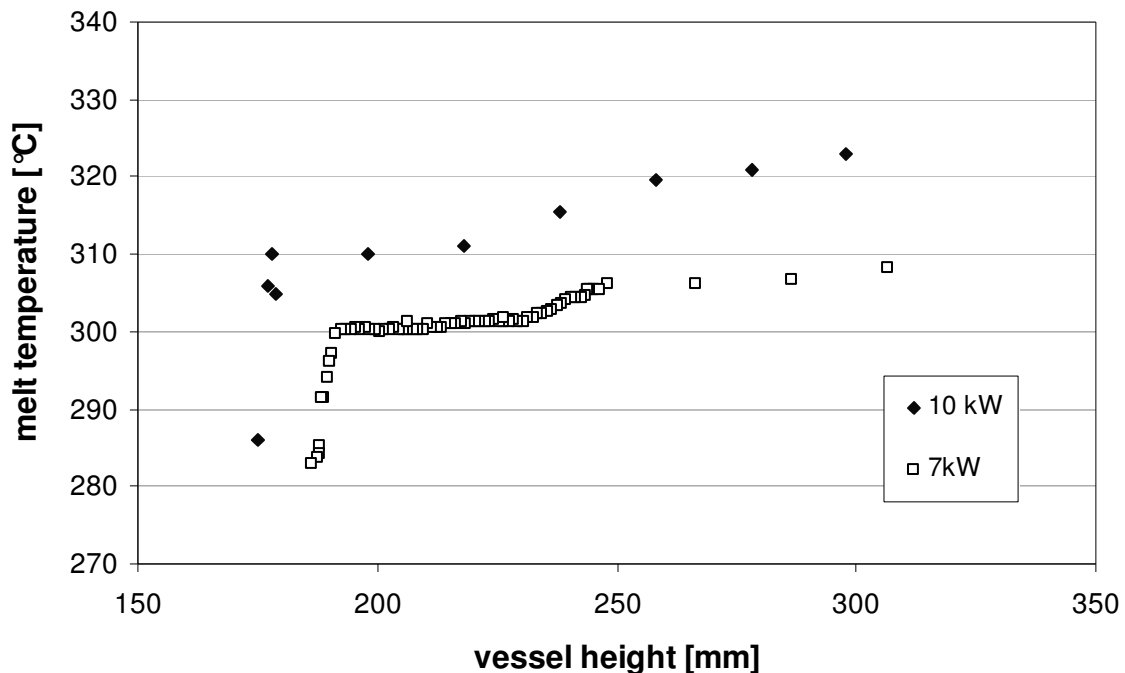
Figure 27: Melt pool temperature profiles during 10 kW and 7 kW heating periods.

4.5 Post-test analysis in LIVE-L3A

As mentioned in section 4.1, about 224 kg or 119.7 l of the melt was poured into the test vessel at the beginning of the test. At the end of the test 179 kg of melt were extracted back

into the heating furnace. Thus, the mass of the crust formed on the vessel wall at the end of the test was 45 kg, which corresponds to 20 % of the total melt mass in the test vessel.

After the extraction of the melt and cool down of the test facility, the upper lid was removed from the vessel. A view into the test vessel after the test is shown in Figure 28.

The crust formed at the vessel wall can be clearly seen. The upper edge of the crust indicates the position of the melt surface during the experiment. The crust formed during melt pouring period on the left of the vessel can also be seen. The thickness of the crust was measured along two directions and crust samples were taken to investigate the crust characteristics and composition. In the following sections the detailed post-test analysis is described.

Figure 28: View of the test vessel after disassembly of the lid in LIVE-L3A.

4.5.1 Bulk melt composition in LIVE-L3A

The original melt composition and the melt composition at the end of 10 kW and 7 kW heating periods were analysed from the samples taken by a steel rod. The melt solidified on the cold surface of the rod was used for the composition analysis. The samples were dissolved in water and the composition analysis was performed by determining the content of Na and K cations in the aqueous solution. The sampling positions and sampling times were:

- Sample 0: crust from the pouring spout opening. This sample corresponds to the original melt composition.
- Sample 1: melt from the centre of the test vessel, at the end of the 10 kW phase.
- Sample 2: melt from the centre of the test vessel at the end of the 7 kW phase.

The composition of the melt and the corresponding melt liquidus temperature are given in the Table 12. The original KNO_3 concentration was 79.7 mole%. Since KNO_3 concentration in crust is distinguishingly higher than the KNO_3 concentration in the melt pool, the concentration of KNO_3 in the melt pool became lower as the crust developed. Corresponding to the change of the melt composition, the liquidus temperature of the melt pool was reduced from 283.5°C to 278.5°C. The changing bulk melt liquidus temperature also means that the melt/crust interface temperature was changing during the test period.

Table 12: Composition of the melt pool.

	Original sample (Sample 0)	End of 10 kW (Sample 1)	End of 7 kW (Sample 2)
Na/K, [w/w]	0.1497	0.1559	0.1644
K, [mol-%]	79.706	79.044	78.148
Na, [mol-%]	20.294	20.956	21.852
Na/K, [mol/mol]	0.2546	0.2651	0.2796
KNO_3, [w/o]	82.371	81.776	80.969
$NaNO_3$, [w/o]	17.629	18.224	19.031
Melt liquidus temperature, °C	283.47	281.36	278.51

4.5.2 Crust growth rate and growth period in LIVE-L3A

Some important parameters related to the melt solidification process can be determined with the temperature measured by the thermocouple trees. The detailed description of the thermocouple trees is given in section 2.4. These solidification parameters are the crust thickness development with time, the crust growth rate, the melt/crust interface temperature during solidification, the temperature gradient in the crust and the time period of crust growth. Based on these parameters, the conditions of the melt solidification can be determined. For example, whether the crust grows under undercooling conditions, and if it is the case, how long is the undercooling period. The time period of crust growth is important for the definition of the boundary conditions: within the crust growth period, the interface temperature is lower

than the bulk melt liquidus temperature; beyond this period the interface temperature is equal to the bulk melt liquidus temperature. Additionally, the crust growth velocity influences the crust porosity, crust composition, crust microstructure and most importantly, crust thermal conductivity.

The times at which the crust front arrived at the thermocouple location can be determined based on the changing slope of the cooling temperature due to the phase change. However, since only a few thermocouples were embedded in the crust, the crust growth velocity cannot be precisely determined. More accurate determination can be performed assuming that the temperature gradient in the crust at the interface is the same as in the adjacent crust. Figure 29 illustrates the calculation method.

When a crust layer with thickness "z" is between two thermocouples located at z_i and z_{i+1}, and there are at least two thermocouples embedded in the crust, which show the temperatures T_{i-1} and T_i, then the temperature gradient G near the crust front can be determined in Eq. (8):

$$G = \frac{T_i - T_{i-1}}{Z_i - Z_{i-1}} \tag{8}$$

and the crust thickness z can be calculated according to Eq (9).

$$z = z_i + \frac{T_{int} - T_i}{G} \tag{9}$$

where T_{int} is the temperature at the melt/crust interface.
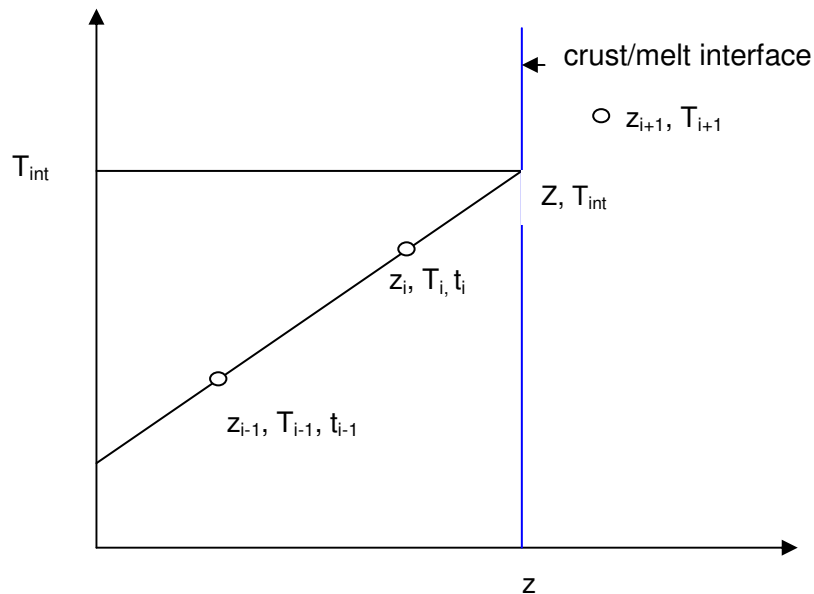
Figure 29: Determination of crust thickness during the solidification process.

Based on the calculation above, the crust thickness, the temperature gradient within the crust and the crust growth velocity can be determined. These parameters at the polar angles 37.6° and 52.9° are given in Table 13.

The parameters shown in Table 13 are subject to some deviation due to the assumption that the temperature gradient in the crust at the interface is the same as the one located inside the crust which can be measured by the next adjacent thermocouple, and the interface temperature is equal to the previous one when the crust front reaches the last thermocouple immersed in the crust layer. Nevertheless the presented determination of the crust thickness shows reliable results, as shown in Figure 30. At all positions, the crust grew fast during the initial period. For example, at polar angle 37.6° about 80% of the crust was formed during the first hour. Figure 30 also shows that the crust growth period was different at different vessel heights. The crust growth period in the lower part of the vessel was longer than in the upper parts. The time period of crust growth at polar angle 37.6° was more than 25 hours whereas this time period at 52.9° was about 1.6 hours.

Table 13: Crust temperature gradient G_s, crust thickness z and crust growth rate R during 10 kW in the LIVE-L3A test.

	CT4: 37.6°				CT2: 52.9°			
Time, s	G_s, K/mm	z, mm	R, µm/s	G_s/R, K·s/mm^2	G_s, K/mm	z, mm	R, µm/s	G_s/R, K·s/mm^2
200	18.96	7.40	9.10	2084	23.35	3.91	2.55	9167
300	17.31	8.31	9.01	1922	22.41	4.17	0.77	29140
371	16.29	8.94	7.22	2258	22.30	4.22	1.07	20794
600	14.15	10.60	6.90	2052	21.72	4.47	2.47	8809
1000	11.95	13.36	7.92	1509	18.87	5.45	1.52	12416
1400	9.36	16.52	9.97	939	17.07	6.06	0.60	28548
1600	9.16	18.52	2.24	4100	17.46	6.18	0.25	69831
2000	8.89	19.42	2.30	3857	17.41	6.28	0.41	42143
3000	8.17	21.72	1.07	7658	16.65	6.69	0.28	58837
4000	7.91	22.79	0.36	22100	16.12	6.98	0.19	84163
6000	7.70	23.50	0.18	43027	15.41	7.36	0.08	199808
9000	7.58	24.04	0.18	43279	15.06	7.59	0.02	794025
12000	7.42	24.57	0.12	63949	15.00	7.65		
16000	7.36	25.03	0.10	71782	15.00	7.66		
20000	7.28	25.44	0.20	36693	15.06	7.54		
25000	7.21	26.43	0.13	55412	15.18	7.45		
28001	6.98	26.82	0.04	181119	15.30	7.42		
40000	6.92	27.29	0.02	356024	15.36	7.37		

| 89000 | 6.80 | 28.24 | 0.02 | 331907 | 15.42 | 7.45 | | |
| 90000 | 6.80 | 28.26 | | | | | | |
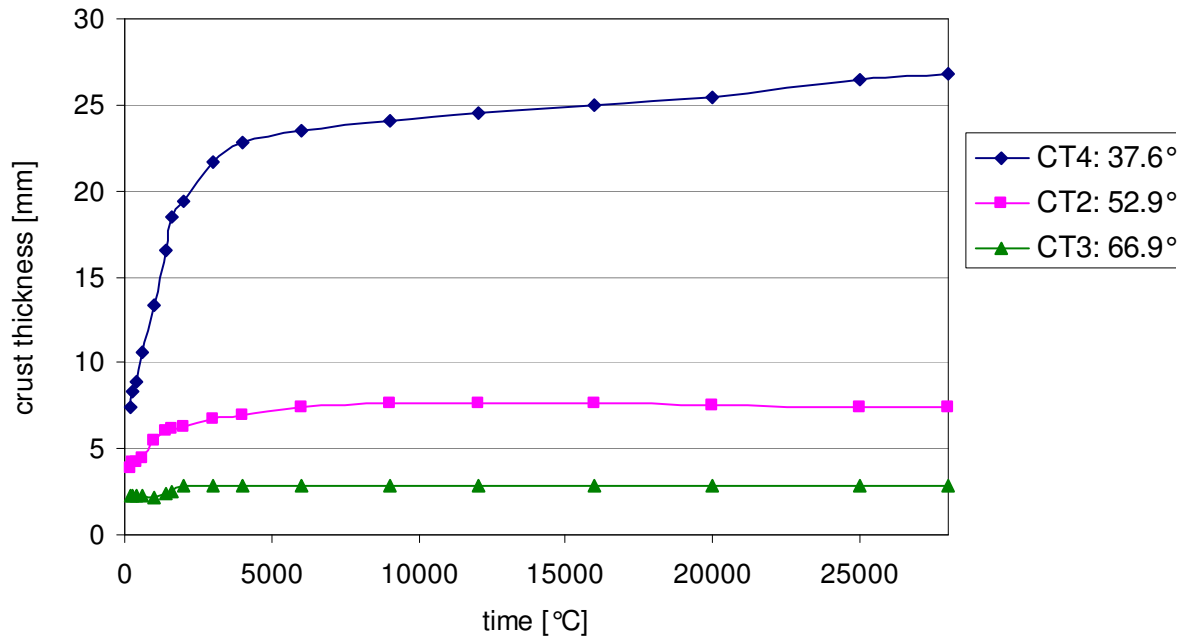
Figure 30: The development of crust thickness after melt pouring in the LIVE-L3A.

At the polar angle 66.9°, the crust growth period was influenced by the melt temperature evolution. As shown in Figure 14, in contrast with the melt temperatures in the middle and lower parts of the vessel, the melt temperature in the upper part of the pool increased slightly at the beginning and then decreased to a constant value. It took about 2000 s for the melt to reach the steady-state temperature. This time period represents also the crust growth period at the polar angle 66.9°. The crust growth rates R calculated in Table 13 are shown in Figure 31. Following behavior of the crust growth rate can be observed:

- The crust grew faster in the lower part of the vessel wall than in the middle and upper parts.
- The crust growth rate reduced significantly after 4000 s.
- The crust growth rate did not decrease continuously. Significant reduction of the crust growth velocity shortly after the melt pouring is observed. After this period the crust growth rate was recovered shortly and then was reduced again.

The temperature gradient within the crust "G_s" is shown in Figure 32. Since the heat flux through the crust layer to the vessel wall was higher in the upper part of the vessel, the temperature gradient in the upper part of the crust was also higher. After ~6000 s the temperature gradient in the crust at polar angle 52.9° was about 15 K/mm, whereas at the 37.6° position this value was about 7 K/mm.

43
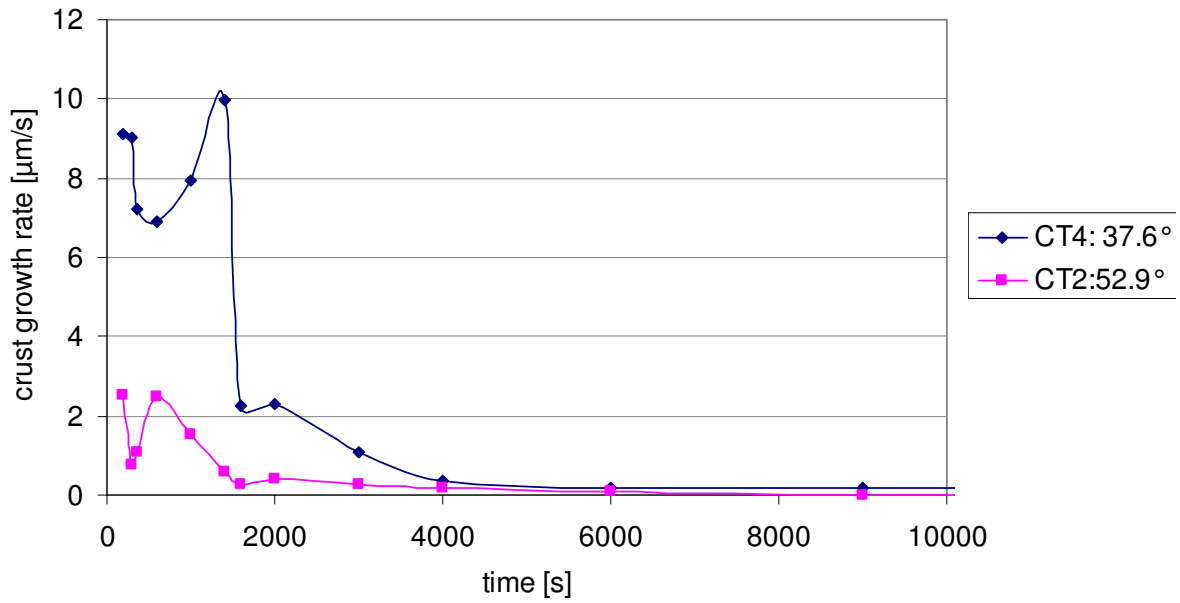
Figure 31: Crust growth rate in LIVE-L3A.
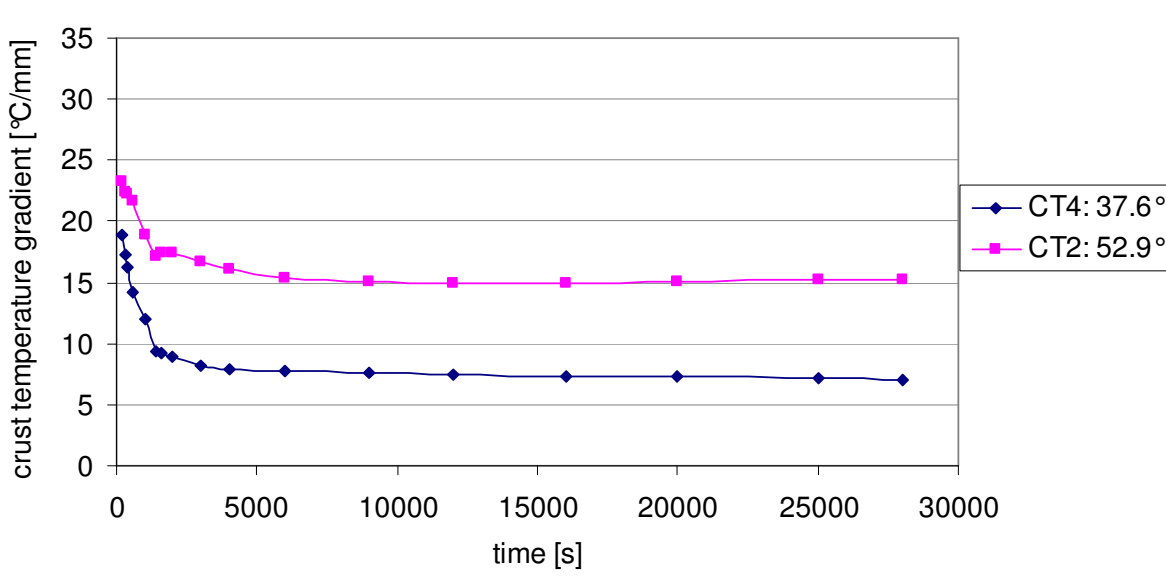
Figure 32: Temperature gradient in the crust layer near the crust/melt interface.

The cooling conditions during the melt solidification are also examined. The question is whether the crust solidifies under supercooling conditions [19]. If this was the case, then what was the time period of the undercooling. For binary melts the supercooling condition should fulfil at least the "constitutional supercooling" conditions, when the temperature of a liquid ahead of the solid-liquid interface is lower than the liquidus temperature. The word "constitutional" means that the supercooling arises from the change in the melt composition and not in the melt temperature [13]. Under the supercooling condition a mushy zone exists,

and beyond this period, a planar crust front exists. The constitutional supercooling condition is fulfilled when the Eq. (10) is satisfied.

$$\frac{G_L}{R} \leq \frac{m_L C_0 (1-k)}{k D_L} \tag{10}$$

where

G_L is the actual temperature gradient in the liquid at the interface;

R is the rate of solidification;

m_L is the slope of the liquidus line of the local melt;

k is the equilibrium partition ratio C_s/C_0;

C_s is the solute concentration (here $NaNO_3$) in solid;

C_0 is the solute concentration (here $NaNO_3$) in bulk liquid;

D_L is the self diffusion coefficient of the solute in the liquid (here $NaNO_3$).

Since the thermal conductivity in the liquid melt is similar to that in the solid crust, the temperature gradient in the liquid G_L is replaced by the temperature gradient within the crust G_s. The calculated values of G_s/R are shown in Table 13 for the following melt properties:

m_L: -2.42 °C/(mol%),

k: 0.2 taken from the reference [14],

C_0:   20 mol% $NaNO_3$,

D_L: 0.002 mm²/s, taken from the references [15] and [16].

The right side of the Eq. (10) amounts 96800 K·s/mm². Comparing the value of G_s/R in the Table 13 with this criterion, the time period of the crust growth under supercooling conditions can be obtained. This time period is different at different locations and amounts to 25000 s at polar angle 37.6° and to 4000 s at polar angle 52.9°.

4.5.3   Crust morphology in LIVE-L3A

The crust thickness profiles along the vessel wall were measured after the test at the azimuth direction of the melt pouring (157.5°-337.5°) and at the direction perpendicular to the melt pouring (247.5°-67.5°). In Figure 33 the crust thickness profiles at these two directions are shown. Also the exact position of the melt surface during the test can be determined. The crust thickness during the 7 kW heating power was in the range from 10 mm at the melt surface and ~50 mm at the vessel bottom. No significant asymmetry of the crust thickness can be observed, as shown in **Fehler! Verweisquelle konnte nicht gefunden werden.**. This indicates that the asymmetric melt pouring position (azimuthal angle 157.5°, polar angle 52°-72°) has almost no influence on the final crust thickness.
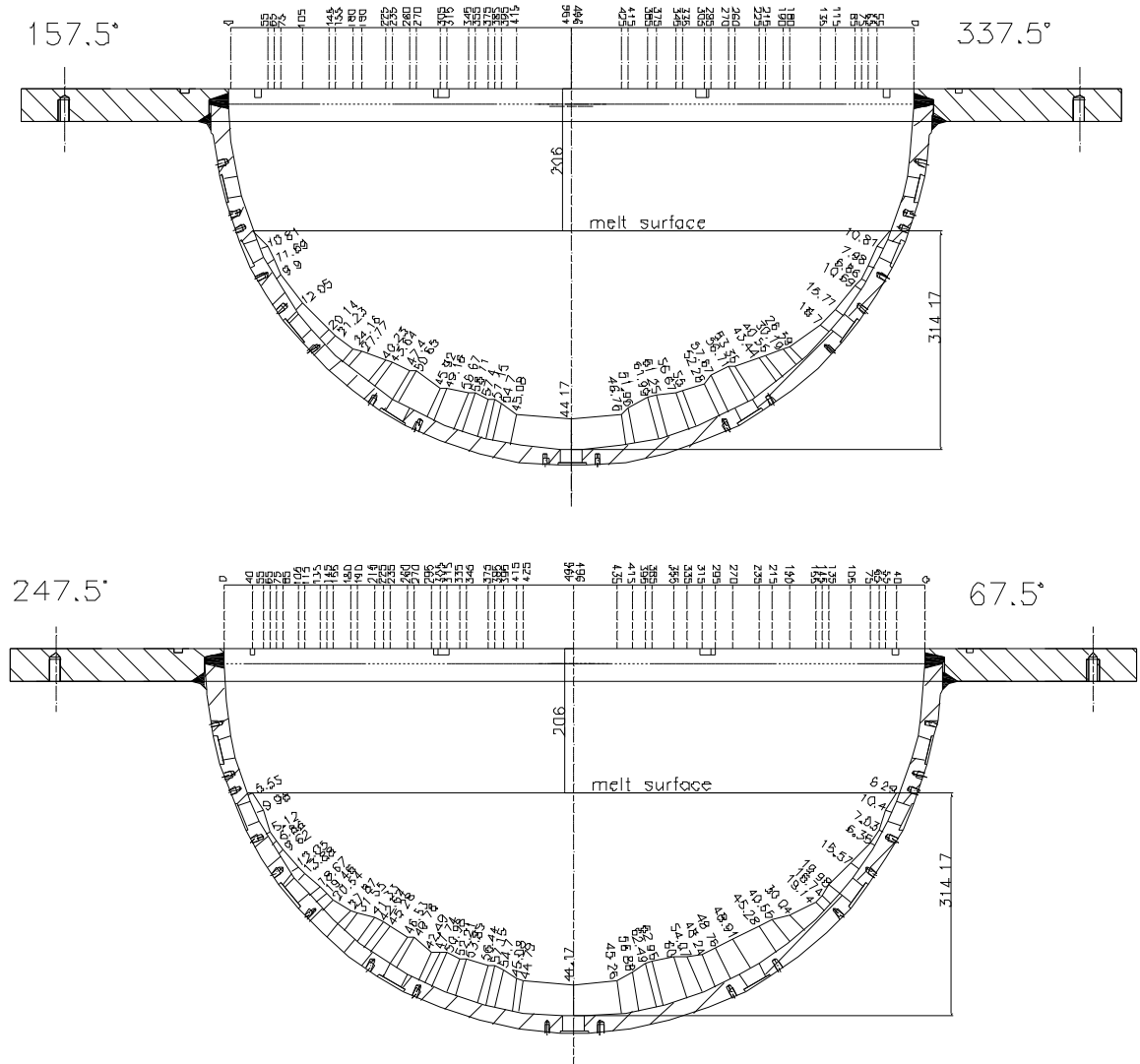
Figure 33: Crust thickness profiles at the end of LIVE L3A.
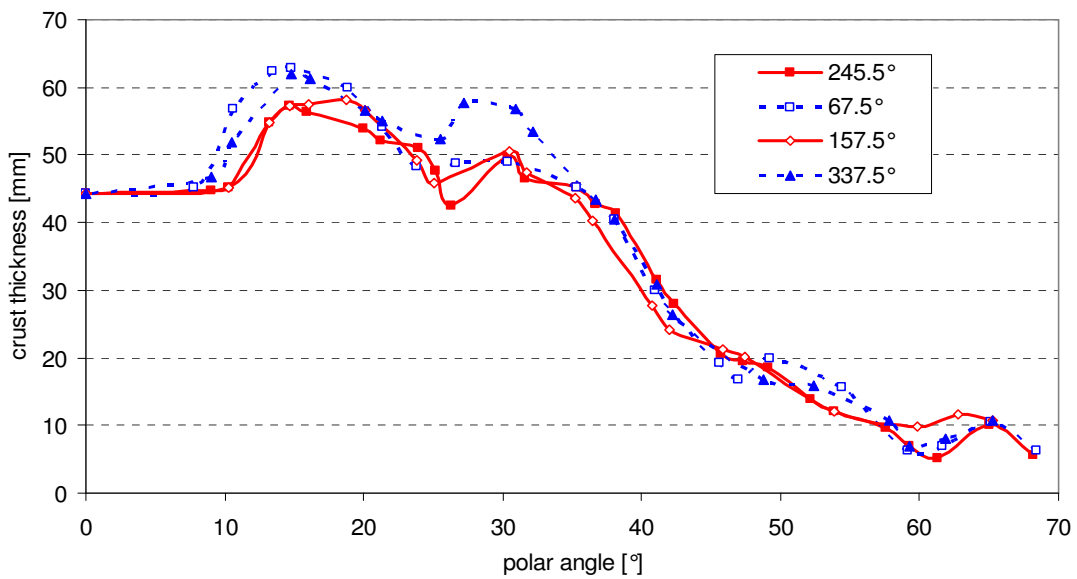
Figure 34: Comparison of crust thickness at four different locations.

The microstructure and the composition of the crust were examined with SEM (scanning.electron microscopy). 17 mm thick crust sample taken from the location at polar angle 55° was analysed. In Figure 35 the images across the crust layer from the melt/crust interface to the crust/wall interface are shown.

0 mm to crust front (at melt/crust interface)

4 mm to crust front (inner layer)

10 mm to crust front (outer layer)

14 mm to crust front (outer layer)

17 mm to crust front (at crust/wall)
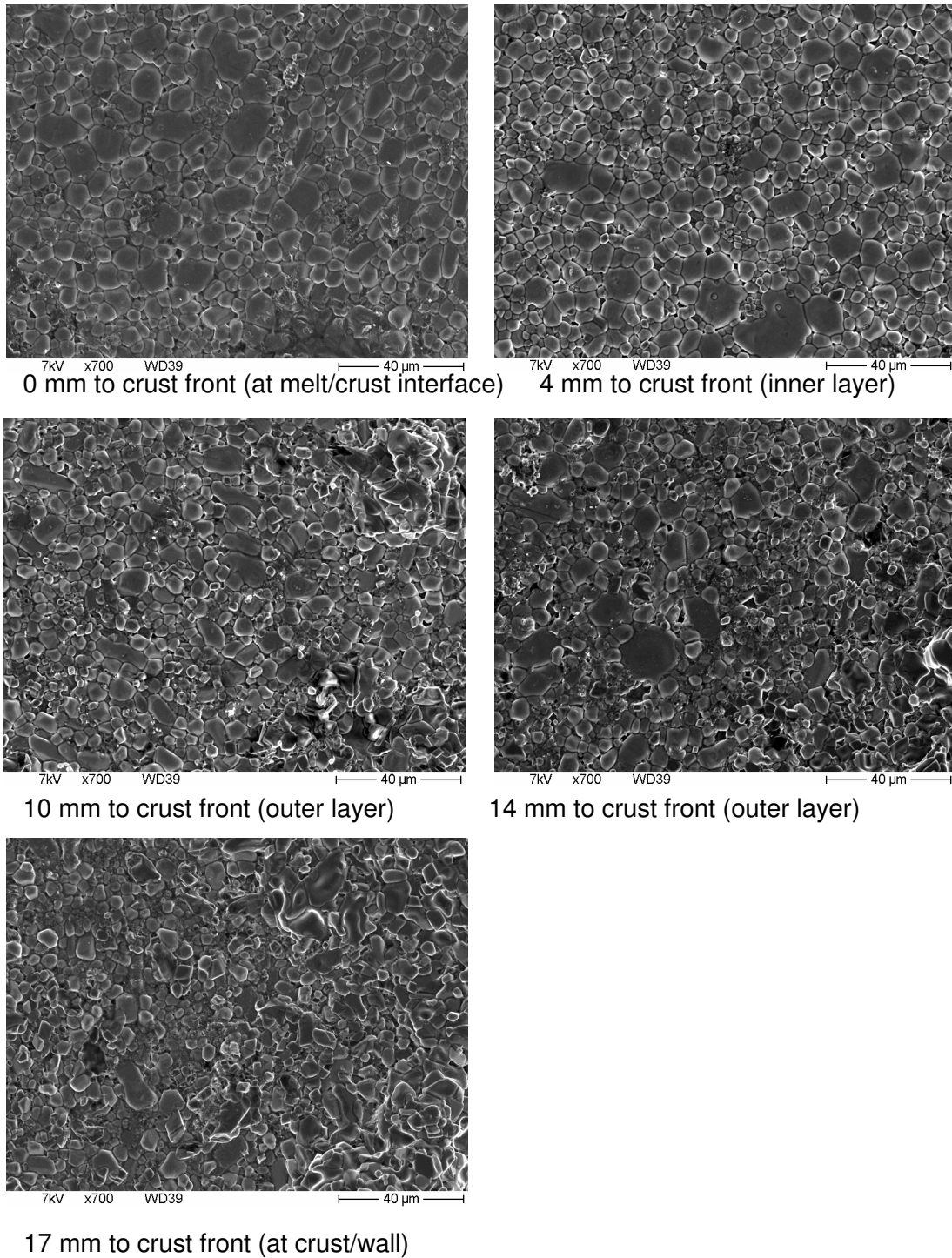
Figure 35: Examples of the crust microstructure at different locations from the melt/crust interface to the crust/wall interface.

A two-layer structure was formed in the crust due to 10 kW and 7 kW heating periods. At the examined crust position the outer layer (formed during the 10 kW heating period) is about 8 mm, the inner layer is about 9 mm thick. Therefore, the images shown in Figure 35 at 0 mm and 4 mm show the crust formed during the 7 kW heating period. The other images relate to the crust formed during the 10 kW heating period. The microstructure through the cross section of the crust shows heterogeneous character of the grain size distribution. Moreover, the crust layer formed during 10 kW heat generation (images of 10 mm, 14 mm and 17 mm) was looser and more porous, resulting from rapid solidification.

As the crust cools down, stresses are generated within the crust due to the shrinkage. It is observed that the manner of the stress relief was different between the two layers. The image in Figure 36 left indicates that minor cracks appeared parallel to the vessel wall, whereas in the inner crust layer large through-layer cracks are observed perpendicular to the vessel wall. The minor cracks resulted from the slow cooling during the solidification process, whereas the large cracks could be generated during the fast cooling at the end of the test after the liquid melt extraction and fast cooldown of the crust.
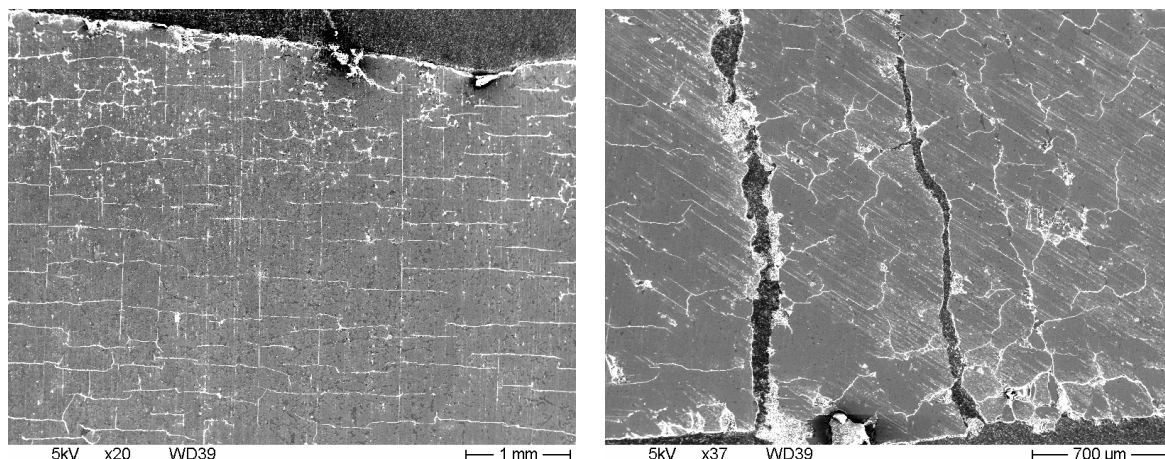
Figure 36: Minor cracks in the outer crust layer (left) and large through-layer cracks in the inner layer of the crust (right).

Elemental composition of the different crust layers was determined with energy dispersive X-ray (EDX). The error range of the analysis was examined by analysing the standard samples. It was found out that the error is within ~1 mole %. In Figure 37 the concentration of KNO_3 across the crust layer is shown. The crust composition corresponds to the local melt composition which is a parameter of crust solidification rate and the diffusion rate of $NaNO_3$. During the solidification of KNO_3-rich crust, $NaNO_3$ is rejected to the melt ahead of the crust front. The sharp decrease of KNO_3 content in the crust layer appr. 0.5 mm away from the vessel wall indicates that the solidification at the beginning of the test was so fast that $NaNO_3$ was highly enriched in the local melt ahead of the crust front. A similar phenomenon occurred

after the 10 kW heating power was switched to 7 KW. Since the solidification rate was lower in this case, the decrease of the KNO_3 concentration was lower as well. The concentration of the crust at the end of the solidification process indicates that the solidus concentration of the actual melt was about 90 mole %.
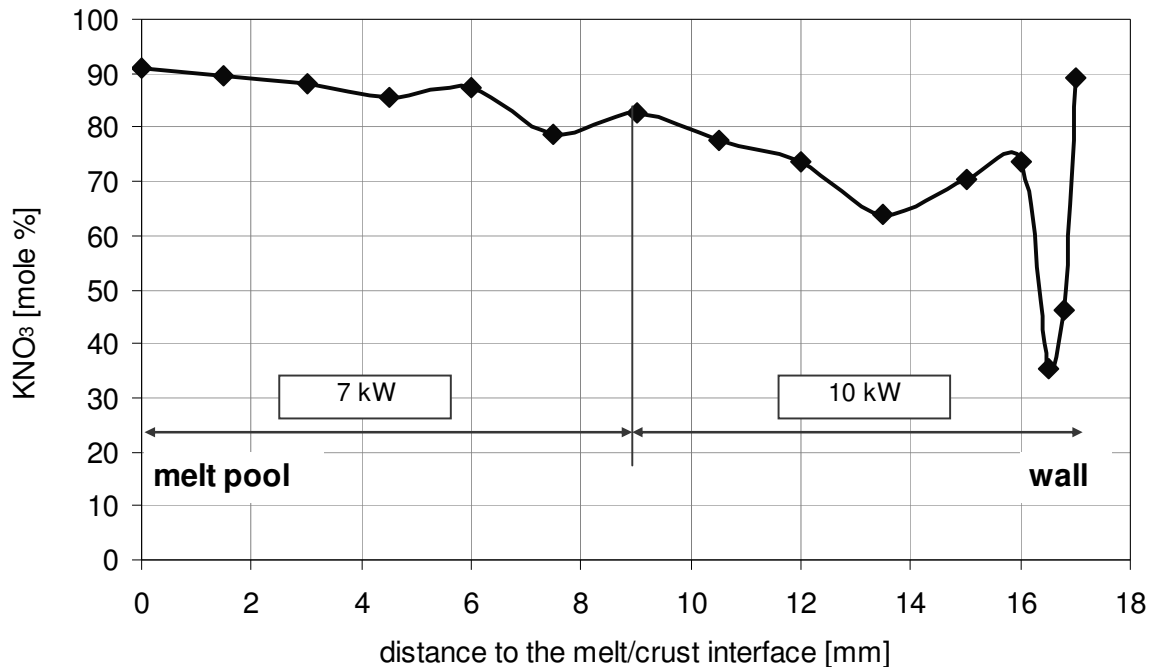
Figure 37: SEM-EDX analysis of KNO_3 concentration across the crust layer.

4.5.4 Crust liquidus temperature and crust composition in LIVE-L3A

Crust samples from the positions of CT2 (polar angle 52.9°) and CT3 (polar angle 66.9°) were taken after the test for the crust liquidus temperature determination. The crust at the position of CT4 (polar angle 37.6°) cannot be accessed due to the heating wires and the cage. The crust thickness after the 7 kW heating period at the positions of 52.9° and 66.9° is about 15 mm and 9 mm respectively. For the 9 mm thick crust seven measurement points across the crust layer were selected; for the 15 mm thick crust eight measurement points were selected.

The crust liquidus temperature was determined with "Optimelt", a melting temperature analysis device which detects the image change in three powder-loaded capillary tubes during controlled heat up period. Sampling material was grounded and well mixed before loaded to the capillary tubes. Comparing with the cooldown method for melting point determination the accuracy of this method is within 4 degrees. In Table 14 the measuring position, crust liquidus temperature and the corresponding concentration of KNO_3 in the crust are listed. The composition at these sampling positions was determined according to the phase diagram, which is shown in Table 1.

Table 14: Crust composition and liquidus temperature and in the LIVE-L3A test.

CT2 (52.9°)	Distance to wall [mm]	Liquidus temp. [°C]	Mole % KNO_3	CT3 (66.9°)	Distance to wall [mm]	Liquidus temp. [°C]	Mole % KNO_3
15_0	0	312.0	90.92	9_0	0	312	90.92
15_1.5	1.5	304.0	87.23	9_1.5	1.5	284	79.81
15_3	3	281.5	79.61	9_3	3	292	81.96
15_6	6	291.9	82.46	9_4.5	4.5	302	86.86
15_9	9	302.6	86.71	9_6	6	314	91.74
15_12	12	315.0	92.32	9_7.5	7.5	318	93.58
15_13.5	13.5	310.0	89.95	9_In	9	323	95.73
15_In	15	321.6	95.02				
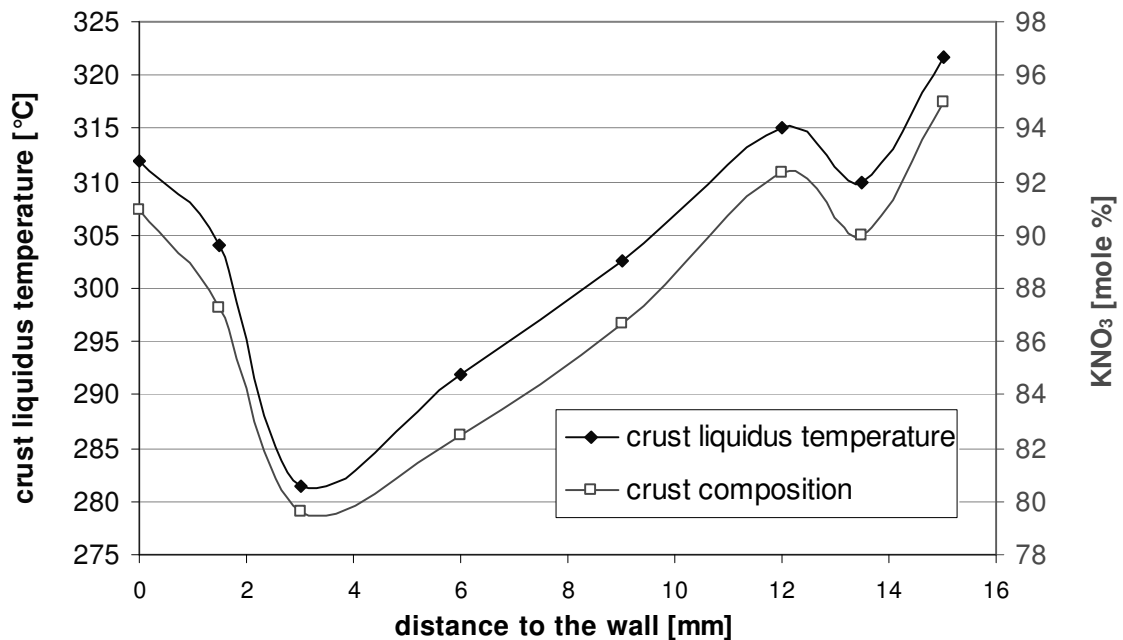
Figure 38: Crust liquidus temperature and crust composition at polar angle 52.9° in the LIVE-L3A test analysed by Optimelt melting method.

The crust liquidus temperature and composition are also shown in Figure 38. The results are in a good agreement with the SEM-EDX analysis shown in Figure 37. The low value of KNO_3 concentration near the crust outer surface could not be exactly measured due to a low resolution of the Optimelt device (sampling area more than 1-2 mm^2) compared to EDX (0.06 mm^2). Moreover, higher KNO_3 concentration was determined by the Optimelt method in comparison to the SEM-EDX (Figure 37). This difference can be explained by the measurement principles of the two different methods. SEM-EDX determines an average composition of a small area, whereas the Optimelt device measures the liquidus temperature of the com-

ponent with the highest liquidus temperature in the area. For example, in the innermost layer of the crust adjacent to the melt pool, KNO_3-enriched phases with KNO_3 concentration of 95 mole% were detected by Optimelt, whereas the average composition at this position detected by EDX is about 90% KNO_3. The non-uniform crust liquidus temperature across the crust layer also implies a changing boundary temperature at the crust/melt pool interface during the thermal hydraulic transient state.

4.5.5 Crust porosity and thermal conductivity in LIVE-L3A

To analyze the cumulative pore volume and pore size distribution, mercury porosimetry technique was used. The technique involves the intrusion of mercury at high pressure into the investigated sample. The pore size can be determined based on the external pressure needed to force the mercury into pores against the opposing force of the mercury's surface tension. Samples from the outer layer (formed during 10 kW phase) and the inner layer (formed during 7 kW phase) of a 25 mm thick crust sample were investigated. The results of the porosity and the pore size distribution measurements are given in Table 15.

Table 15: Porosity and pore size distribution of crust layers in the LIVE-L3A test.

	Inner layer (7 kW)		Outer layer (10 kW)	
Total cumulative volume, mm³/g	16.27		27.20	
Total porosity, %	3.26		5.52	
Bulk density, g/cm³	2.01		2.03	
Apparent density, g/cm³	2.07		2.15	
Pore size distribution				
Pore radius range, µm	Relative volume, mm³/g	Relative volume, %	Relative volume, mm³/g	Relative volume, %
100000-2000	8.45	51.94	10.96	40.29
2000-1	7.82	48.06	16.24	59.71

The total porosity of the outer crust layer (5.52%) was higher than the porosity of the inner crust layer (3.26%). The higher porosity of the outer layer mainly resulted from the volume of fine pores between 1-2000 µm, as shown in Figure 39. Since large pores could result from the crack formation during fast cooldown (e.g. at the end of the test after the melt extraction), the porosity of the inner crust layer during the LIVE-L3A test could be even lower than the value determined after the test.
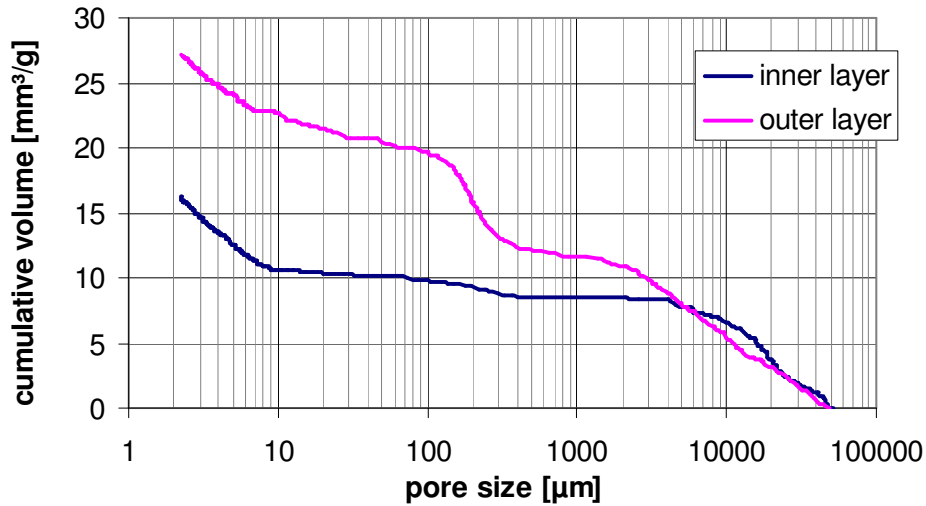
Figure 39: Pore size distribution in the inner and outer crust layers in the LIVE-L3A test.

The crust thermal conductivity is calculated according to the temperature difference measured across the crust layer at the position of CT thermocouple trees and the calculated heat flux as described in the previous section 4.4.1. During the steady-state of 10 kW and 7 kW heat generation, the crust local thermal conductivity at the positions of CT4 and CT2 thermocouple trees are shown in Table 16.

Table 16: Crust thermal conductivity evaluated in the LIVE-L3A test.

Thermocouple tree	distance to wall, mm	10 kW at 50000s			7 kW at 150000s		
		ΔT, K	Heat flux, W/m²	Therm. conduct., W/mK	ΔT, K	Heat flux, W/m²	Therm. conduct., W/mK
CT4 at 37.6°	0	65.12	3771	0.52	48.32	2558	0.48
	9	61.16	3771	0.55	45.25	2558	0.51
	18	59.92	3771	0.57	44.96	2558	0.51
	27				40.75	2558	0.56
Mean value:				0.55			0.51
CT2 at 52.9°	0	43.44	6883	0.48	28.78	4068	0.42
	3	49.06	6883	0.42	30.22	4068	0.40
	6				23.96	4068	0.51
	9				26.81	4068	0.46
Mean value			:	0.45			0.44
CT3 at 66.9°	0				68.36	9138	0.40

The crust thermal conductivity varied between 0.4 and 0.6 W/mK. The crust thermal conductivity at the same crust position during the 10 kW phase was higher than during the 7 kW phase. This indicates the dependence of the crust thermal conductivity on temperature. It is also noted that the thermal conductivity of the crust near the melt pool was higher than near the vessel wall. Three observations could contribute to this result: (1) the dependence of the crust thermal conductivity on temperature; (2) different microstructure and porositiy of the two crust layers [17] and (3) different composition in the crust [18]. The last two facts are related with the solidification process.

5 Comparison of the LIVE-L3A and LIVE-L3 results

The results obtained in the LIVE-L3 and LIVE-L3A tests are compared in this section in order to understand the impact of cooling conditions on the molten pool heat transfer and crust solidification behaviour. The main difference of the test conditions between the LIVE-L3 and LIVE-L3A tests were the initial boundary conditions. At the beginning of the LIVE-L3 test the vessel was cooled by air from the outside. This rather inefficient cooling led to the increase of the melt pool temperatures and melt-down of the crust initially formed at the upper location of the vessel wall. Water cooling was started 7199s after the melt pouring resulting in a cool-down of the test vessel wall and formation of a new crust layer at the upper location of the vessel wall. In the LIVE-L3A test the cooling of the outer vessel wall started already at the beginning of the test. During the LIVE-L3 test the crust was formed in slow cooling conditions after the initiation of the water flooding since the melt temperature was very high and the hot vessel wall was first cooled down, whereas the crust in the LIVE-L3A test was formed under fast cooling condition when the hot melt touched the cold vessel wall during the melt pouring period. These different cooling conditions during the initial period significantly influenced the crust growth behaviour and the thermal hydraulics in the melt pool during the thermal hydraulic steady-state. The dependence of the following parameters on the cooling conditions is discussed, starting with the melt temperature, followed by crust growth rate and crust thermal conductivity, then crust thickness profile and finally the heat flux distribution through the vessel wall and heat flux splitting. Wall inner temperature and the parameters of the cooling water are also compared to get a better understanding of the obtained results.

5.1 Melt temperature

The melt temperatures at 70 mm, 170 mm and 270 mm vessel height are compared between the LIVE-L3 and LIVE-L3A tests at the radius of 74 mm. Figure 40 shows the melt temperature distribution during the initial period in both tests.

Figure 40 indicates also that the temperature distribution in both tests has similar behaviour during first 1000 s: the temperatures in the bottom and middle parts of the melt pool decreased and in the upper part of melt pool increased, however after this period the melt temperatures in the two tests behaved differently: in the LIVE-L3 test the melt temperature increased during the air cooling period, whereas the melt temperatures in the LIVE-L3A decreased further to constant values. After the initiation of the water flooding at 7199 s in the LIVE-L3 test the melt temperatures decreased also to constant values.
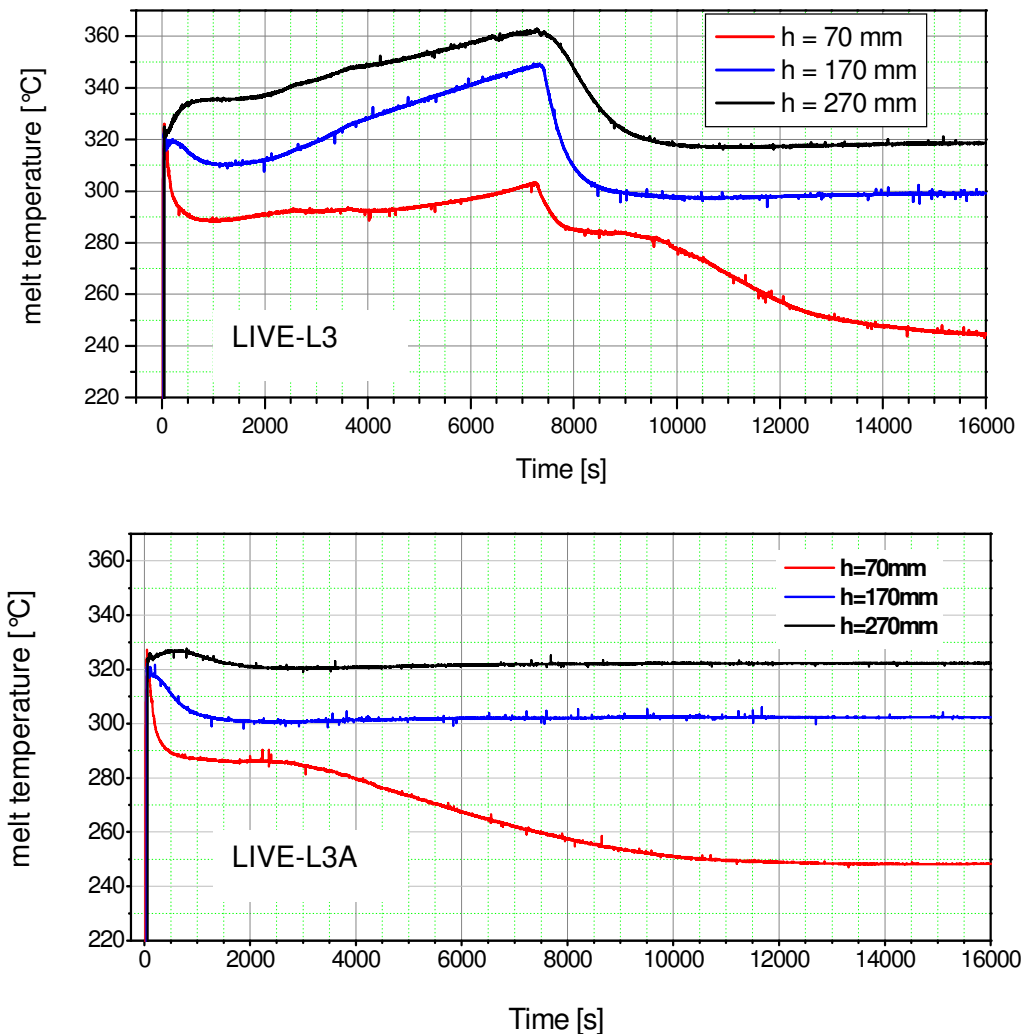
Figure 40: Melt temperature development during the initial period in LIVE-L3 and LIVE-L3A tests.

During the thermal hydraulic steady-state the melt temperature in the LIVE-L3A test were generally 3 ℃ to 5 ℃ higher than those measured in the LIVE-L3, as it is shown in Figure 41, although the wall inner temperatures (IT temperature) in the LIVE-L3A were slightly lower compared to the LIVE-L3 test. This indicates that the heat resistance of the crust layer in the LIVE-L3A was somewhat higher than in the LIVE-L3 test.

Large horizontal deviation in the melt temperature distribution in the lower part of the melt pool close to the vessel wall is observed, e.g. at the location of 70 mm height and at the radius 174 mm attributed to the crust formation at these positions. During the LIVE-L3A test in which the overall melt temperature was slightly higher, 3/4 of the vessel circumference was

embedded within the crust layer, whereas during the LIVE-L3 test the whole circumference was covered by the crust at this location.
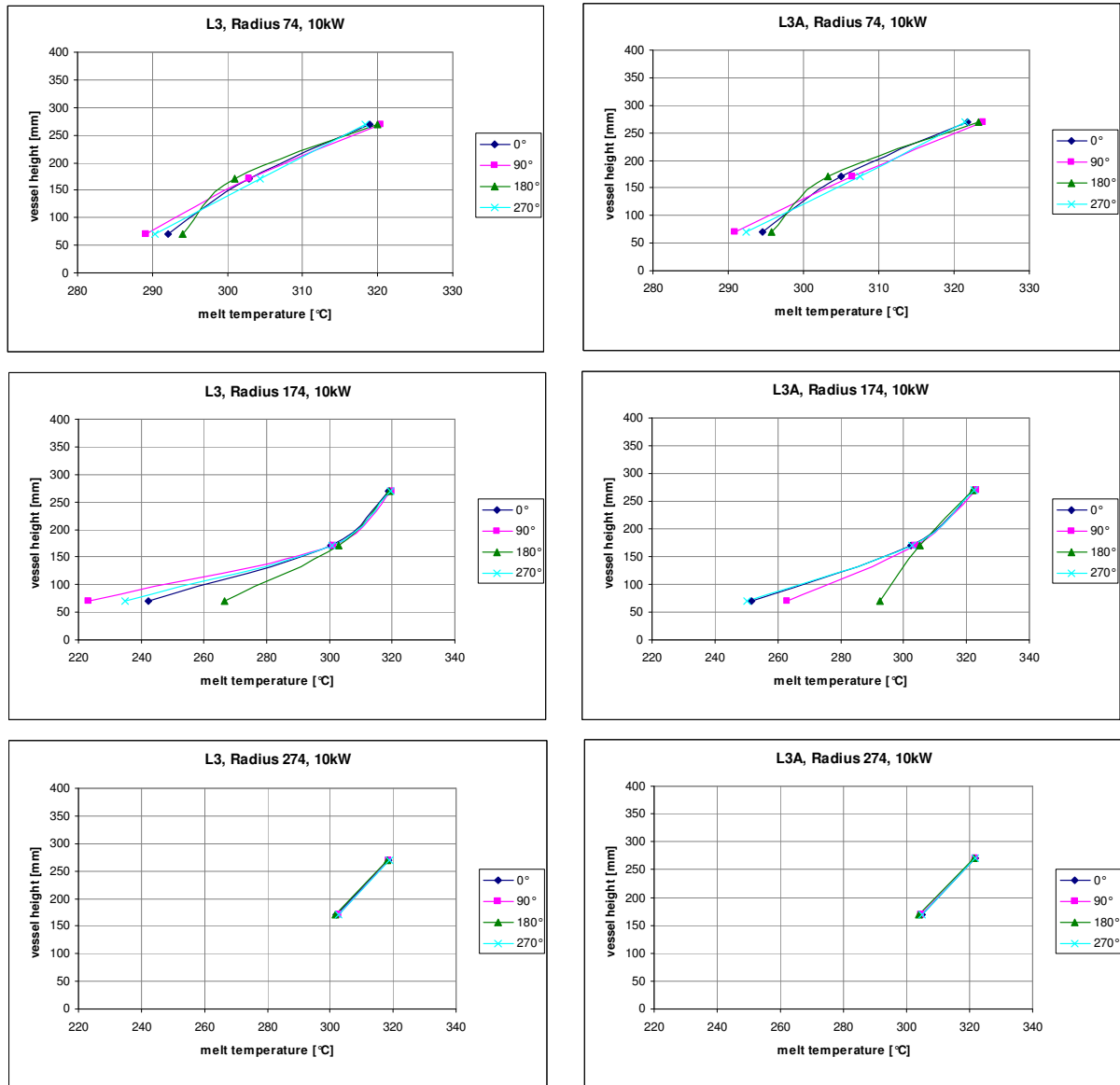
Figure 41: Melt temperature distribution in the LIVE-L3 and LIVE-L3A tests.

5.2 Crust growth characteristics

The development of the crust thickness at polar angles 37.6° and 52.9° during the two tests is shown in Figure 42. In the LIVE-L3 test the start time of the crust growth was the beginning of the water flooding, i.e. 7199 s after the melt pouring.

Several phenomena can be observed in the Figure 42. (1) At both positions the crust layer in the LIVE-L3A test developed faster than in the LIVE-L3 test during the initial period. The time

period in which L3A crust was thicker than L3 crust were ~1000 and ~1600 s at polar angles 37.6° and 52.9° respectively. At the end of these periods the crust thickness in the LIVE-L3A reached ~48% of the final thickness at polar angle 37.6% and ~88% of the final thickness at 52.9°. This indicates that more than 50% of the crust layer in the LIVE-L3A test formed faster compared to the same crust position in the LIVE-L3 test; (2) the final crust layer thickness in the LIVE-L3A test was thinner. At the polar angle 37.6° the final crust thickness in the LIVE-L3A test was only ~80% of the corresponding crust layer thickness in the LIVE-L3 test and at the polar angle 52.9° the final crust thickness was ~60% compared to the LIVE-L3 test; (3) the total crust growth period in the LIVE-L3A was shorter than in the LIVE-L3 test. The crust growth period will be discussed in detail with respect to the G/R ratio (existence of constitutional supercooling conditions).
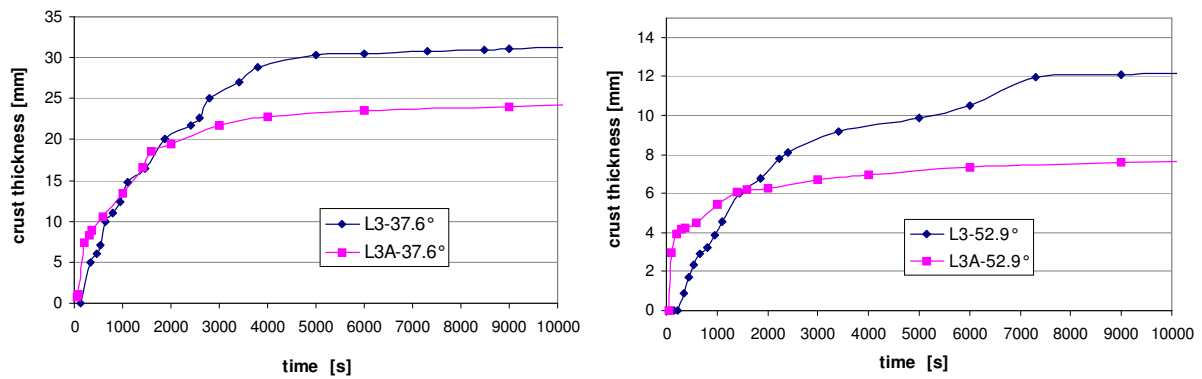
Figure 42: Comparison of the crust thickness development
in the LIVE-L3 and LIVE-L3A tests.

The crust growth rates are compared between the LIVE-L3 and LIVE-L3A at polar angles of 37.6° and 52.9°, as shown in Figure 43. The highest crust growth rate was measured at the beginning of the LIVE-L3A test and amounted to 0.06 mm/s. The initial crust growth rate was generally higher in the LIVE-L3A test than in the LIVE-L3 test: at 37.6° the crust growth rate was about twice as high as in the LIVE-L3 test (Figure 43 (a)), and at 52.9° the initial crust growth rate in the LIVE-L3A was about 10 times higher than in the LIVE-L3 test (Figure 43 (b)). The time periods in which the LIVE-L3A crust growth rate exceeded the one determined in the LIVE-L3 were 200 s at 37.6° and 600 s at 52.9°. After these periods, the crust in the LIVE-L3 test developed faster.

Based on the crust growth rate the constitutional supercooling conditions in the two tests were examined. As described in the section 4.5.2, the constitutional supercooling condition depends on the ratio of the temperature gradient in the fluid at the interface to the crust growth rate: G/R. The temperature gradient in the fluid in the two tests was not directly

measured. However, due to the similar thermal conductivity between the liquid and the solid of the simulant material, the temperature gradients in the crust layer near the melt/crust inter-face were applied for the evaluation. Figure 44 shows the temperature gradients at two polar angles 37.6° and 52.9° in the two tests.
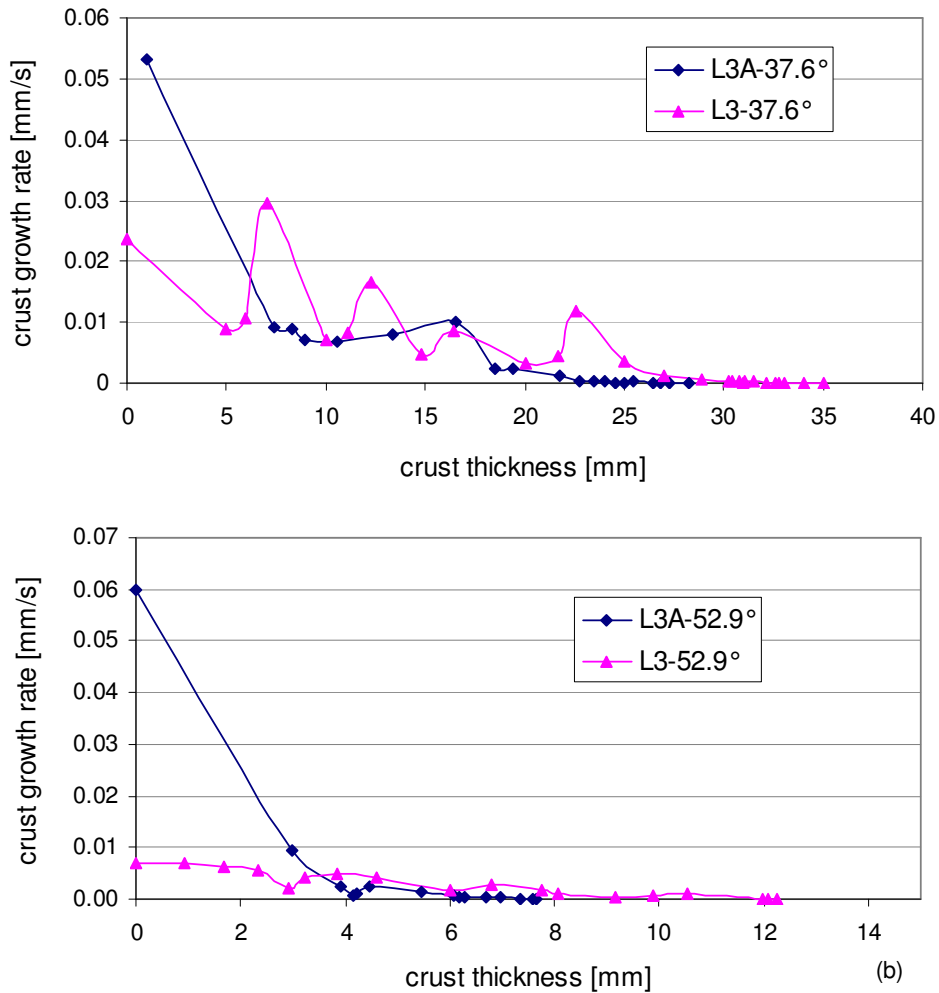
Figure 43: Comparison of the crust growth rates between the LIVE-L3 and LIVE-L3A tests.
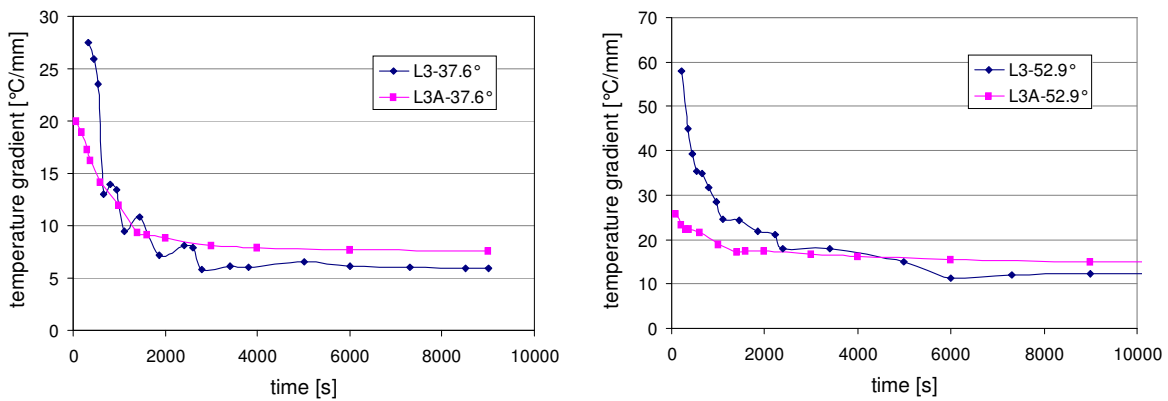
Figure 44: Temperature gradient in the crust at polar angles 37.6° (left) and 52.9° (right).

Figure 44 shows that the temperature gradient was not constant during the test period and was not the same at different vessel heights. The temperature gradient in the LIVE-L3A test in the beginning was lower, and the time to reach the steady-state conditions was also shorter. During the thermal hydraulic steady-state the temperature gradient near the melt/crust interface in the LIVE-L3A was higher compared to the LIVE-L3 results.

When the G/R ratio is larger than ~10^5 K·s/mm^2, as discussed in the section 4.5.2, the crust solidifies under equilibrium conditions and the crust/melt interface is planar. The times when the crust front changed from the constitutional supercooling-controlled cellular structure to the equilibrium solidification-controlled planar front are given in Table 17. No apparent difference in the time of transition can be found at 37.6° between the two tests, whereas at the 52.9° the crust solidification period under the constitutional supercooling conditions in the LIVE-L3A was shorter.

The crust growth period at the polar angle 66.9° was not compared since the crust growth was not only determined by the heat and mass transfer between the crust and the melt, but was also strongly dependent on the stabilization time period of local melt temperature.

Table 17: Time period to reach equilibrium solidification conditions in the LIVE-L3 and LIVE-L3A tests.

Polar angle	LIVE-L3	LIVE-L3A
37.6°	22000 s or 6.1 hours	25000 s or 6.9 hours
52.9°	6000 s or 100 min	4000 s or 67 min

5.3 Crust porosity and thermal conductivity

The crust porosities of the outer (the layer adjacent to the vessel wall) and inner layer (the crust layer adjacent to the melt pool) between LIVE-L3 and LIVE-L3A are presented in Table 18. The relative pore volume of the crust inner and outer layer in the LIVE-L3A test was almost twice as high as in the LIVE-L3 test, whereas the difference in the volume of large pores was negligible.

Table 18: Comparison of the crust porosity in the LIVE-L3 and LIVE-L3A tests.

Pore radius range	Specific volume, mm^3/g			
	LIVE-L3 Outer layer	LIVE-L3 Inner layer	LIVE-L3A Outer layer	LIVE-L3A Inner layer
100000-2000, µm	8.22	8.14	10.96	8.45
2000-2, µm	8.69	4.45	16.24	7.82
Porosity, %	3.46	2.6	5.52	3.26

The thermal conductivity at polar angles 37.6° and 52.9° was also compared. The mean thermal conductivities of the outer layers (formed during 10 kW period) and of the whole layers are presented in the Table 19. The crust thermal conductivities varied from 0.41 to 0.69 W/mK depending on the vessel height and crust temperature. At both 37.6° and 52.9° locations the heat conductivity of the crust in the LIVE-L3A test was lower than in the LIVE-L3, e.g. at the polar angle 37.6° the crust thermal conductivity in the LIVE-L3A was 20 % lower compared to the LIVE-L3. The thermal conductivity of the outer crust layers decreased from ~7 to ~10 % when the heating power changed from 10 kW to 7 kW indicating the dependence of the crust thermal conductivity on the crust temperature. The effective thermal conductivity of the whole crust layer was higher than the thermal conductivity of the outer layer, meaning that the inner crust layer (formed during the 7 kW heating period) had higher thermal conductivity than the outer crust layer. The reasons of this phenomenon were explained in 4.5.5.

Table 19: Crust thermal conductivities (W/mK) at polar angles 37.6° and 52.9°.

	outer layer (10 kW)		outer layer (7 kW)		whole layer (7 kW),	
	37.6°	52.9°	37.6°	52.9°	37.6°	52.9°
L3	0.690	0.475	0.649	0.446	-	0.458
L3A	0.547	0.446	0.499	0.414	0.514	0.445

5.4 Crust thickness

The crust thickness profiles after the melt extraction at the end of the two tests are compared in Figure 45. The initial crust layer formed above the polar angle 30° in the LIVE-L3 test was molten during the air cooling phase before the water flooding at 7199 s after melt pouring as a result of elevated melt pool temperatures. The upper part of the crust layer in the LIVE-L3 was about 15-30% thicker than in the LIVE-L3A at the end of the 7 kW heating period. The pits in the crust profiles at the vessel bottom at the polar angle ~25° resulted from heating wires embedded in the crust. Crust growth at the end of the test after the power shutdown cannot be detected.

There are some indications that during the steady-state of 10 kW the crust layer in the LIVE-L3A test was also thinner than in the LIVE-L3 test. The crust thicknesses estimated by the crust temperature measurements at 37.6°, 52.9° and 66.9° (Figure C-17 to Figure C-19) during the steady-state of 10 kW are given in Table 20.
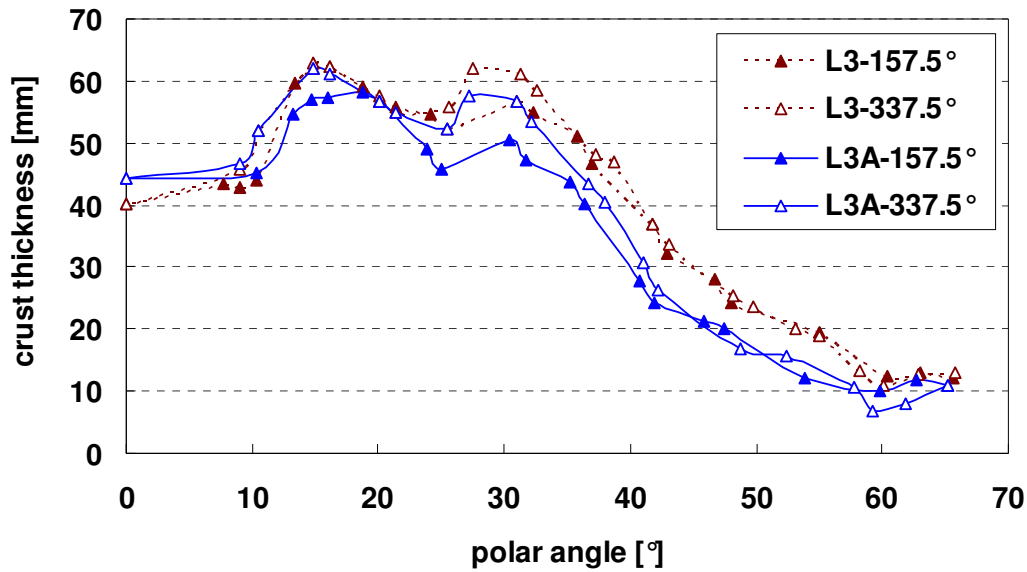
Figure 45: Comparison of the crust thickness in the LIVE-L3 and LIVE-L3A tests at the end of the 7 kW heating period.

Table 20: Crust thickness at the end of the 10 kW heating period.

Polar angle	Crust thickness in LIVE-L3 during 10 kW, mm	Crust thickness in LIVE-L3A during 10 kW, mm
37.6° (CT1/CT4)	35.9	28
52.9° (CT2)	12.5	7.5
66.9° (CT3)	3.4	2.8

Correspondingly to the crust thickness the total mass of the crust was also different in the two tests. In the LIVE-L3 test 57 kg was found solidified corresponding to 23.5% of the total melt mass, whereas in the LIVE-L3A this value amounted to 47 kg, representing 20.8% of the total melt mass.

5.5 Heat flux

The comparison of the heat flux distribution in the LIVE-L3 and LIVE-L3A tests demonstrates significant differences in both horizontal and vertical heat flux distribution. Figure 46 shows the heat fluxes at four azimuthal angles in the LIVE-L3 and LIVE-L3A tests. The heat fluxes in the LIVE-L3A test near the melt pour position (between azimuth 112.5° and 202.5° and at the polar angle 65.5°) were higher than the heat flux at the same position measured in the LIVE-L3 test. The heat flux scattering in the LIVE-L3A was larger than in the LIVE-L3 in the upper part of the melt pool, e.g., the scattering of the heat flux at the polar angle 65.5° in the LIVE-L3A was 31.8% compared to the heat flux mean value, whereas the scattering in the

LIVE-L3 test was 16.8%. In the LIVE-L3A test the highest heat flux at the polar angle 65.5° was about 12.5% higher than the mean heat flux, whereas in the LIVE-L3 test the highest heat flux was 8% higher than the mean value.
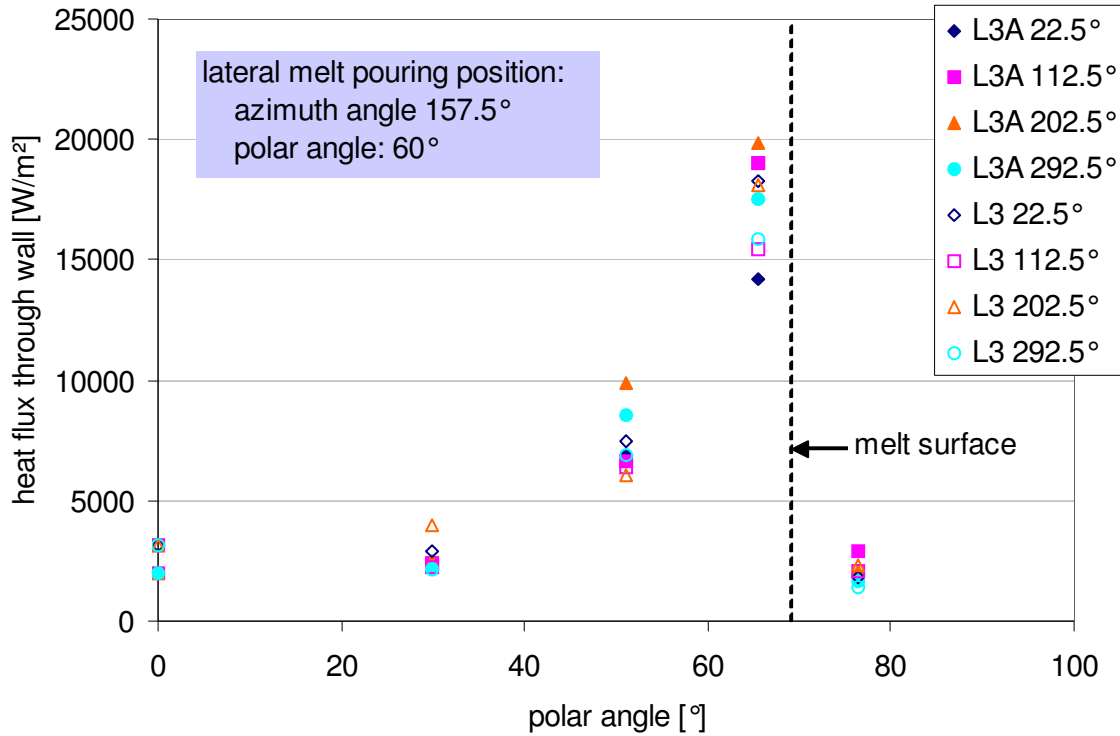
Figure 46: Comparison of the heat flux measured in the LIVE-L3 and LIVE-L3A tests.
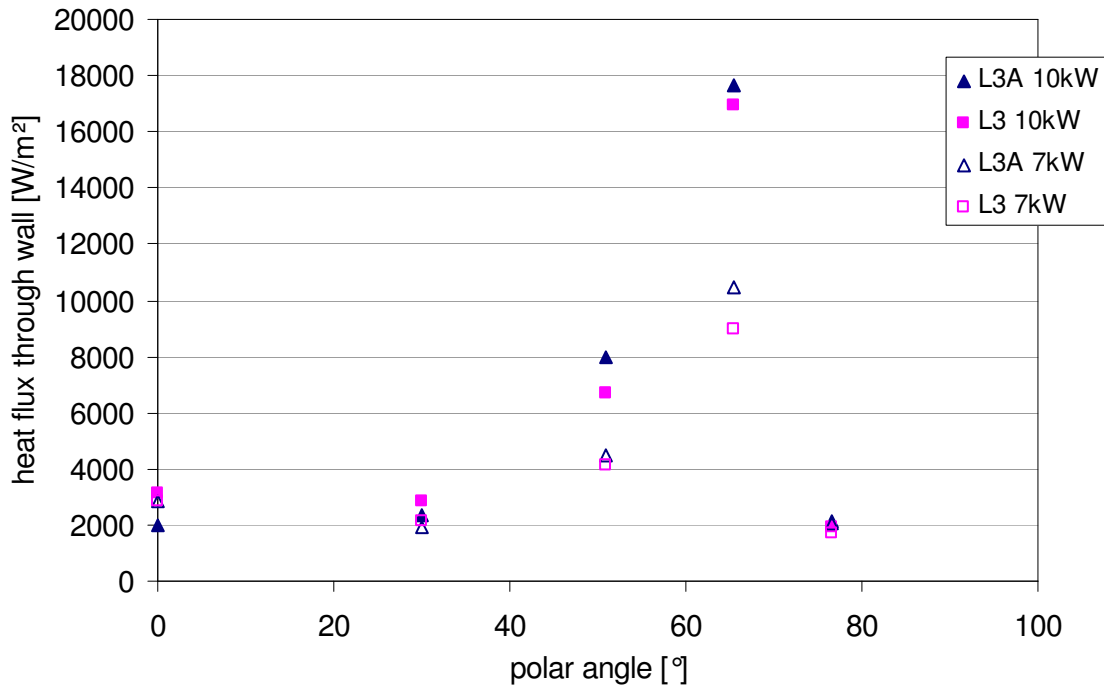
Figure 47: Comparison of the mean heat flux in the LIVE-L3 and LIVE-L3A tests.

Concerning the vertical heat flux distribution, Notable difference was observed in the upper part of the melt pool. The vertical distribution of the mean heat flux along the vessel polar angle is shown in the Figure 47. Higher fraction of heat was transferred through the upper part of the vessel wall during the LIVE-L3A test. At the lower part of the vessel wall this difference is negligible.

5.6 Heat flux splitting, wall inner temperature and cooling water temperature

5.6.1 Heat flux splitting

The heat flux splitting describes the relationship between the portion of the heat transported through the vessel wall below the melt surface (Q_{wall}) and the fraction of the heat released from the melt surface. In the LIVE experiments performed up to now only a small fraction of heat is transported upwards due to the insulated upper lid; the most of the heat is removed through the vessel wall to the cooling water.

In Table 21 the fractions of Q_{wall} during the steady-state of the LIVE-L3 and LIVE-L3A tests are presented. Due to the good insulation of the vessel upper lid 80% to 90% of the heat generated in the melt was removed through the vessel wall to the cooling water during the steady-state phases of the experiments. Increasing the heating power increases also the fraction of the heat transfer through the vessel wall. More heat was removed under the water cooling condition (LIVE-L3A) compared to the delayed water cooling condition (LIVE-L3).

Table 21: Heat flux splitting in the LIVE-L3 and LIVE-L3A tests.

	Heating power	Time s	Q_{wall} W	$Q_{heating}$ W	Q_{wall} / $Q_{heating}$ %
L3	10 kW	60001	8539	9833	86.8
	7 kW	94920	5477	6768	80.9
L3A	10 kW	50000	9125	10025	91
	7 kW	150000	6053	7000	86.5

5.6.2 Wall inner temperature

The wall inner temperature increased from ~23°C at the vessel bottom to ~90°C near the melt surface. Figure 48 shows the wall inner temperature during the steady-state of 10 kW and 7 kW phases. In both tests increasing the heating power resulted in significant increase of wall inner temperature up from the polar angle 51°.

The measured wall inner temperatures were generally higher in the LIVE-L3 than in the LIVE-L3A test. Taking into account that the melt pool temperatures in the LIVE-L3 test were lower than in the LIVE-L3A (Figure 41) and the crust in the LIVE-L3 test was thicker than in the LIVE-L3A, the crust thermal conductivity in the LIVE-L3 test must be lower than in the LIVE-L3A test.
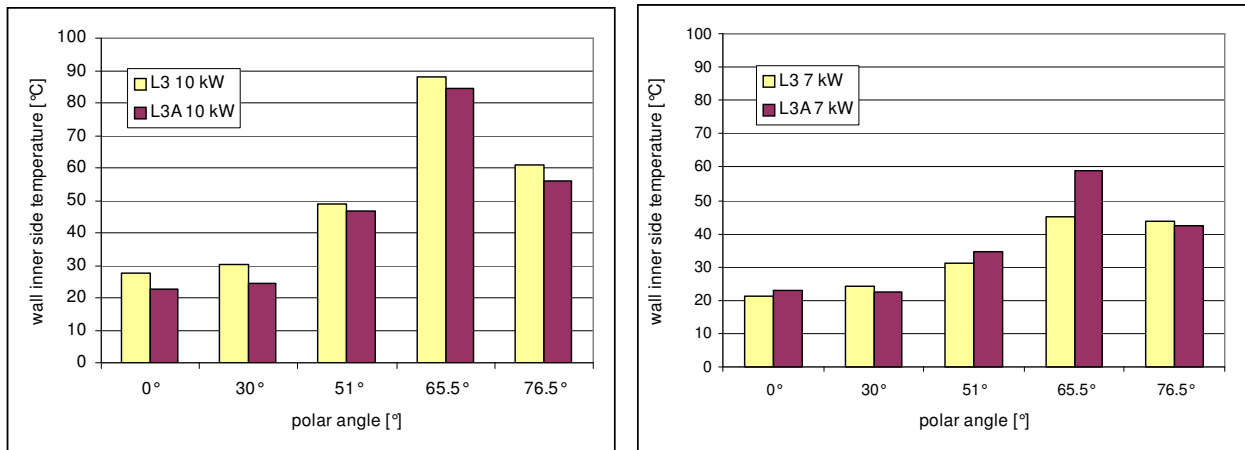
Figure 48: Wall inner temperatures in the LIVE-L3 and LIVE-L3A tests: left: 10 kW heating period, right: 7 kW heating period.

5.6.3 Cooling water temperature

The comparison of the cooling water temperature is helpful to get a better understanding of the differences observed in the two tests. In the Table 22 the water inlet and outlet temperatures are compared.

Table 22: Water temperature and water flow rate in the LIVE-L3 and LIVE-L3A tests.

	Heating period	Time, s	T_{inlet} °C	T_{outlet} °C	ΔT_{water} °C	water flow rate, mg/s
L3	10 kW	60001	15.9	59.0	40.0	46.6
	7 kW	94920	15.9	45.6	27.7	47
L3A	10 kW	50000	11.3	53.9	42.6	47.68
	7 kW	150000	11.4	40.0	28.6	47.2

Both the water inlet and outlet temperatures in the LIVE-L3 test were higher compared to the LIVE-L3A test. However the heatup of the cooling water was more pronounced in the LIVE-L3A test. Considering that the water flow rate in the LIVE-L3A test was slightly higher, more heat should be removed by the cooling water in the LIVE-L3A test. This is in a good agreement with the heat flux splitting described in the section 5.6.1. More heat was transported from the melt pool through the vessel walls to the cooling water in the LIVE-L3A test.

6 Conclusions

To complement the experimental data on melt pool behaviour in the vessel lower head KIT performs large-scale tests within the LIVE program. The LIVE experimental facility is designed to study the molten pool behaviour in the RPV lower head in order to provide the experimental data for the development and improvement of mechanistic models applied for the description of the late in-vessel phase of the core melt progression. The objective of the LIVE-L3A test was to study the influence of the melt relocation mode on the vessel thermal loads in the transient phase and on the long-term melt behaviour and crust formation and crust properties in the steady-state conditions.

The test performance of the LIVE-L3A test was similar to the previous LIVE-L3 test except the initial cooling conditions. In both tests the melt was poured near to the vessel wall. In the LIVE-L3 test the vessel was initially cooled by air and then by water; in the LIVE-L3A test the vessel was cooled by water already at the beginning of the experiment. Comparing the results of the LIVE-L3A and LIVE-L3 tests the following conclusions can be drawn.

Melt temperatures:

Ineffective air cooling at the beginning of the LIVE-L3 test resulted in the overall increase of melt pool temperature from the vessel bottom to the melt surface since the air flow could not remove the generated heat sufficiently. At the end of the air cooling period the maximum melt temperature reached 370°C, i.e. maximum allowed temperature of the simulant material. During the LIVE-L3A test the cooling water outside the vessel wall effectively cooled the hot melt. As a result the melt temperature in the middle and lower part of the pool decreased quickly to constant values, the melt temperature near the melt surface increased at first slightly, but decreased to a steady-state value after ~2000 s.

Behaviour of the initial crust layer:

In the LIVE-L3 test a crust layer was built up at the very beginning of the test, however it was completely molten due to the insufficient cooling by air and increase of the melt temperatures up from the polar angle of 30°. After the initiation of the water flooding, a new crust layer was formed. Therefore the influence of the asymmetric melt pouring position on the original crust layer was negligible in this test.

In the LIVE-L3A test a crust layer was formed at the beginning of the test and kept its form and properties during the whole test duration. The influence of the asymmetric melt pouring position on the crust formation process also persisted during the whole test period.

Influence of the melt pouring position on horizontal heat flux distribution:
Considerable asymmetry in horizontal heat flux distribution was observed in the upper part of the vessel where the contact area of the melt jet during the pouring was located. At the location of the melt jet, the heat flux through the vessel wall was noticeably higher than at the opposite location even in the steady-state conditions.

Crust growth velocity, crust thermal conductivity and crust thickness:
The different initial cooling conditions in the two tests resulted in the different crust growth rates, crust thermal conductivity and final crust thickness. The crust layer formed after the initiation of the water cooling in the LIVE-L3 test developed under poor cooling conditions, since the melt temperature was high and the vessel wall temperature was higher than the liquidus temperature of the melt. In the contrast with LIVE-L3, the crust layer in the LIVE-L3A test was formed under fast cooling condition, i.e. the melt contacted the cold vessel walls and solidified. The difference in the crust growth rates was quite noticeable during the first 3 to10 minutes of the crust growth period and almost 50% of the whole crust layer was influenced by the different growth rate. Fast cooling at the outside leads to a low thermal conductivity of the crust and a thinner crust layer during the thermal hydraulic steady-state. Fast cooling also leads to a shorter period of the crust growth.

Other differences in the results of the LIVE-L3 and LIVE-L3A were also observed but it is not quite clear up to now whether they can be attributed to the initial cooling conditions or to other minor differences in the test parameters. These are:
- steady-state melt temperature: the melt temperatures in the LIVE-L3A were generally ~3°C higher than in the LIVE-L3 test;
- vertical heat flux distribution: the focusing of heat flux near to the melt surface was more pronounced in the LIVE-L3A test. This corresponds also to the thinner crust layer at the upper part of the crust, given that the influence of the different crust thermal conductivity is compensated;
- heat flux splitting: higher amount of heat was removed through the vessel wall in the LIVE-L3A test.

The minor differences in test parameters were:
- heating power: the heating power in the LIVE-L3A was ~2% higher than in the LIVE-L3 test during the 10 kW heating period;
- cooling water temperature: the cooling water temperature in the LIVE-L3A was ~4.5°C lower than in the LIVE-L3 test.

7 References

[1]   O. Kymäläinen. H. Tuomisto. T.G. Theofanous. "In-vessel retention of corium at the Loviisa plant". Nuclear Engineering and Design 169 (1997) pp.109-130.

[2]   S. Abalin. I. Gnidoi. V. Semenov. V. Strizhov. A. Surenkov. "The Results and Analysis of the RASPLAV Salt Tests". Rasplav Seminar 2000. Munich. Germany. 14-15 November 2000.

[3]   T. G.Theofanous. S. Angelini. "Natural Convection for In-Vessel Retention at Prototypic Rayleigh Numbers". Nuclear Engineering and Design. 200 (2001). pp. 1-9.

[4]   V. Asmolov. et al.. "Challenges Left in the Area of In-Vessel Melt Retention". Nuclear Engineering and Design. 209 (2001). pp. 87-96.

[5]   B. Fluhrer. A. Miassoedov. T. Cron. J. Foit. X. Gaus-Liu. S. Schmidt-Stiefel. T. Wenz. I. Ivanov. D. Popov. "The LIVE-L1 and LIVE-L3 Experiments on Melt Behaviour in RPV Lower Head". FZKA-7419. September 2008.

[6]   A. Miassoedov. et al.. "Results of the LIVE-L1 Experiment on Melt Behaviour in RPV Lower Head Performed within the LACOMERA project at the Forschungszentrum Karlsruhe". 2007. Proc. 15th International Conference on Nuclear Engineering (ICONE15). Nagoya. Japan. April 22-26. 2007. Paper 10227.

[7]   B. Fluhrer. et al.. "The Experimental Programme LIVE to investigate In-Vessel Core Melt Behaviour in the Late Phase". Jahrestagung Kerntechnik 2005. Nürnberg. INFORUM GmbH. 2005. pp. 198-201.

[8]   Deutsche Risikostudie Kernkraftwerke. Phase B-: eine Untersuchung / Ges. für Reaktorsicherheit. Im Auftr. d. Bundesministers für Forschung u. Technologie. - Köln: Verl. TÜV Rheinland. 1990. ISBN 3-88585-809-6.

[9]   B.R. Sehgal. Z.L. Yang. "Ex-vessel Core Melt Stabilization Research; On the Experiments with Simulant Materials at KTH". SAM-ECOSTAR-P11/001. KTH. Stockholm. Sweden. January 2001.

[10]   E.M. Levin. C.R. Robbins. H.F. McMurdie. 1985. "Phase Diagrams For Ceramists Vol. 1: Oxides and Salts". American Ceramic Society. ISBN-10: 0916094049.

[11]   H.M. Goodwin. and R.D. Mailey. "On the Density. Electrical Conductivity and Viscosity of Fused Salts and Their Mixtures". The Physical Review - American Physical Society. January. 1980. pp. 40.

[12]   F.P. Incropera. D.P. Dewitt. "Introduction to heat transfer". ISBN0-471-38649-9. pp. 820.

[13]   Flemmings, "Solidification Processing", Materials Science and Engineering Series, ISBN 0-07-021283-x, pp.59-66.

[14]   R.W. Berg et al., 2004, "The NaNO3/KNO3 system: the position of the solidus and sub-solidus", Dalton Trans., pp. 2224-2229.

[15]   A. S. Dworkin, , R. B. Escue, , Van Artsdalen, E., 1960, "Self-diffusion in molten nitrates", J. Phys. Chem. 64 (7), pp. 872-876.

[16]   G. J. Janz,; C. B. Allen; N. P. Bansal; et al., 1979, "Physical Properties Data Compilations Relevant to Energy Storage- II. Molten Salts: Data on Single and multi-Component Salt Systems "NSRDS, U.S. Department of Commerce, pp. 4

[17]   R.P. Tye, "Thermal conductivity", Ed. by R.P. Tye, Vol. 1, London: Academic Pr., 1969, ISBN 12-705401-4, pp.17.

[18]   G.J. Janz. and C.B. Allen. "Physical Properties Data Compilations. Relevant to Energy Storage. II. Molten Salts: Data on Single and Multi-Component Salt Systems". U.S. Department of Commerce. National Bureau of Standards. NSRDS-NBS 61. Part II. April 1979. pp161+pp148.

[19]   P.R. Sahm, I. Egry, "Schmelze, Erstarrung, Grenzflächen", ISBN 3-528-06979-1. pp 208.

Annex A   Data Acquisition and Instrumentation

Annex A.1   LIVE-L3A channel assignment

Table A- 1 lists all signals that were registered on the PC data acquisition system for the experiment LIVE-L3A. All signal cables are attached to a control cabinet, which is positioned near the LIVE test vessel. The temperature signals are all single-ended signals. The reference junctions of thermocouples are traditionally maintained at 0 °C. This is assumed in thermocouple calibration tables. In the LIVE experiments the reference junction is situated in the control cabinet and has ambient temperature. To overcome this error of a non-zero thermocouple reference junction, the temperature of the reference point is measured by three PT-100 sensors (named RT) that are attached at the connector blocks of the thermocouples. This temperature is then used to correct the temperature measured by the thermocouples.

Table A- 1: LIVE-L3A channel assignment for PC data acquisition system

Nr.	Designation	Category	Sensor	Position Angle φ	Radius [mm]	Depth [mm]	Channel Number	Remarks
1	ST1	Spout temperature	NiCr/Ni	-	-	-	1	ST = Spout Temperature
2	MT1	Melt temperature	NiCr/Ni	0	74	450	2	MT = Melt Temperature
3	MT2	Melt temperature	NiCr/Ni	90	74	450	3	
4	MT3	Melt temperature	NiCr/Ni	180	74	450	4	Reference point:
5	MT4	Melt temperature	NiCr/Ni	270	74	450	5	Angle 0 = Instrumentation axis
6	MT5	Melt temperature	NiCr/Ni	0	174	450	6	Radius 0 = Middle of the tet vessel
7	MT6	Melt temperature	NiCr/Ni	90	174	450	7	Depth 0 = Flange upper edge
8	MT7	Melt temperature	NiCr/Ni	180	174	450	8	
9	MT8	Melt temperature	NiCr/Ni	270	174	450	9	
10	MT9	Melt temperature	NiCr/Ni	0	74	350	10	
11	MT0	Melt temperature	NiCr/Ni	90	74	350	11	
12	MT11	Melt temperature	NiCr/Ni	180	74	350	12	
13	MT12	Melt temperature	NiCr/Ni	270	74	350	13	
14	MT13	Melt temperature	NiCr/Ni	0	174	350	14	
15	MT14	Melt temperature	NiCr/Ni	90	174	350	15	
16	MT15	Melt temperature	NiCr/Ni	180	174	350	16	
17	MT16	Melt temperature	NiCr/Ni	270	174	350	17	
18	MT17	Melt temperature	NiCr/Ni	0	274	350	18	
19	MT18	Melt temperature	NiCr/Ni	90	274	350	19	
20	MT19	Melt temperature	NiCr/Ni	180	274	350	20	
21	MT20	Melt temperature	NiCr/Ni	270	274	350	21	
22	MT21	Melt temperature	NiCr/Ni	0	74	250	22	
23	MT22	Melt temperature	NiCr/Ni	90	74	250	23	
24	MT23	Melt temperature	NiCr/Ni	180	74	250	24	
25	MT24	Melt temperature	NiCr/Ni	270	74	250	25	

26	MT25	Melt temperature	NiCr/Ni	0	174	250	26	
27	MT26	Melt temperature	NiCr/Ni	90	174	250	27	
28	MT27	Melt temperature	NiCr/Ni	180	174	250	28	
29	MT28	Melt temperature	NiCr/Ni	270	174	250	29	
30	MT39	Melt temperature	NiCr/Ni	0	274	250	30	
31	MT30	Melt temperature	NiCr/Ni	90	274	250	31	
32	MT31	Melt temperature	NiCr/Ni	180	274	250	32	
33	MT32	Melt temperature	NiCr/Ni	270	274	250	33	
34	MT33	Melt temperature	NiCr/Ni	0	374	250	34	
35	MT34	Melt temperature	NiCr/Ni	90	374	250	35	
36	MT35	Melt temperature	NiCr/Ni	180	374	250	36	
37	MT36	Melt temperature	NiCr/Ni	270	374	250	37	
38	MT37	Temperature above melt	NiCr/Ni	0	60	50	38	
39	OT1	Outer wall temperature	NiCr/Ni	292.5	36.35	518	191	OT = Temperature of the vessel outer surface
40	OT2	Outer wall temperature	NiCr/Ni	22.5	260	451	192	
41	OT3	Outer wall temperature	NiCr/Ni	112.5	260	451	193	
42	OT4	Outer wall temperature	NiCr/Ni	202.5	260	451	194	Reference point:
43	OT5	Outer wall temperature	NiCr/Ni	292.5	260	451	195	Angle 0 = Instrumentation axis
44	OT6	Outer wall temperature	NiCr/Ni	22.5	404	327	196	Radius 0 = Middle of the test vessel
45	OT7	Outer wall temperature	NiCr/Ni	112.5	404	327	197	Depth 0 = Flange upper edge
46	OT8	Outer wall temperature	NiCr/Ni	202.5	404	327	198	
47	OT9	Outer wall temperature	NiCr/Ni	292.5	404	327	199	
48	OT10	Outer wall temperature	NiCr/Ni	22.5	474	216	200	
49	OT11	Outer wall temperature	NiCr/Ni	112.5	474	216	201	
50	OT12	Outer wall temperature	NiCr/Ni	202.5	474	216	202	
51	OT13	Outer wall temperature	NiCr/Ni	292.5	474	216	203	
52	OT14	Outer wall temperature	NiCr/Ni	22.5	506	121	204	
53	OT15	Outer wall temperature	NiCr/Ni	112.5	506	121	205	
54	OT16	Outer wall temperature	NiCr/Ni	202.5	506	121	206	
55	OT17	Outer wall temperature	NiCr/Ni	292.5	506	121	207	

No.	Label	Description	Type				No.
56	IT1	Inner wall temperature	NiCr/Ni	292.5	35	520	49
57	IT2	Inner wall temperature	NiCr/Ni	22.5	249	455	50
58	IT3	Inner wall temperature	NiCr/Ni	112.5	249	455	51
59	IT4	Inner wall temperature	NiCr/Ni	202.5	249	455	52
60	IT5	Inner wall temperature	NiCr/Ni	292.5	249	455	53
61	IT6	Inner wall temperature	NiCr/Ni	22.5	387	337	54
62	IT7	Inner wall temperature	NiCr/Ni	112.5	387	337	55
63	IT8	Inner wall temperature	NiCr/Ni	202.5	387	337	56
64	IT9	Inner wall temperature	NiCr/Ni	292.5	387	337	57
65	IT10	Inner wall temperature	NiCr/Ni	22.5	453	230	58
66	IT11	Inner wall temperature	NiCr/Ni	112.5	453	230	59
67	IT12	Inner wall temperature	NiCr/Ni	202.5	453	230	60
68	IT13	Inner wall temperature	NiCr/Ni	292.5	453	230	61
69	IT14	Inner wall temperature	NiCr/Ni	22.5	484	140	62
70	IT15	Inner wall temperature	NiCr/Ni	112.5	484	140	63
71	IT16	Inner wall temperature	NiCr/Ni	202.5	484	149	64
72	IT17	Inner wall temperature	NiCr/Ni	292.5	484	140	65
73	OOT1	Outer temp. cooling tank	NiCr/Ni	300	38	730	46
74	OOT2	Outer temp. cooling tank	NiCr/Ni	300	428	587	47
75	OOT3	Outer temp. cooling tank	NiCr/Ni	300	670	250	48
76	PT11	Temperature of plug 1	NiCr/Ni	0	0	520	68
77	PT12	Temperature of plug 1	NiCr/Ni	0	0	520	69
78	PT13	Temperature of plug 1	NiCr/Ni	0	0	520	70
79	PT14	Temperature of plug 1	NiCr/Ni	0	0	520	71
80	PT15	Temperature of plug 1	NiCr/Ni	0	0	520	72
81	PT21	Temperature of plug 2	NiCr/Ni	67.5	248.18	454	146
82	PT22	Temperature of plug 2	NiCr/Ni	67.5	248.18	454	147
83	PT23	Temperature of plug 2	NiCr/Ni	67.5	248.18	454	148
84	PT24	Temperature of plug 2	NiCr/Ni	67.5	248.18	454	149
85	PT25	Temperature of plug 2	NiCr/Ni	67.5	248.18	454	150

IT = Temperature of the vessel inner surface

OOT = Temperature of the cooling tank outer surface

PT = Plug temperature

Position refers to the upper edge of the instrumentation plug

Reference point:
Angle 0 = Instrumentation axis
Radius 0 = Middle of the test vessel
Depth 0 = Flange upper edge

								Designation of the "b" number of PT"ab" 1 = 0 mm 2 = 5 mm 3 = 10 mm 4 = 15 mm 5 = 20 mm length of the thermocouple from the inner vessel wall into the melt
86	PT31	Temperature of plug 3	NiCr/Ni	157.5	248.18	454	122	
87	PT32	Temperature of plug 3	NiCr/Ni	157.5	248.18	454	123	
88	PT33	Temperature of plug 3	NiCr/Ni	157.5	248.18	454	124	
89	PT34	Temperature of plug 3	NiCr/Ni	157.5	248.18	454	125	
90	PT35	Temperature of plug 3	NiCr/Ni	157.5	248.18	454	126	
91	PT41	Temperature of plug 4	NiCr/Ni	247.5	248.18	454	98	
92	PT42	Temperature of plug 4	NiCr/Ni	247.5	248.18	454	99	
93	PT43	Temperature of plug 4	NiCr/Ni	247.5	248.18	454	100	
94	PT44	Temperature of plug 4	NiCr/Ni	247.5	248.18	454	101	
95	PT45	Temperature of plug 4	NiCr/Ni	247.5	248.18	454	102	
96	PT51	Temperature of plug 5	NiCr/Ni	337.5	248.18	454	74	
97	PT52	Temperature of plug 5	NiCr/Ni	337.5	248.18	454	75	
98	PT53	Temperature of plug 5	NiCr/Ni	337.5	248.18	454	76	
99	PT54	Temperature of plug 5	NiCr/Ni	337.5	248.18	454	77	
100	PT55	Temperature of plug 5	NiCr/Ni	337.5	248.18	454	78	
101	PT61	Temperature of plug 6	NiCr/Ni	67.5	385.75	337	152	
102	PT62	Temperature of plug 6	NiCr/Ni	67.5	385.75	337	153	
103	PT63	Temperature of plug 6	NiCr/Ni	67.5	385.75	337	154	
104	PT64	Temperature of plug 6	NiCr/Ni	67.5	385.75	337	155	
105	PT65	Temperature of plug 6	NiCr/Ni	67.5	385.75	337	156	
106	PT71	Temperature of plug 7	NiCr/Ni	157.5	385.75	337	128	
107	PT72	Temperature of plug 7	NiCr/Ni	157.5	385.75	337	129	
108	PT73	Temperature of plug 7	NiCr/Ni	157.5	385.75	337	130	
109	PT74	Temperature of plug 7	NiCr/Ni	157.5	385.75	337	131	
110	PT75	Temperature of plug 7	NiCr/Ni	157.5	385.75	337	132	
111	PT81	Temperature of plug 8	NiCr/Ni	247.5	385.75	337	104	
112	PT82	Temperature of plug 8	NiCr/Ni	247.5	385.75	337	105	
113	PT83	Temperature of plug 8	NiCr/Ni	247.5	385.75	337	106	
114	PT84	Temperature of plug 8	NiCr/Ni	247.5	385.75	337	107	
115	PT85	Temperature of plug 8	NiCr/Ni	247.5	385.75	337	108	

116	PT91	Temperature of plug 9	NiCr/Ni	337.5	385.75	337	80
117	PT91	Temperature of plug 9	NiCr/Ni	337.5	385.75	337	81
118	PT93	Temperature of plug 9	NiCr/Ni	337.5	385.75	337	82
119	PT94	Temperature of plug 9	NiCr/Ni	337.5	385.75	337	83
120	PT95	Temperature of plug 9	NiCr/Ni	337.5	385.75	337	84
121	PT101	Temperature of plug 10	NiCr/Ni	67.5	451.69	230	158
122	PT102	Temperature of plug 10	NiCr/Ni	67.5	451.69	230	159
123	PT103	Temperature of plug 10	NiCr/Ni	67.5	451.69	230	160
124	PT104	Temperature of plug 10	NiCr/Ni	67.5	451.69	230	161
125	PT105	Temperature of plug 10	NiCr/Ni	67.5	451.69	230	162
126	PT111	Temperature of plug 11	NiCr/Ni	157.5	451.69	230	134
127	PT112	Temperature of plug 11	NiCr/Ni	157.5	451.69	230	135
128	PT113	Temperature of plug 11	NiCr/Ni	157.5	451.69	230	136
129	PT114	Temperature of plug 11	NiCr/Ni	157.5	451.69	230	137
130	PT115	Temperature of plug 11	NiCr/Ni	157.5	451.69	230	138
131	PT121	Temperature of plug 12	NiCr/Ni	247.5	451.69	230	110
132	PT122	Temperature of plug 12	NiCr/Ni	247.5	451.69	230	111
133	PT123	Temperature of plug 12	NiCr/Ni	247.5	451.69	230	112
134	PT124	Temperature of plug 12	NiCr/Ni	247.5	451.69	230	113
135	PT125	Temperature of plug 12	NiCr/Ni	247.5	451.69	230	114
136	PT131	Temperature of plug 13	NiCr/Ni	337.5	451.69	230	86
137	PT132	Temperature of plug 13	NiCr/Ni	337.5	451.69	230	87
138	PT133	Temperature of plug 13	NiCr/Ni	337.5	451.69	230	88
139	PT134	Temperature of plug 13	NiCr/Ni	337.5	451.69	230	89
140	PT135	Temperature of plug 13	NiCr/Ni	337.5	451.69	230	90
141	PT141	Temperature of plug 14	NiCr/Ni	67.5	482.66	140	164
142	PT142	Temperature of plug 14	NiCr/Ni	67.5	482.66	140	165
143	PT143	Temperature of plug 14	NiCr/Ni	67.5	482.66	140	166
144	PT144	Temperature of plug 14	NiCr/Ni	67.5	482.66	140	167
145	PT145	Temperature of plug 14	NiCr/Ni	67.5	482.66	140	168

146	PT151	Temperature of plug 15	NiCr/Ni	157.5	482.66	140	140
147	PT152	Temperature of plug 15	NiCr/Ni	157.5	482.66	140	141
148	PT153	Temperature of plug 15	NiCr/Ni	157.5	482.66	140	142
149	PT154	Temperature of plug 15	NiCr/Ni	157.5	482.66	140	143
150	PT155	Temperature of plug 15	NiCr/Ni	157.5	482.66	140	144
151	PT161	Temperature of plug 16	NiCr/Ni	247.5	482.66	140	116
152	PT162	Temperature of plug 16	NiCr/Ni	247.5	482.66	140	117
153	PT163	Temperature of plug 16	NiCr/Ni	247.5	482.66	140	118
154	PT164	Temperature of plug 16	NiCr/Ni	247.5	482.66	140	119
155	PT165	Temperature of plug 16	NiCr/Ni	247.5	482.66	140	120
156	PT171	Temperature of plug 17	NiCr/Ni	337.5	482.66	140	92
157	PT172	Temperature of plug 17	NiCr/Ni	337.5	482.66	140	93
158	PT173	Temperature of plug 17	NiCr/Ni	337.5	482.66	140	94
159	PT174	Temperature of plug 17	NiCr/Ni	337.5	482.66	140	95
160	PT175	Temperature of plug 17	NiCr/Ni	337.5	482.66	140	96
161	HFT1	Heat flux sensor temperature	NiCr/Ni	0	0	520	67
162	HFT2	Heat flux sensor temperature	NiCr/Ni	67.5	248.18	454	145
163	HFT3	Heat flux sensor temperature	NiCr/Ni	157.5	248.18	454	121
164	HFT4	Heat flux sensor temperature	NiCr/Ni	247.5	248.18	454	97
165	HFT5	Heat flux sensor temperature	NiCr/Ni	337.5	248.18	454	73
166	HFT6	Heat flux sensor temperature	NiCr/Ni	67.5	385.75	337	151
167	HFT7	Heat flux sensor temperature	NiCr/Ni	157.5	385.75	337	127
168	HFT8	Heat flux sensor temperature	NiCr/Ni	247.5	385.75	337	103
169	HFT9	Heat flux sensor temperature	NiCr/Ni	337.5	385.75	337	79
170	HFT10	Heat flux sensor temperature	NiCr/Ni	67.5	451.69	230	157
171	HFT11	Heat flux sensor temperature	NiCr/Ni	157.5	451.69	230	133
172	HFT12	Heat flux sensor temperature	NiCr/Ni	247.5	451.69	230	109
173	HFT13	Heat flux sensor temperature	NiCr/Ni	337.5	451.69	230	85
174	HFT14	Heat flux sensor temperature	NiCr/Ni	67.5	482.66	140	163
175	HFT15	Heat flux sensor temperature	NiCr/Ni	157.5	482.66	140	139

Position refers to the upper edge of the instrumentation plug

Reference point:

Angle 0 = Instrumentation axis

Radius 0 = Middle of the test vessel

Depth 0 = Flange upper edge

176	HFT16	Heat flux sensor temperature	NiCr/Ni	247.5	482.66	140	115
177	HFT17	Heat flux sensor temperature	NiCr/Ni	337.5	482.66	140	91
178	HF1	Heat flux	HFS	0	0	520	169
179	HF2	Heat flux	HFS	67.5	248.18	454	170
180	HF3	Heat flux	HFS	157.5	248.18	454	171
181	HF4	Heat flux	HFS	247.5	248.18	454	172
182	HF5	Heat flux	HFS	337.5	248.18	454	173
183	HF6	Heat flux	HFS	67.5	385.75	337	174
184	HF7	Heat flux	HFS	157.5	385.75	337	175
185	HF8	Heat flux	HFS	247.5	385.75	337	176
186	HF9	Heat flux	HFS	337.5	385.75	337	177
187	HF10	Heat flux	HFS	67.5	451.69	230	178
188	HF11	Heat flux	HFS	157.5	451.69	230	179
189	HF12	Heat flux	HFS	247.5	451.69	230	180
190	HF13	Heat flux	HFS	337.5	451.69	230	181
191	HF14	Heat flux	HFS	67.5	482.66	140	182
192	HF15	Heat flux	HFS	157.5	482.66	140	183
193	HF16	Heat flux	HFS	247.5	482.66	140	184
194	HF17	Heat flux	HFS	337.5	482.66	140	185
195	CT41	TC-Tree 4	NiCr/Ni	25	299	420.4	208
196	CT42	TC-Tree 4	NiCr/Ni	25	299	420.4	209
197	CT43	TC-Tree 4	NiCr/Ni	25	299	420.4	210
198	CT44	TC-Tree 4	NiCr/Ni	25	299	420.4	211
199	CT45	TC-Tree 4	NiCr/Ni	25	299	420.4	212
200	CT46	TC-Tree 4	NiCr/Ni	25	299	420.4	213
201	CT47	TC-Tree 4	NiCr/Ni	25	299	420.4	214
201	CT21	TC-Tree 2	NiCr/Ni	35	398	320.4	215
203	CT22	TC-Tree 2	NiCr/Ni	35	398	320.4	216
204	CT23	TC-Tree 2	NiCr/Ni	35	398	320.4	217
205	CT24	TC-Tree 2	NiCr/Ni	35	398	320.4	218

CT = Crust Temperature

Position refers to the mounting position of the TC-Tree

Reference point:

Angle 0 = Instrumentation axis

Radius 0 = Middle of the test vessel

Designation of the "b" number of CT"ab" different for a = 1 and a = (2.3)

206	CT25	TC-Tree 2	NiCr/Ni	35	398	320.4	219	1 = 0 mm (0 mm)
207	CT26	TC-Tree 2	NiCr/Ni	35	398	320.4	220	2 = 9 mm (3 mm)
208	CT27	TC-Tree 2	NiCr/Ni	35	398	320.4	221	3 = 18 mm (6 mm)
209	CT31	TC-Tree 3	NiCr/Ni	35	456	220.4	222	4 = 27 mm (9 mm)
210	CT32	TC-Tree 3	NiCr/Ni	35	456	220.4	223	5 = 36 mm (12 mm)
211	CT33	TC-Tree 3	NiCr/Ni	35	456	220.4	224	6 = 45 mm (15 mm)
212	CT34	TC-Tree 3	NiCr/Ni	35	456	220.4	225	7 = 54 mm (18 mm)
213	CT35	TC-Tree 3	NiCr/Ni	35	456	220.4	226	length of the thermocouple from
214	CT36	TC-Tree 3	NiCr/Ni	35	456	220.4	227	inner wall into the melt
215	CT37	TC-Tree 3	NiCr/Ni	35	456	220.4	228	
216	LT1	Temp. measuring rod	NiCr/Ni	340	365	variable	41	Thermocouples of the crust
217	LT2	Temp. measuring rod	NiCr/Ni	340	365	variable	42	detection system. which is movable
218	LT3	Temp. measuring rod	NiCr/Ni	340	365	variable	43	in vertical direction
219	LT4	Temp. measuring rod	NiCr/Ni	340	365	variable	44	
220	LT5	Temp. measuring rod	NiCr/Ni	340	365	variable	45	
221	RT1	Temp. Control Cabinet	Pt-100					RT = Resistance Thermometer
222	RT2	Temp. Control Cabinet	Pt-100					
223	RT3	Temp. Control Cabinet	Pt-100					
224	AT1	Temp. cool. water outflow	NiCr/Ni	inside bow of overflow rod			230	
225	AT2	Temp. cool. water outflow	NiCr/Ni	inside bow of overflow rod			229	redundancy
226	ZT1	Temp. cooling water inflow	NiCr/Ni	behind flowmeter			231	
227	KT1	Temp. condensate outflow	NiCr/Ni	behind condensator			232	
228	W1	Weight of test vessel	W. cells	-			233	
229	DF1	Flow rate cooling water	Krohne	inside cooling water inlet			234	flowmeter 0-2 l/s
230	DF2	Flow rate cooling water	Kobold	inside cooling water inlet			235	flowmeter 0-416.7 ml/s (25 l/min)

Annex A.2   Drawings of the instrumentation of the LIVE test vessel
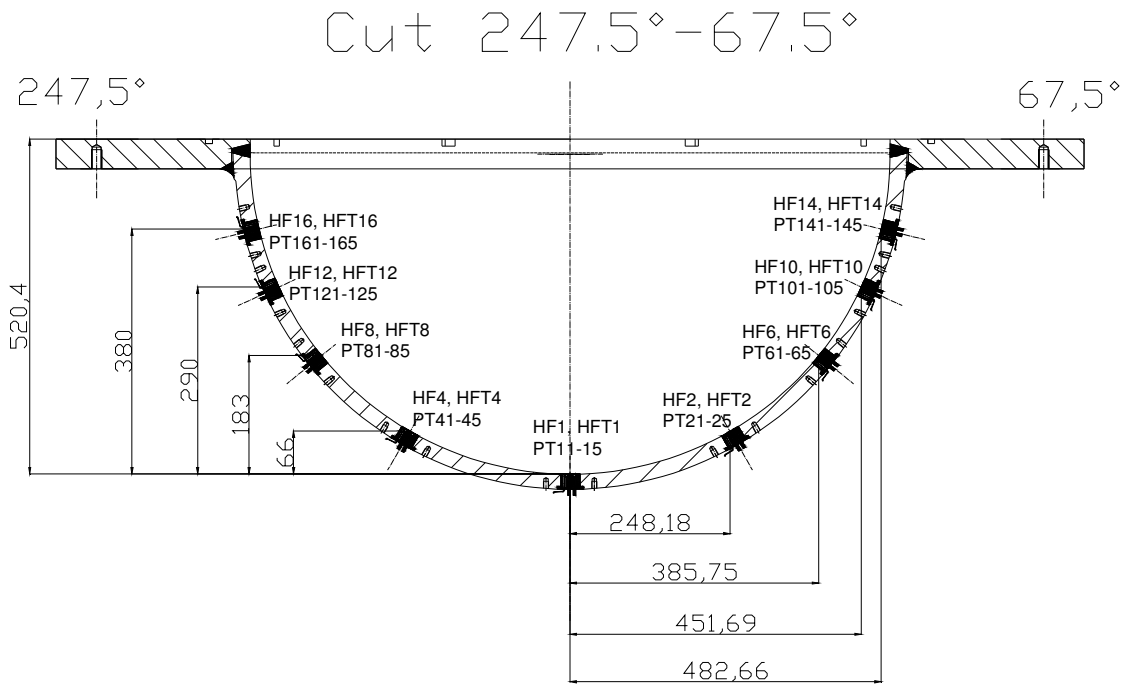
Figure A-1: Positions of the instrumented plugs along the meridians at 67.5° and 247.5°.
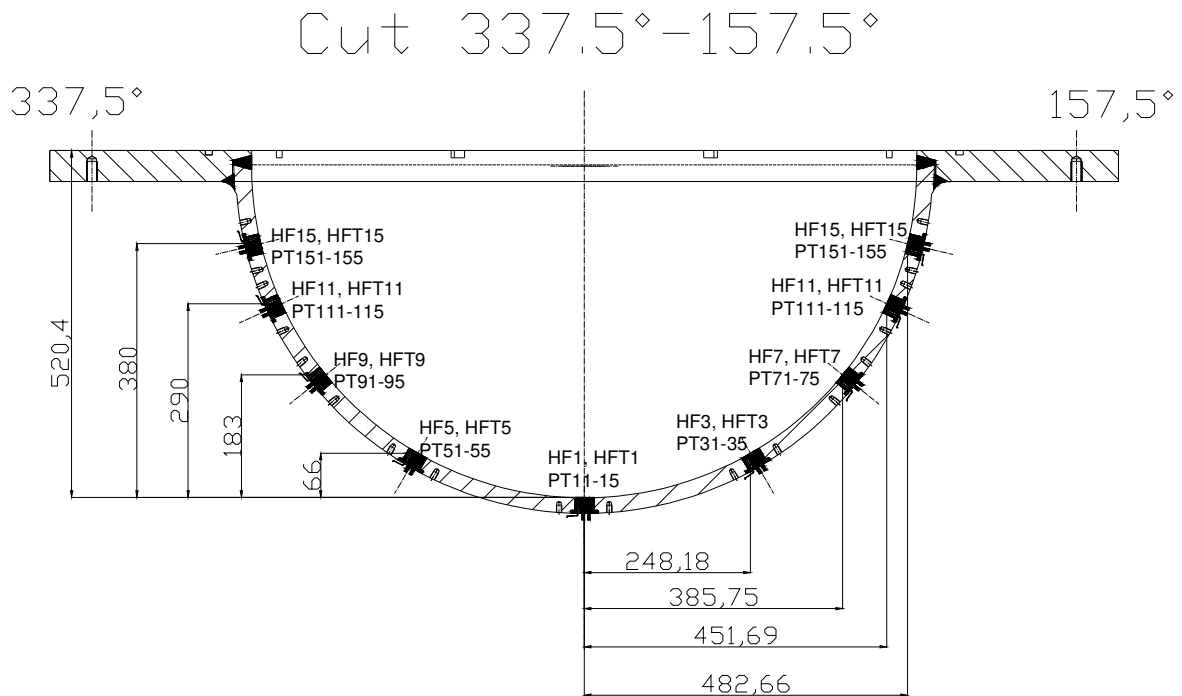
Figure A-2: Positions of the instrumented plugs along the meridians at 157.5° and 337.5°.
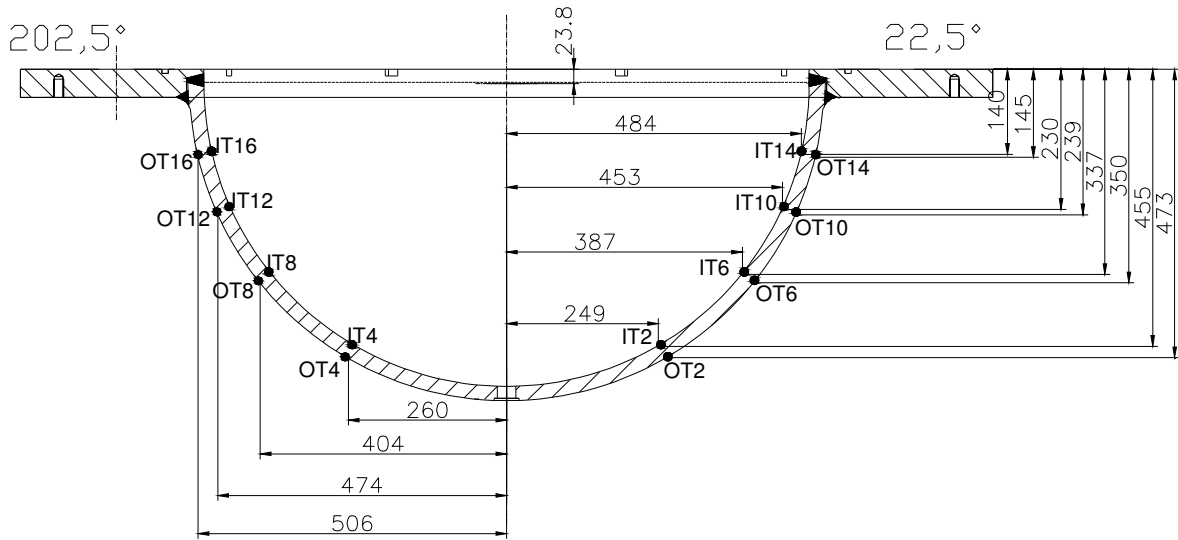
Figure A-3: Positions of the IT and OT thermocouples along the meridians at 22.5° and 202.5°.
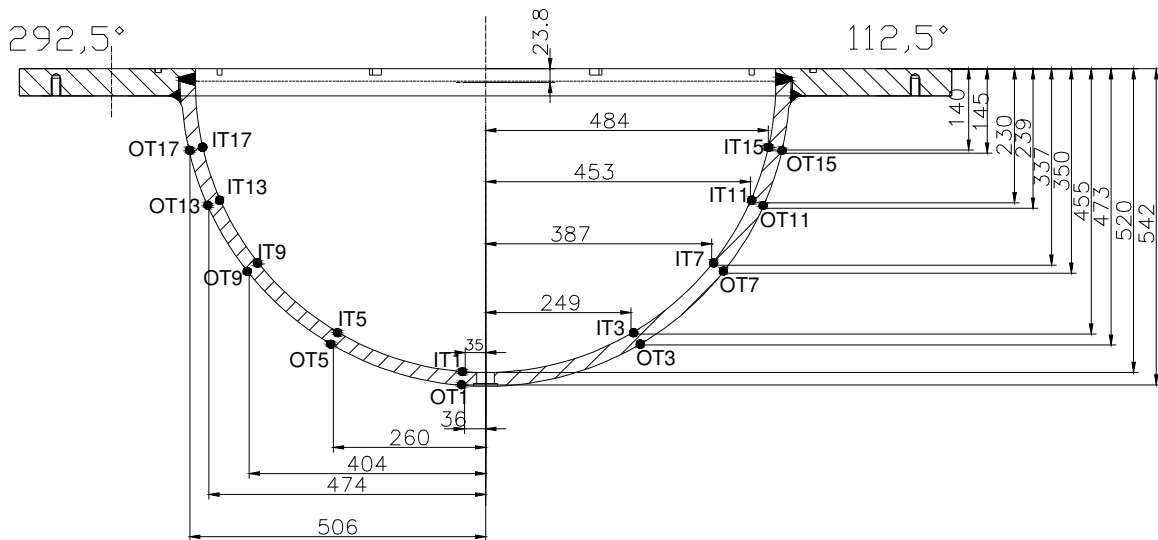
Figure A-4: Positions of the IT and OT thermocouples along the meridians at 112.5° and 292.5°.

Cut 0° - 180°
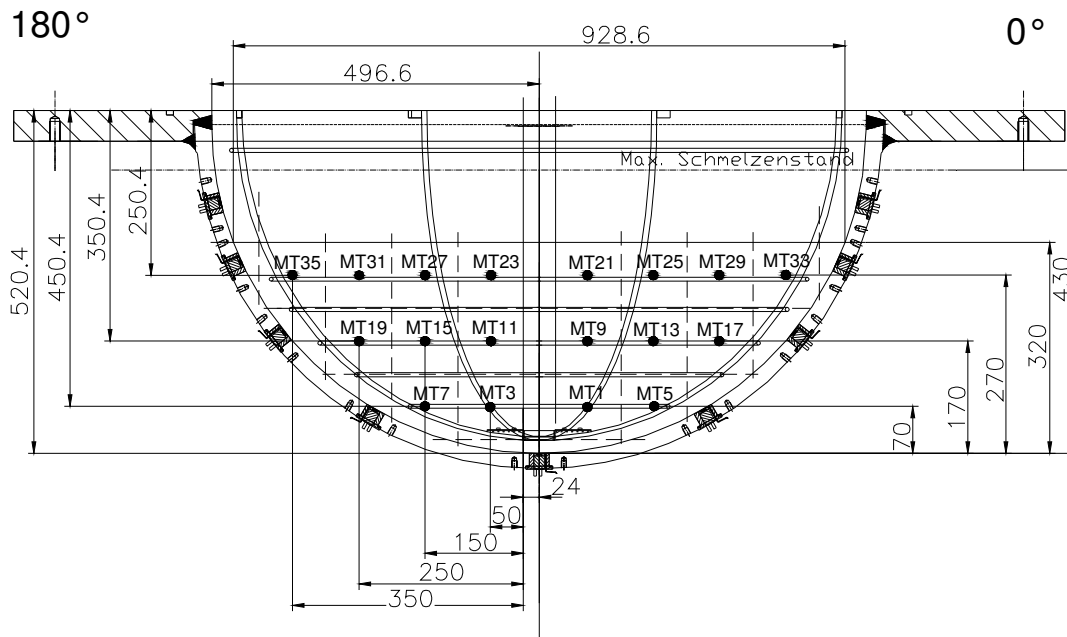
Figure A-5: Positions of the MT thermocouples in the section 0° - 180°

Cut 90° - 270°
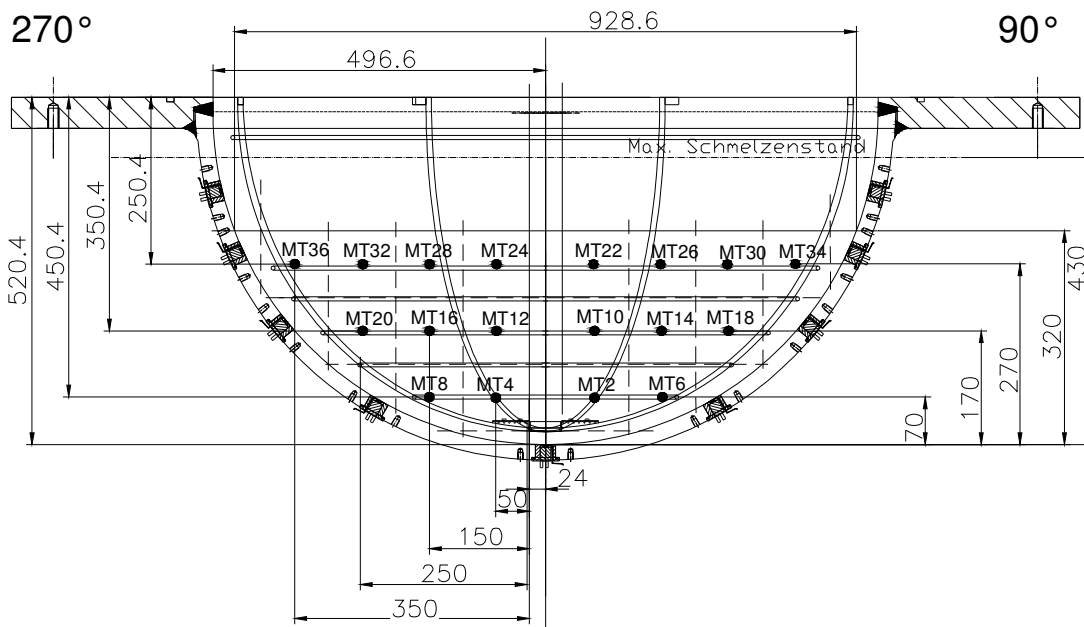
Figure A-6: Positions of the MT thermocouples in the section 90° - 270°
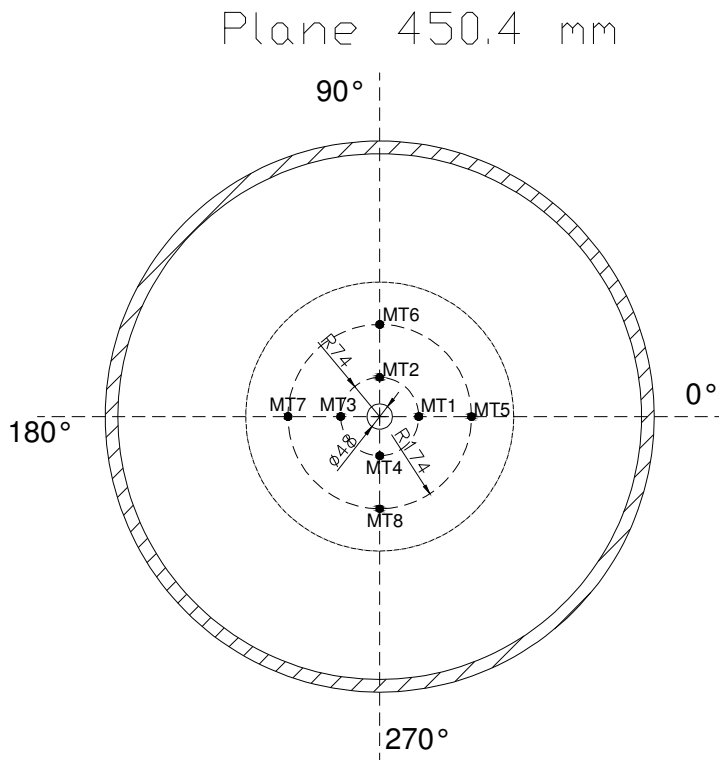
Figure A-7: Orientation of the MT thermocouples at the plane 450.4 mm. Reference point is the upper edge of the LIVE test vessel.
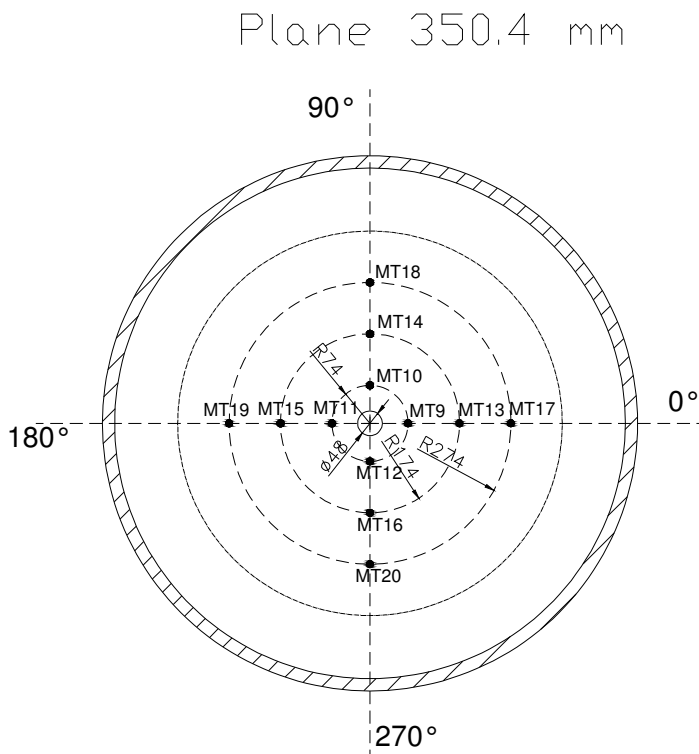
Figure A-8: Orientation of the MT thermocouples at the plane 350.4 mm. Reference point is the upper edge of the LIVE test vessel.
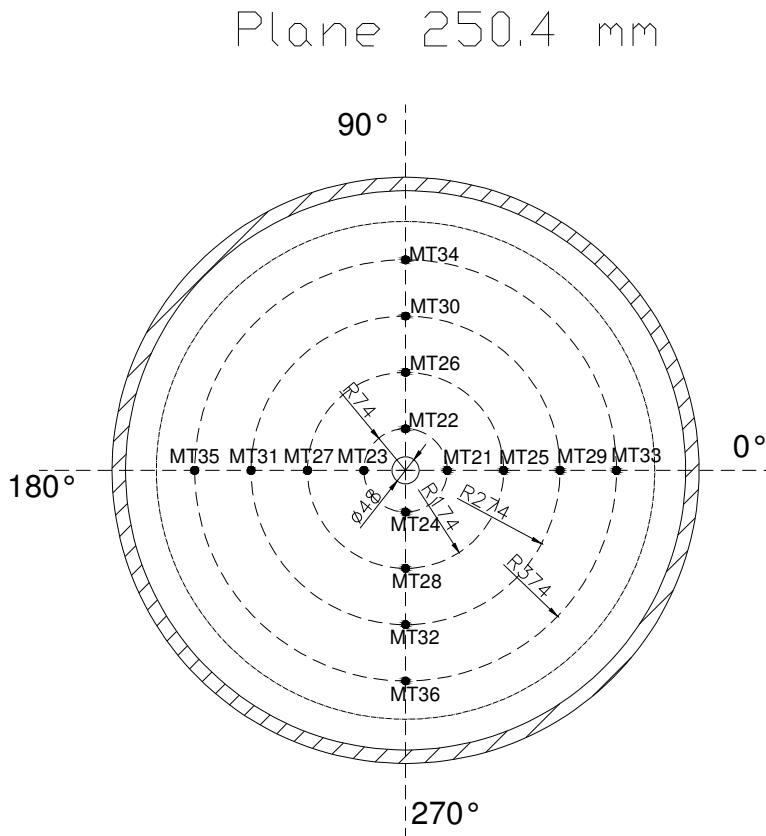
Plane 250.4 mm

Figure A-9: Orientation of the MT thermocouples at the plane 250.4 mm. Reference point is the upper edge of the LIVE test vessel.

Cut 215°-35°
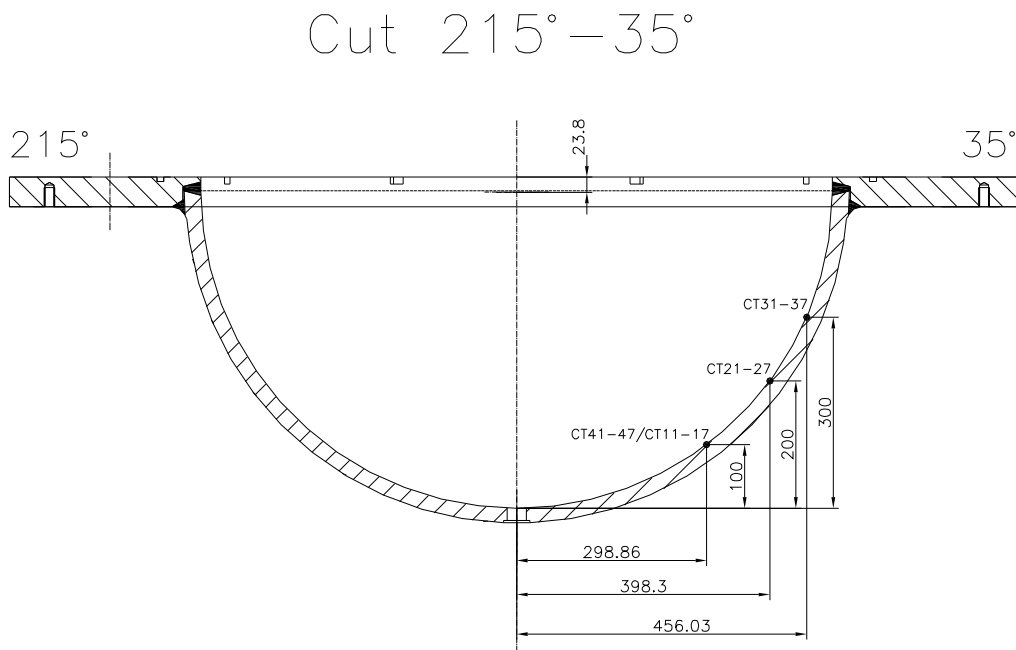
Figure A-10: Positions of the thermocouple trees along the meridians at 25° and 35°.
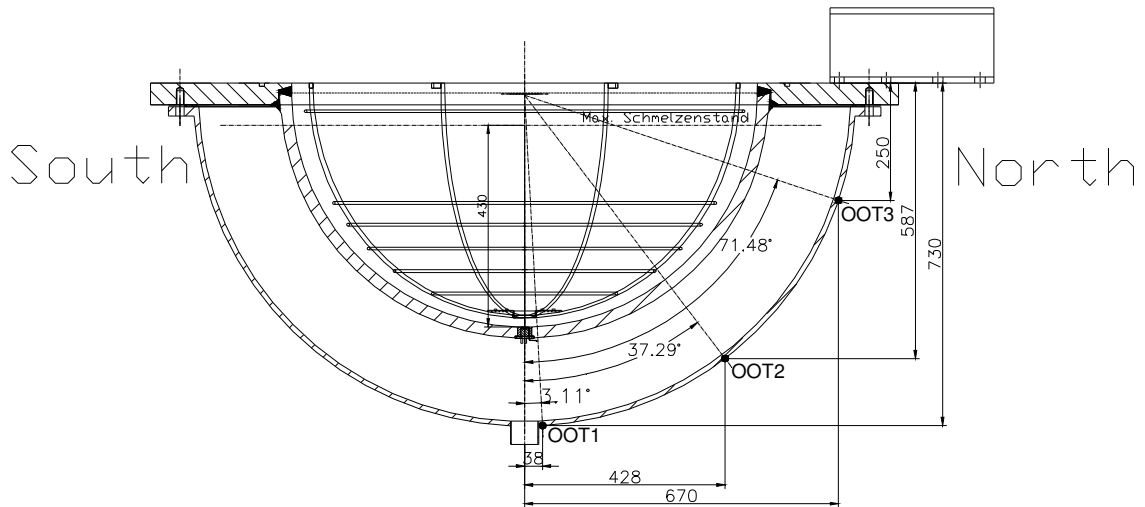
Figure A-11: Positions of the thermocouples at the outer surface of the cooling tank.

Annex B   Test initial conditions and main parameters

Melt characteristics and preparation		
Type	NaNO$_3$	KNO$_3$
Mole %	20 %	80 %
Mass %	17.37 %	82.63 %
Mass	68 kg	324 kg
Total mass	392 kg	
Loading of the furnace	~455 l powder (for T=20 °C) ~210 l melt (for T=350 °C)	
Pouring mass	120 l or 224.4 kg (corresponds to ~31 cm melt height)	
Initial melt temperature	350 °C	
Flow rate of nitrogen flushing	2 l/min	
Melt pour		
Position	lateral	
Number of pours	1	
Furnace tilting velocity	0.5 °/s	
Furnace target angle	76°	
Pouring rate	6 kg/s	
Pouring spout temperature	360 °C	
Phase 1: Homogeneous heat generation with continuous outer vessel wall cooling		
Start time	145 s	
Boundary conditions	water, continuous cooling	
Cooling water flow rate	~0.047 kg/s	
Heating planes	all	
Heating power	10 kW	
Heat generation	homogeneous	
Initial melt temperature	350 °C	
Phase 2: Reduction of heat generation		
Test conditions	reaching of steady-state conditions in phase 1	
Start time	90237 s	
Boundary conditions	water, continuous cooling	
Cooling water flow rate	~0.047 kg/s	
Heating planes	all	
Heating power	7 kW	

Heat generation	homogeneous
Phase 3: Test termination and melt extraction	
End time	181400 s
Test conditions	reaching of steady-state conditions in phase 2
Heating power	switched off

Annex C   Test data

This appendix provides plots of the experimental results. which are not shown in the main part of the report.
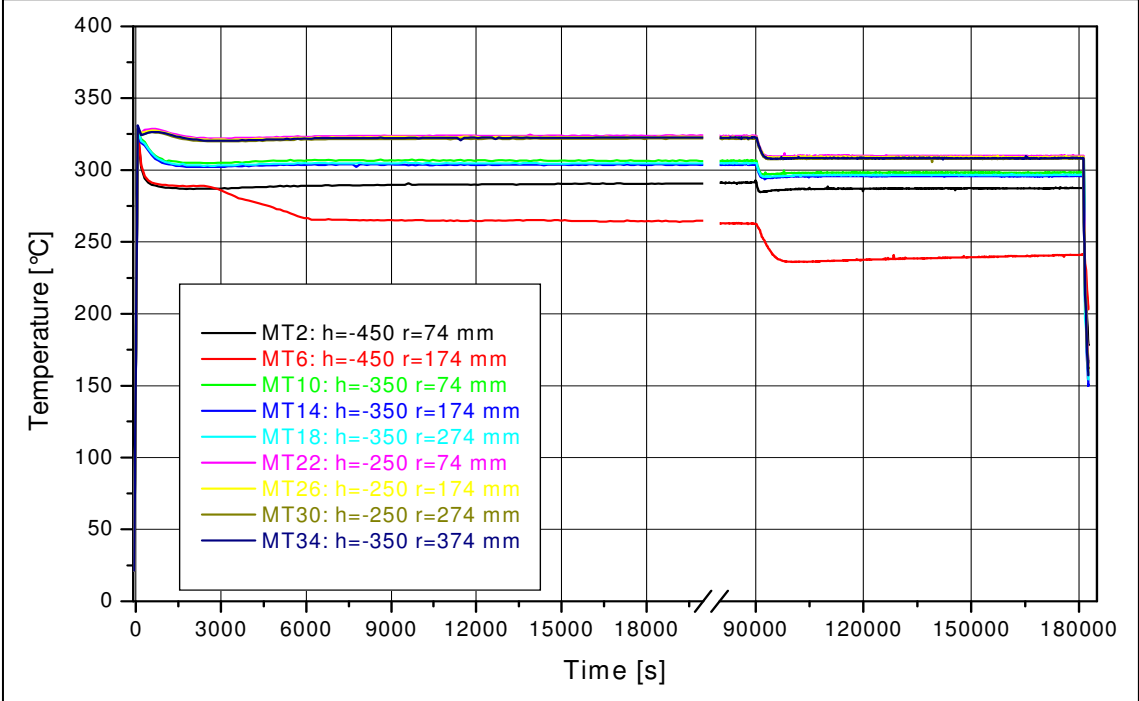
Figure C-1: Melt pool temperatures at different elevations along the meridian at 90° in LIVE-L3A
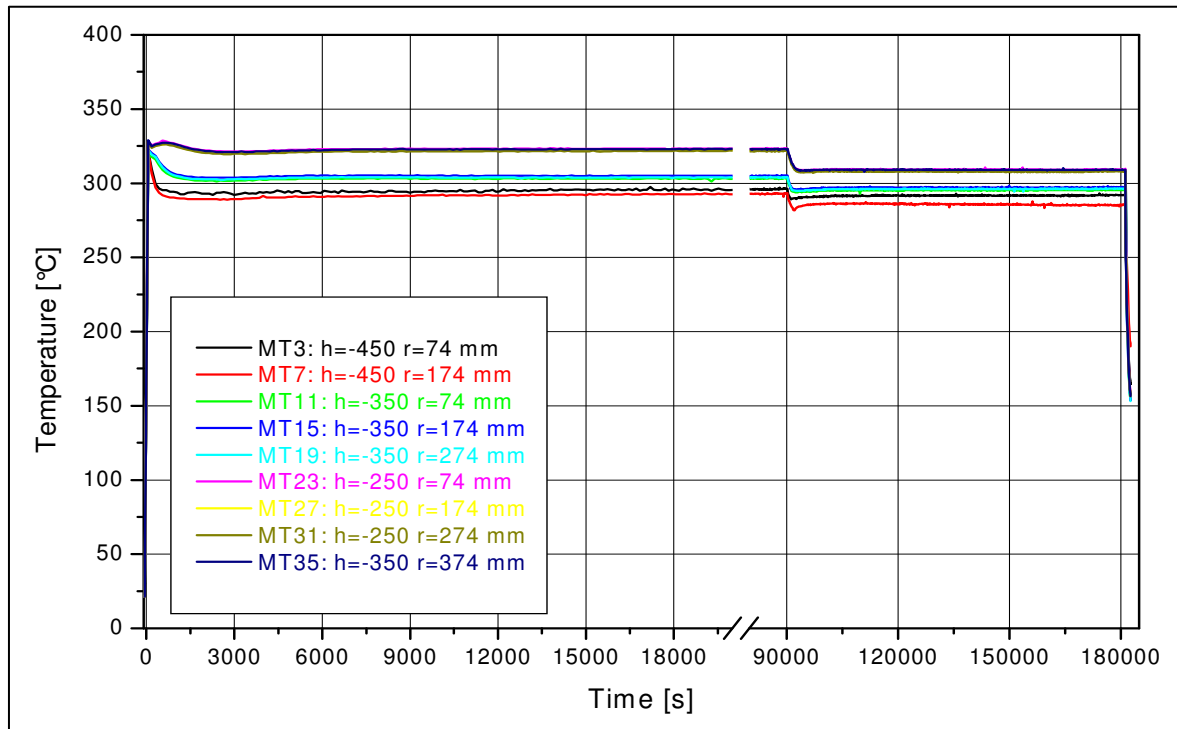
Figure C- 2: Melt pool temperatures at different elevations along the meridian at 180° in LIVE-L3A
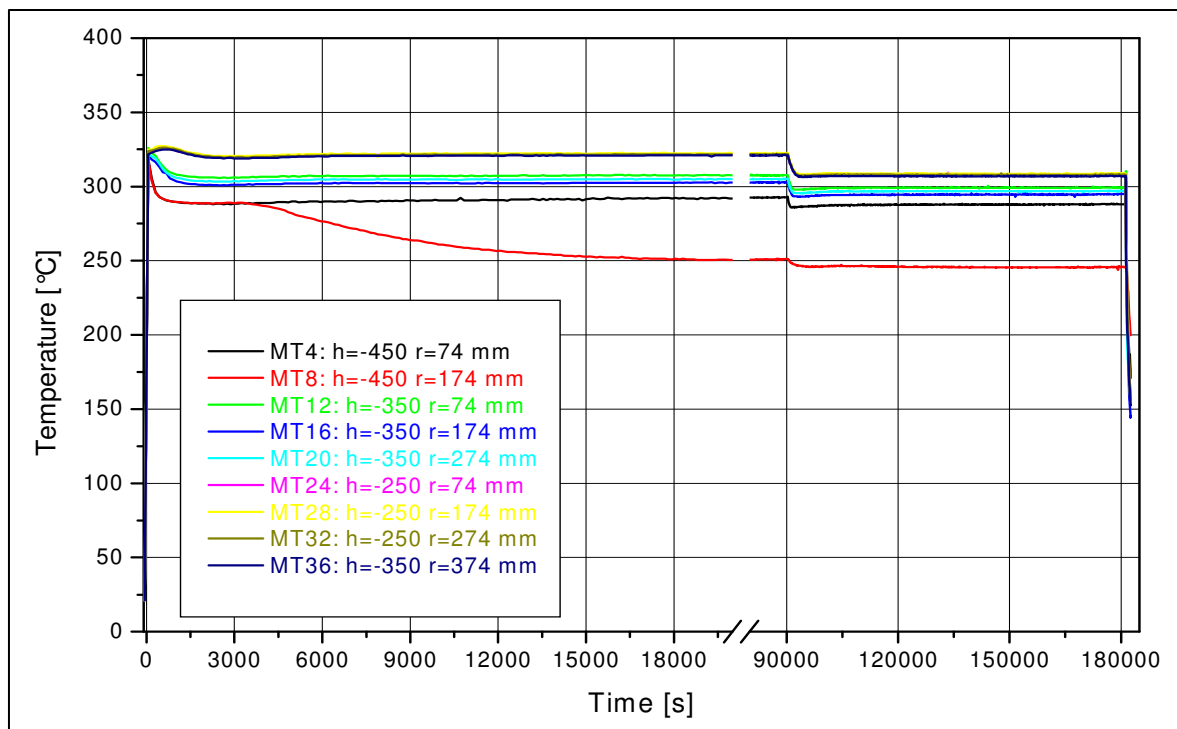
Figure C-3: Melt pool temperatures at different elevations along the meridian at 270° in LIVE-L3A
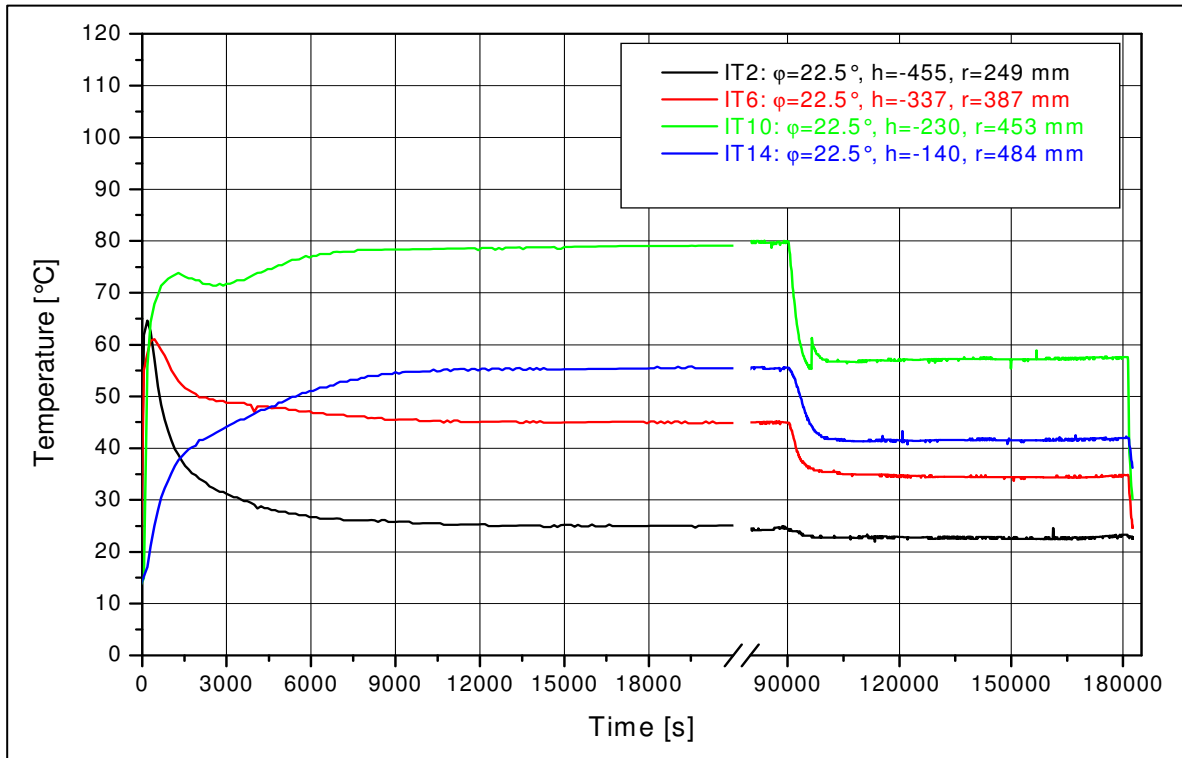
Figure C-4: Inner wall temperatures of the test vessel at different elevations along the meridian at 22.5° in LIVE-L3A
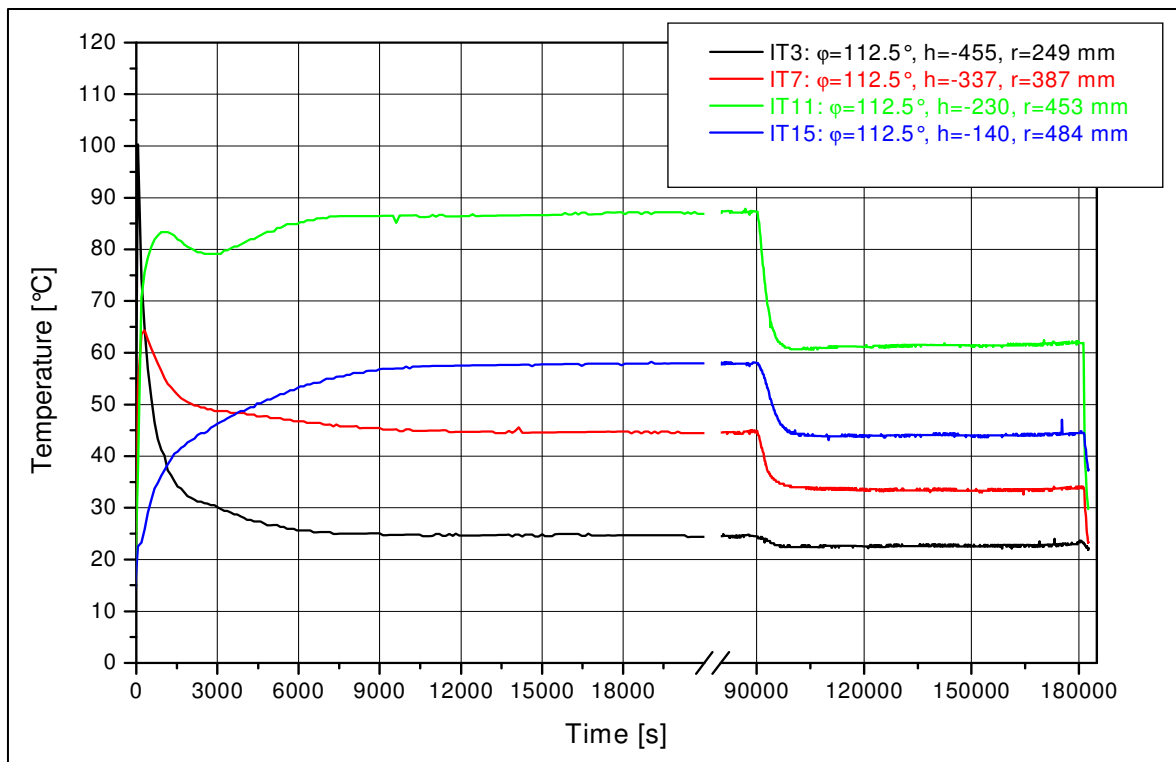
Figure C-5: Inner wall temperatures of the test vessel at different elevations along the meridian at 112.5° in LIVE-L3A
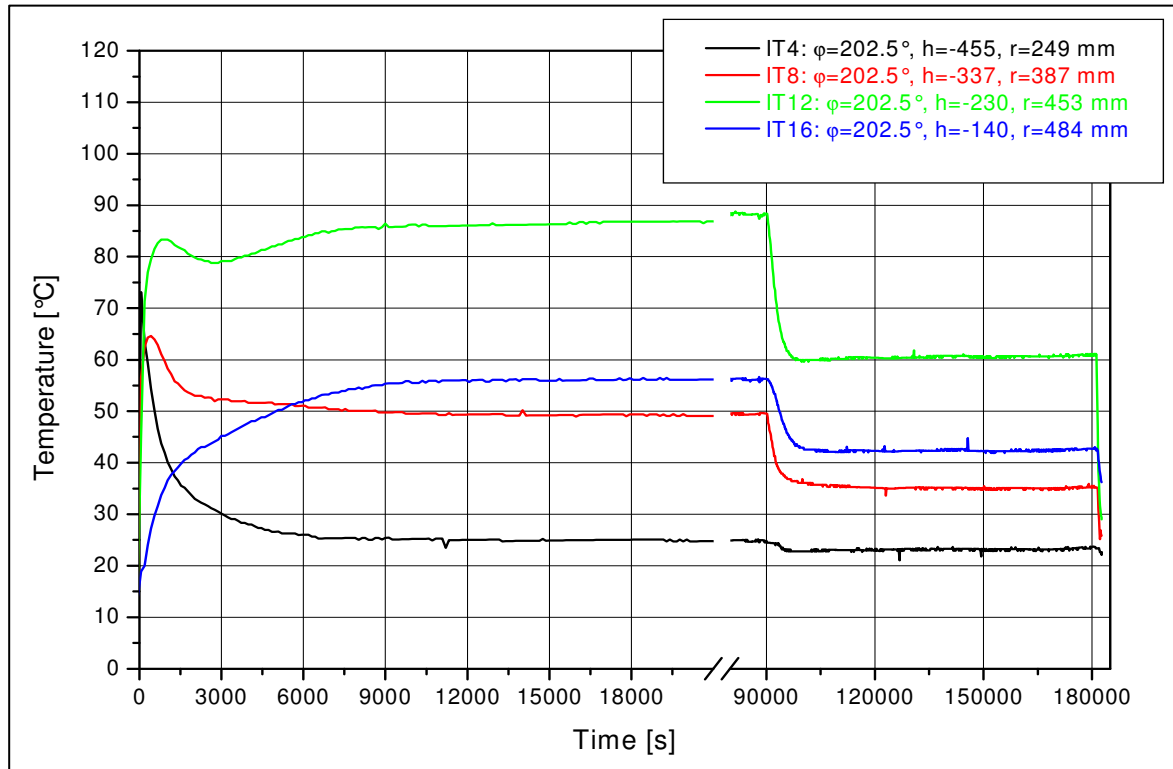
Figure C-6: Inner wall temperatures of the test vessel at different elevations along the meridian at 202.5° in LIVE-L3A
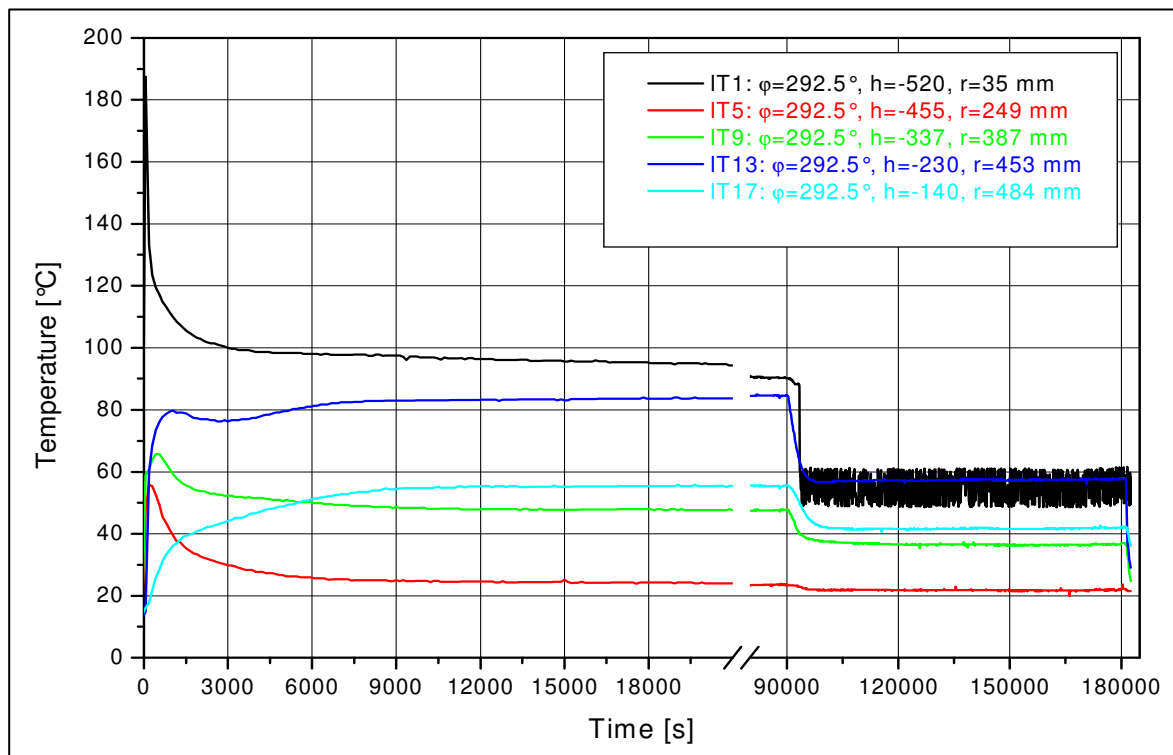
Figure C-7: Inner wall temperatures of the test vessel at different elevations along the meridian at 292.5° in LIVE-L3A
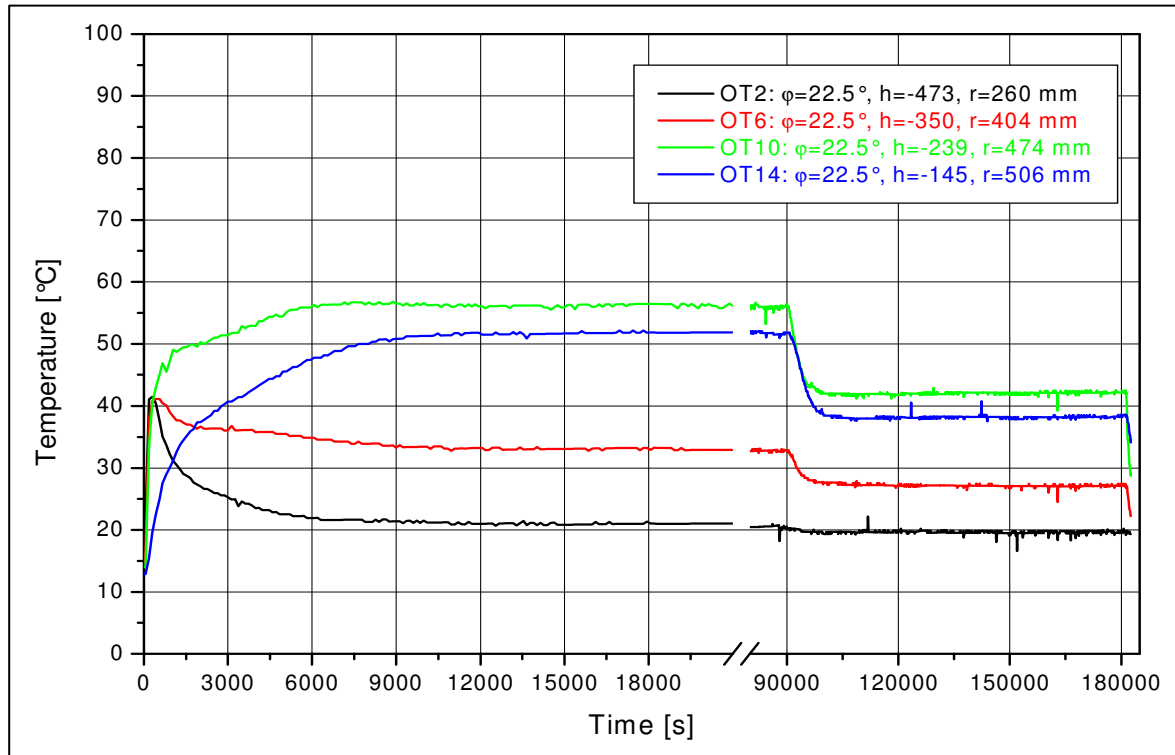
Figure C-8: Outside wall temperatures of the test vessel at different elevations along the meridian at 22.5° in LIVE-L3A
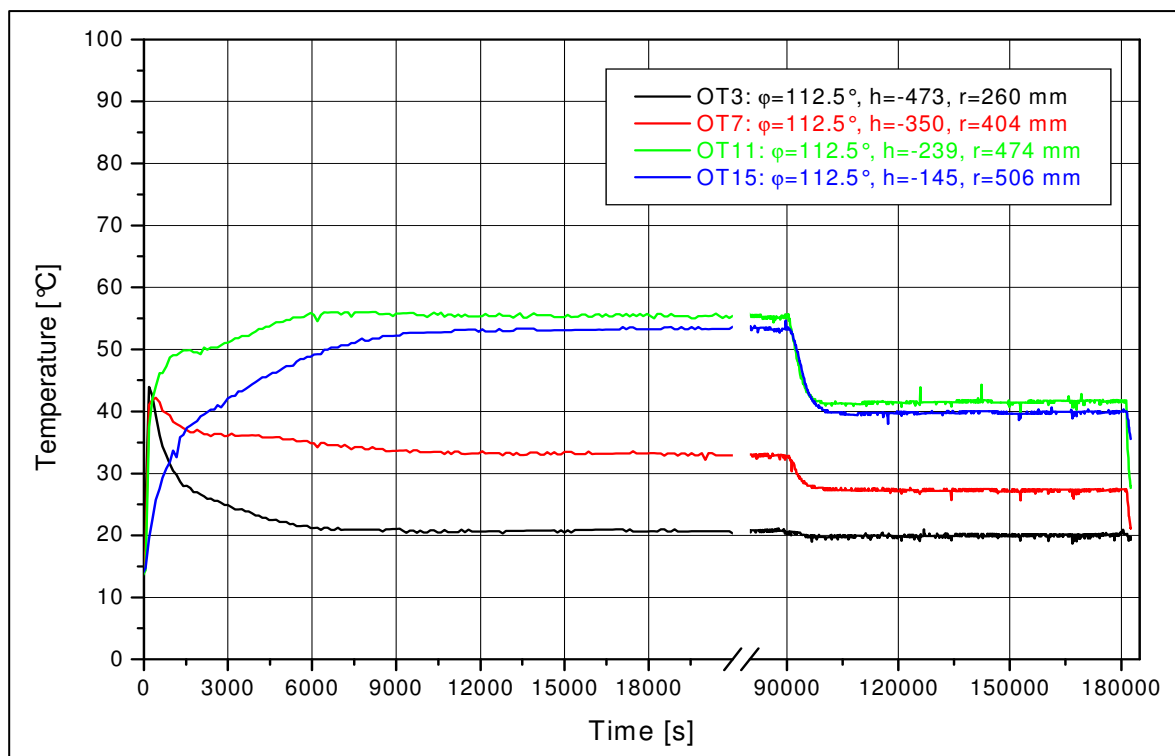
Figure C-9: Outside wall temperatures of the test vessel at different elevations along the meridian at 112.5° in LIVE-L3A
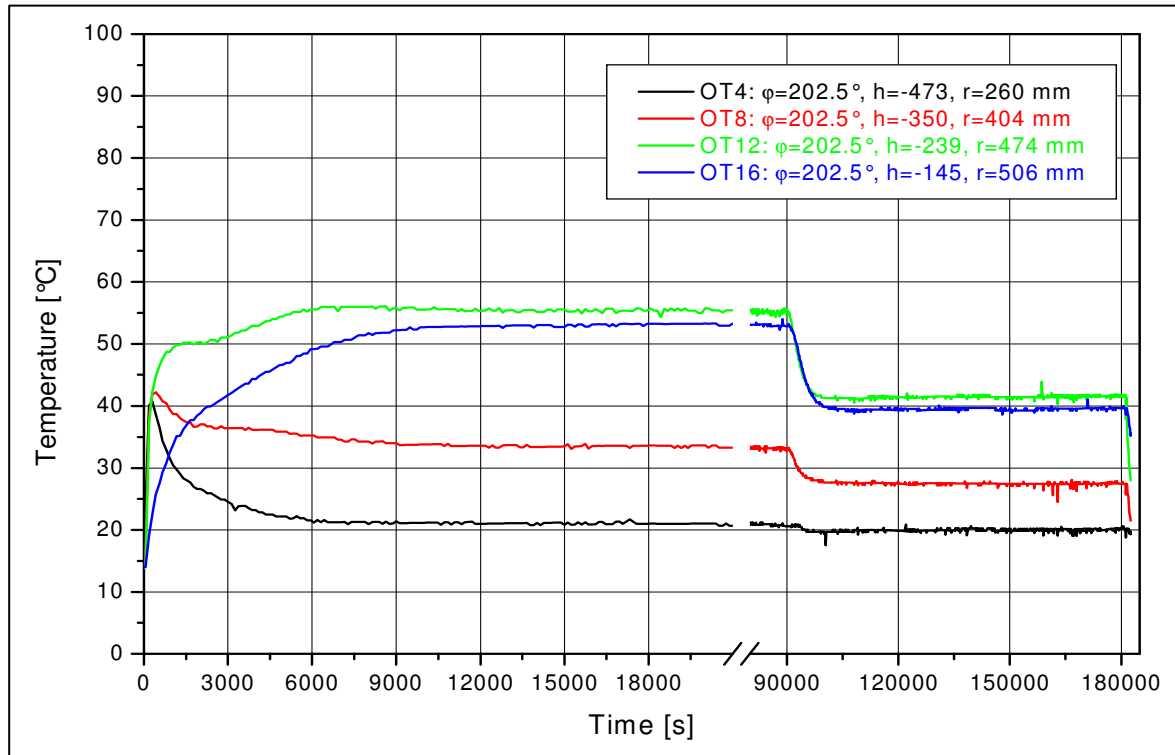
Figure C-10: Outside wall temperatures of the test vessel at different elevations along the meridian at 202.5° in LIVE-L3A
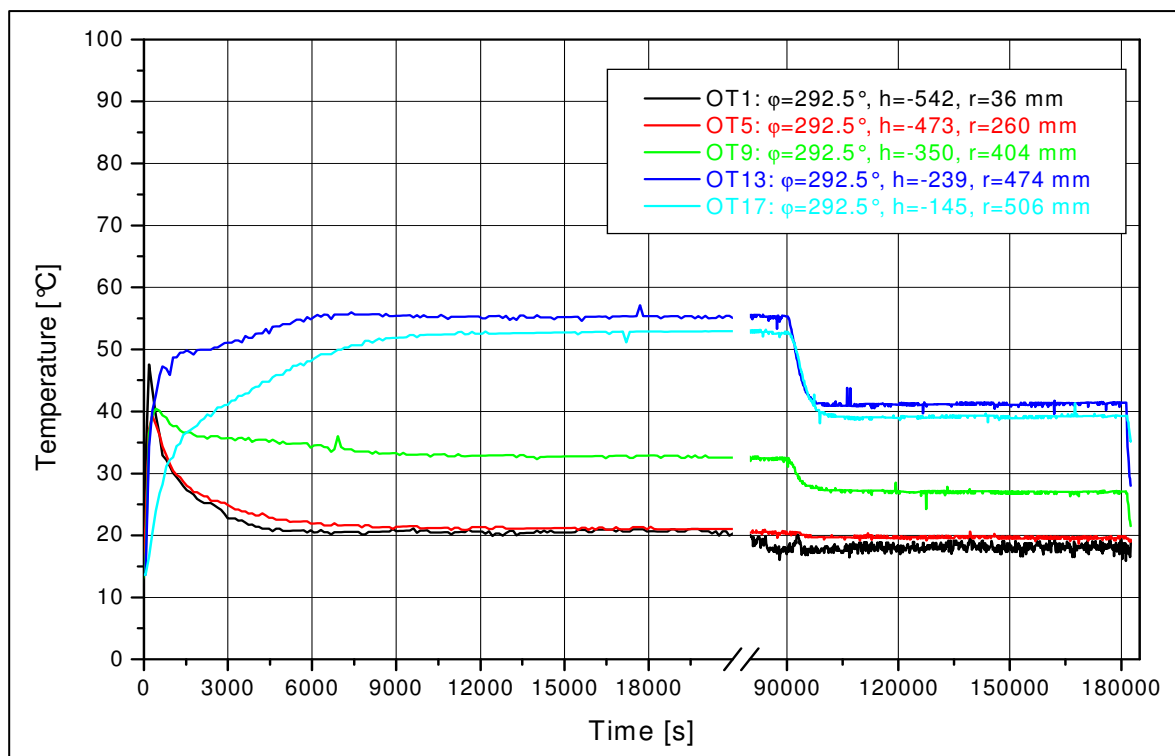
Figure C-11: Outside wall temperatures of the test vessel at different elevations along the meridian at 292.5° in LIVE-L3A
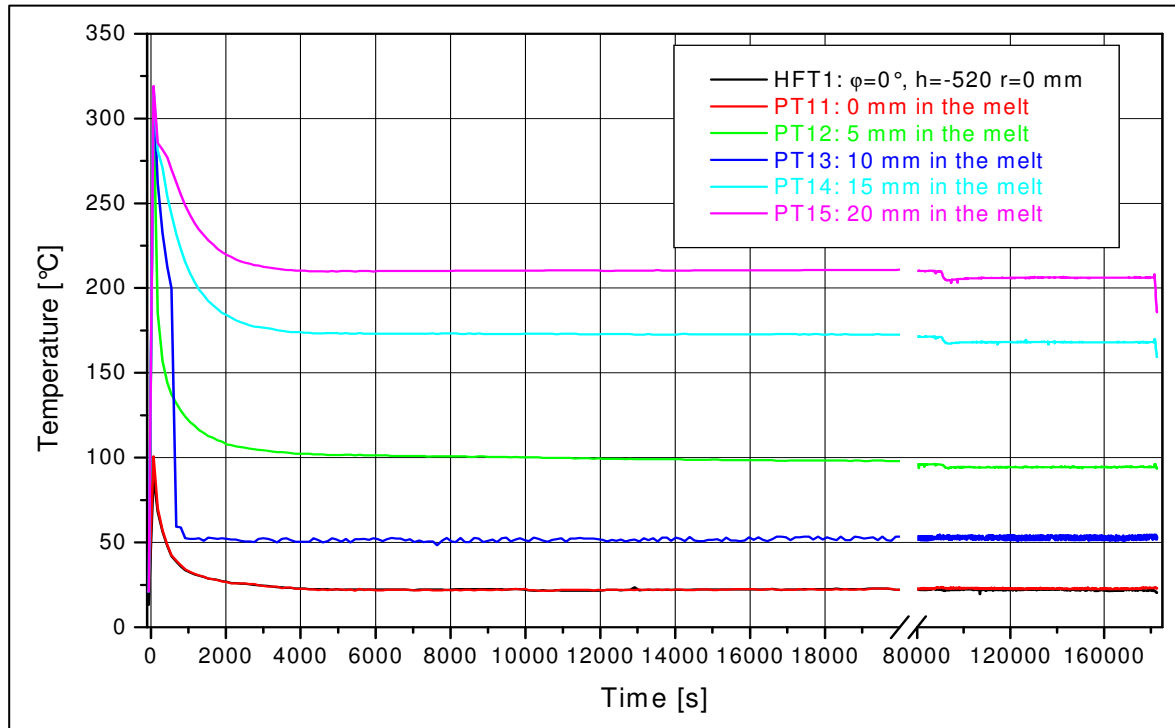
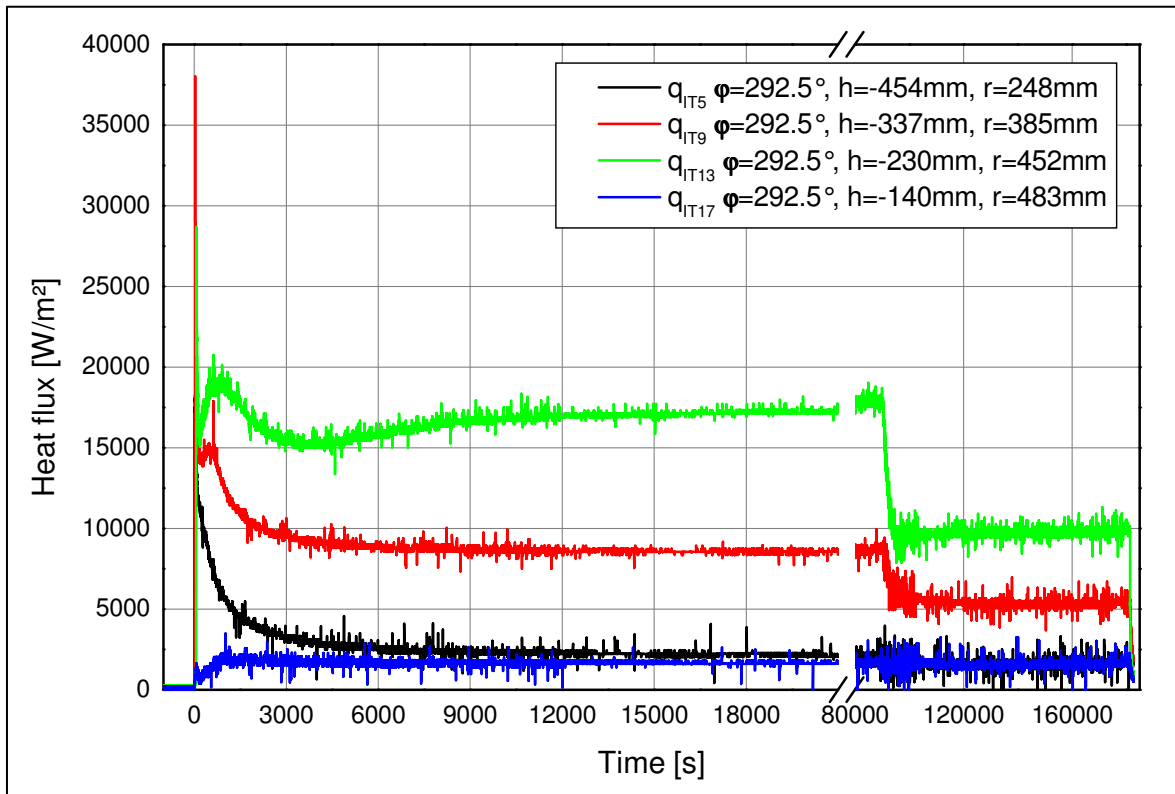Figure C-12: Plug and heat flux sensor temperatures in LIVE-L3A. φ = 0°. h = -520 mm. r=0.
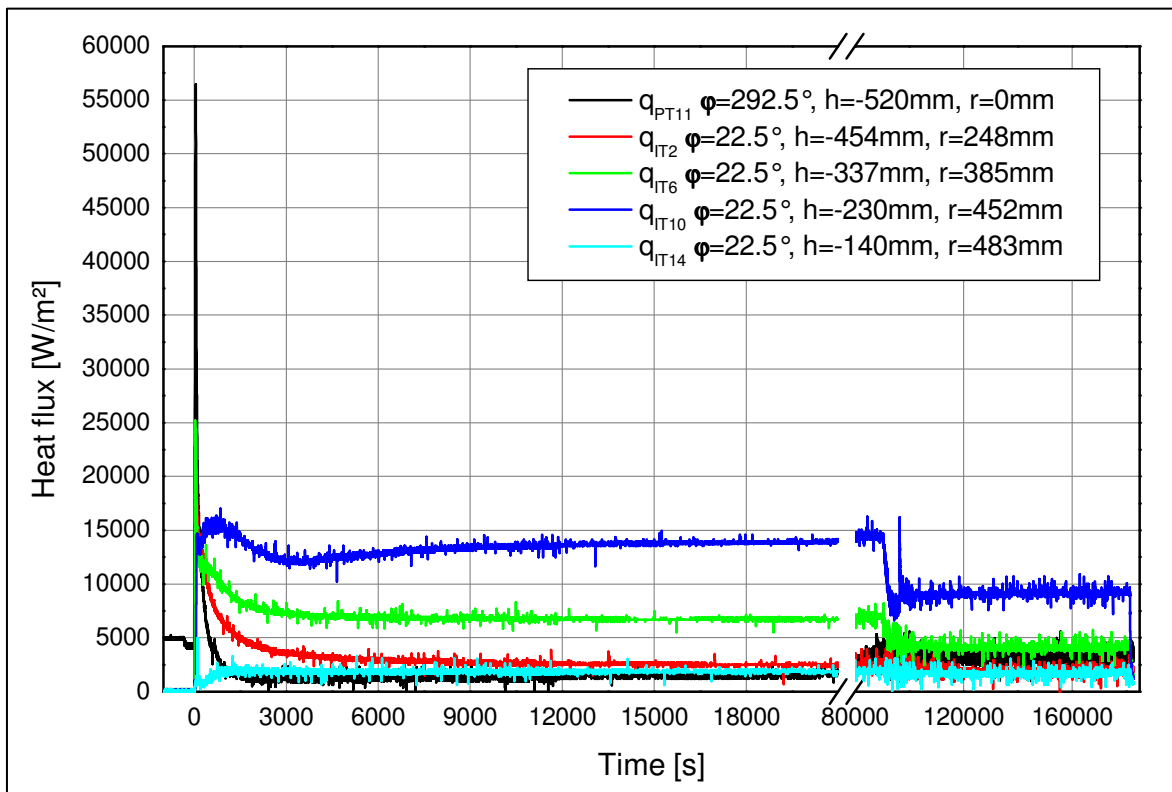
Figure C-13: Heat flux values calculated with IT/OT thermocouples along the meridian at 22.5° in LIVE-L3A
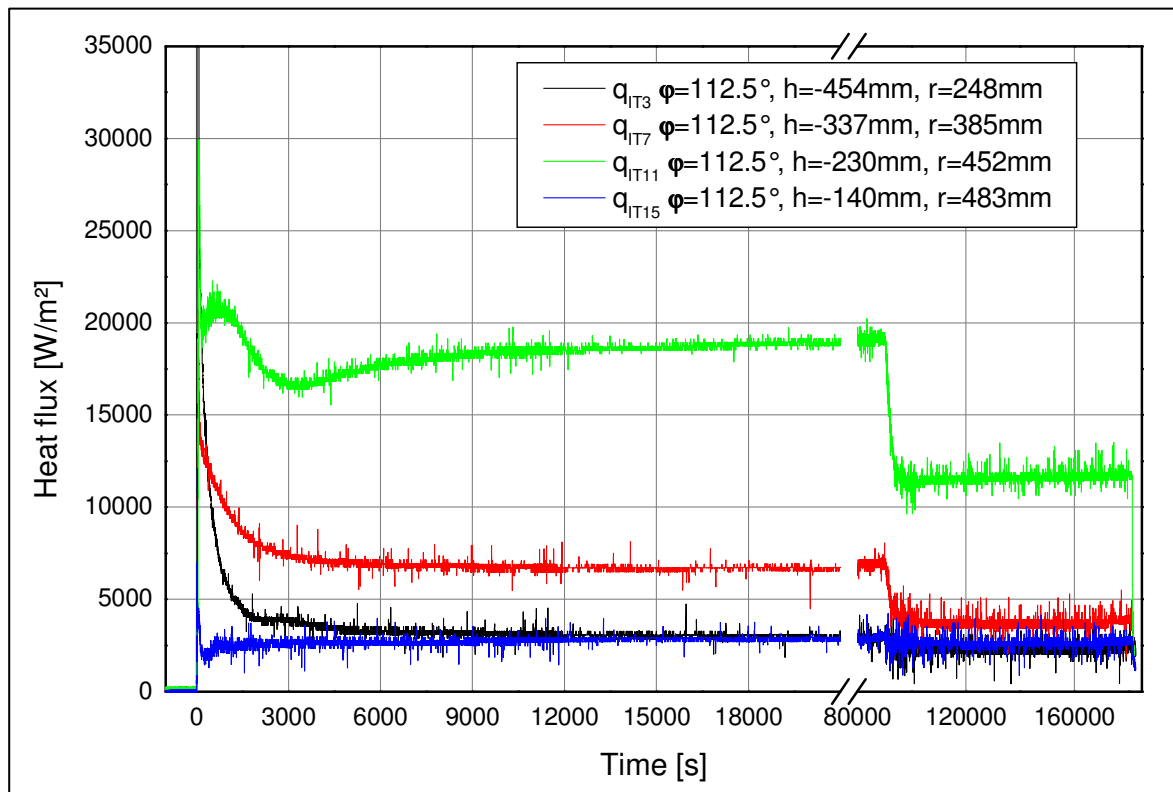
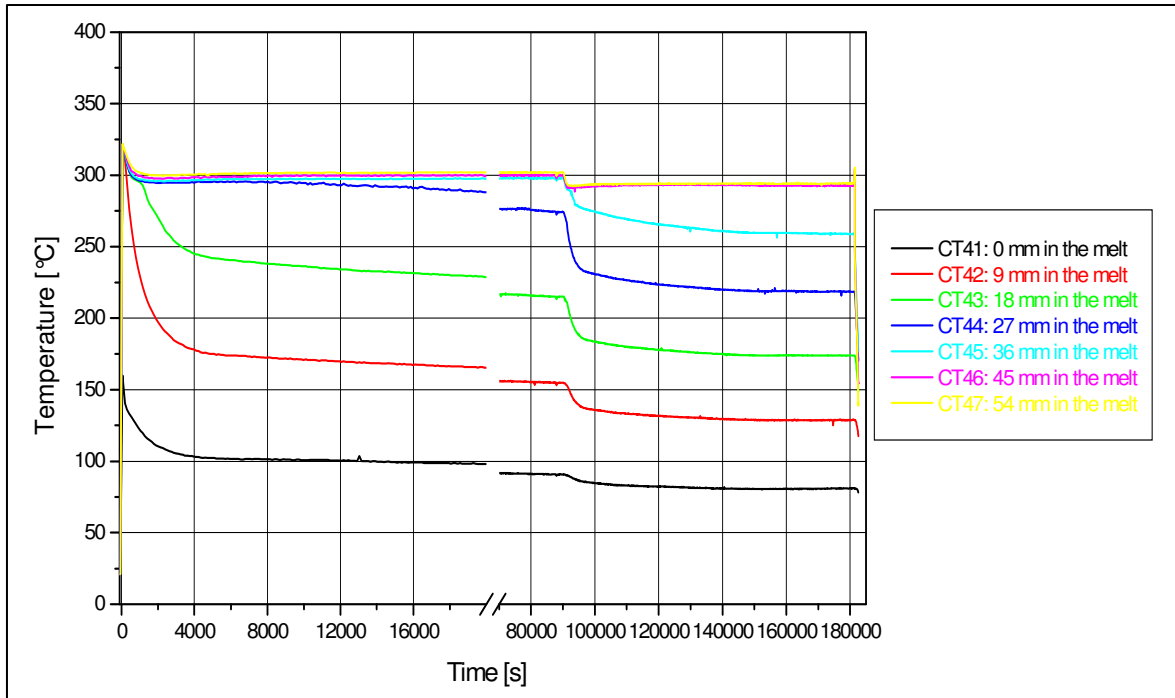Figure C-14: Heat flux values calculated with IT/OT thermocouples along the meridian at 112.5° in LIVE-L3A
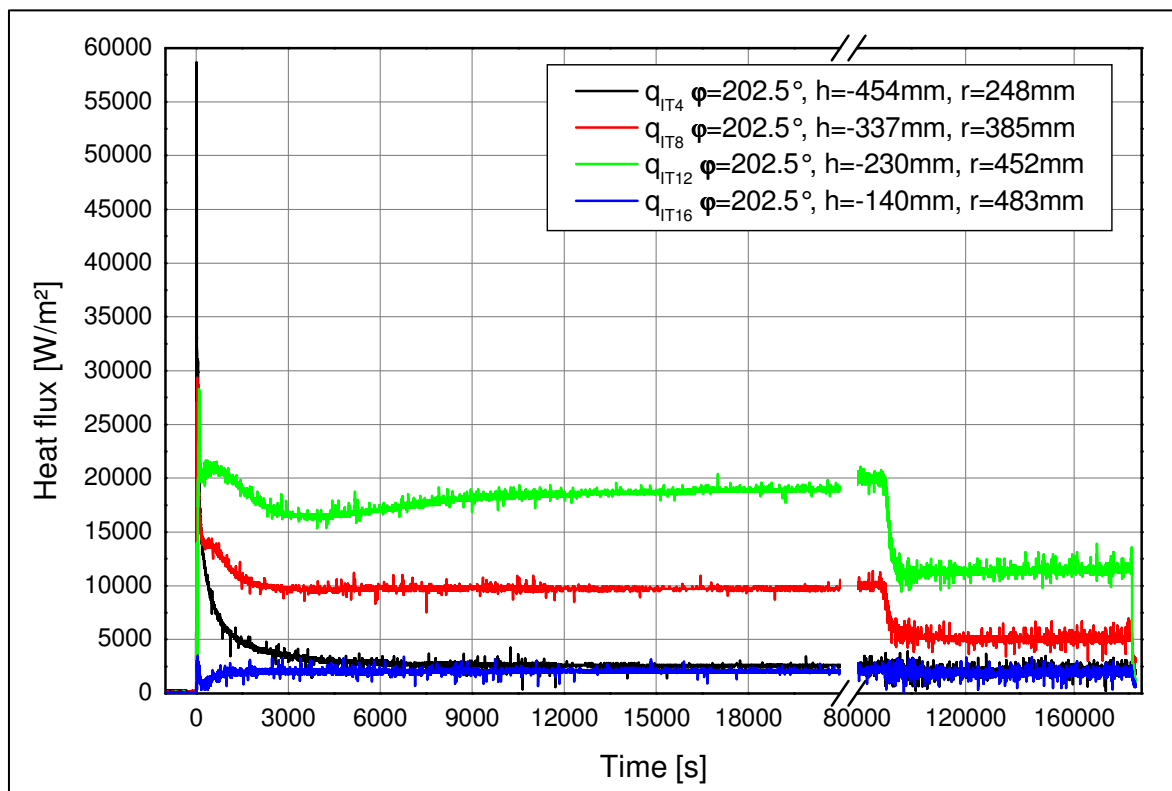
Figure C-15: Heat flux values calculated with IT/OT thermocouples along the meridian at 202.5° in LIVE-L3A

Figure C-16: Heat flux values calculated with IT/OT thermocouples along the meridian at 292.5° in LIVE-L3A

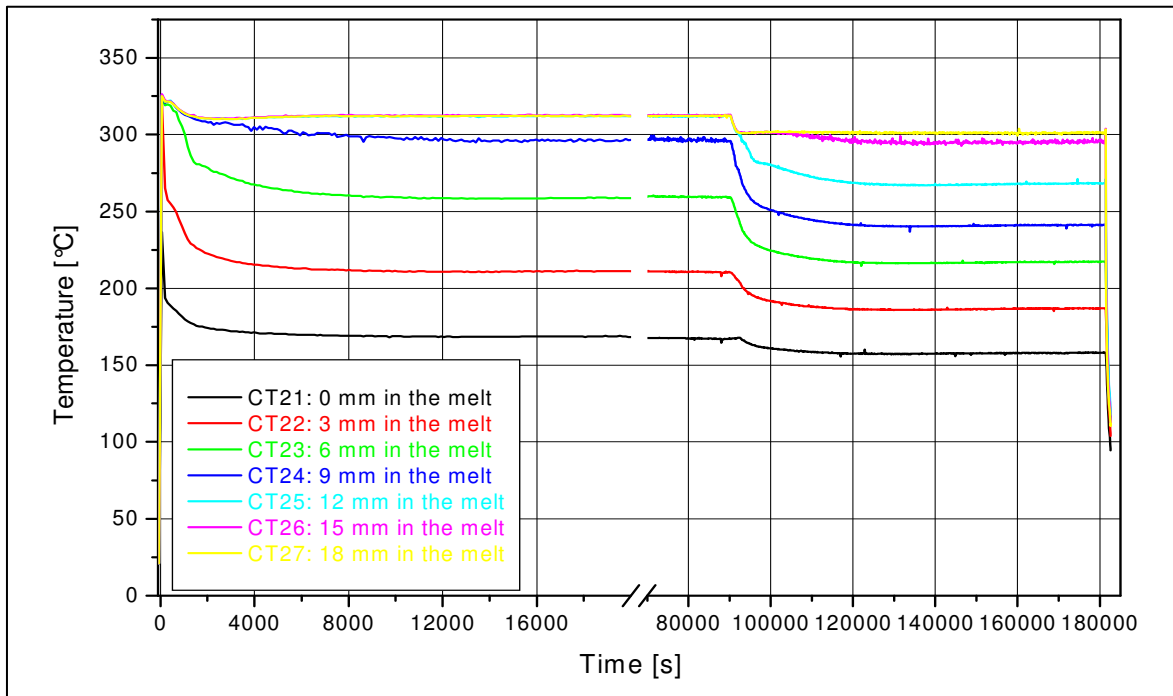Figure C-17: Temperature measurements of the thermocouple tree CT4 in LIVE-L3A. φ = 25°. h = -420.4 mm. r = 299 mm

Figure C-18: Temperature measurements of the thermocouple tree CT2 in LIVE-L3A. φ = 35°. h = -320.4 mm. r = 398 mm
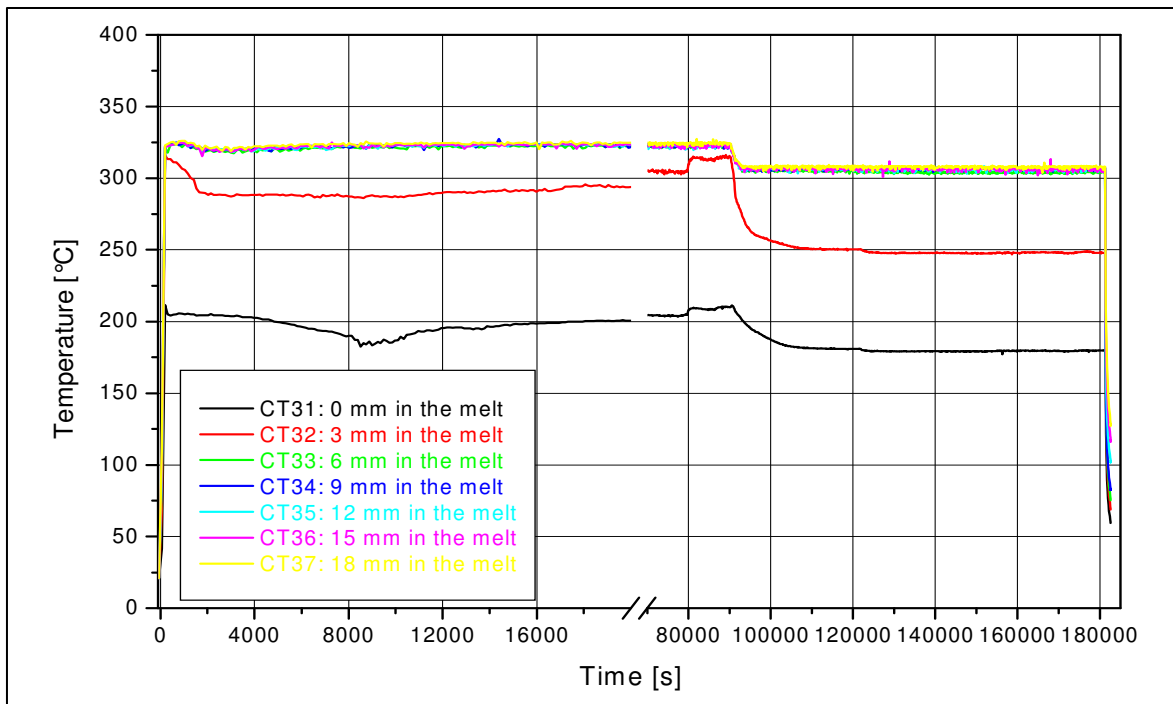

Figure C-19: Temperature measurements of the thermocouple tree CT3 in LIVE-L3A. φ = 35°. h = -220.4 mm. r = 456 mm
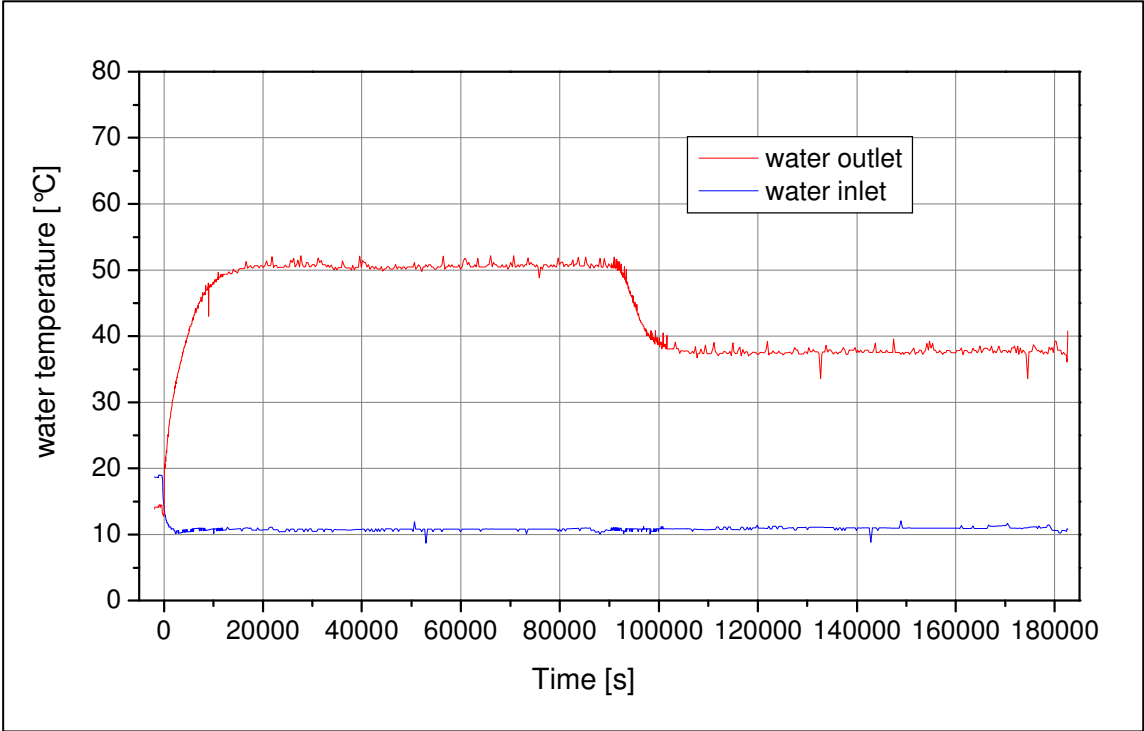
Figure C-20: Cooling water temperatures in LIVE-L3A

The sequence of a postulated core melt down accident in the reactor pressure vessel (RPV) of a pressurised water reactor (PWR) involves a large number of complex physical and chemical phenomena. The main objective of the LIVE program is to study the core melt phenomena during the late phase of core melt progression in the RPV both experimentally in large-scale 3D geometry in supporting separate-effects tests and analytically using CFD codes in order to provide a reasonable estimate of the remaining uncertainty band under the aspect of safety assessment.

The main objective of the LIVE-L3A experiment was to investigate the behaviour of the molten pool and the formation of the crust at the melt/vessel wall interface influenced by the melt relocation position and initial cooling conditions. The test conditions in the LIVE- L3A test were similar to the LIVE-L3 test except the initial cooling conditions. In both tests the melt was poured near to the vessel wall. In the LIVE-L3 test the vessel was initially cooled by air and then by water; in the LIVE-L3A test the vessel was cooled by water already at the start of the experiment.

The information obtained in the test includes horizontal and vertical heat flux distribution through the RPV wall, crust growth velocity and dependence of the crust properties on the crust growth velocity and cooling conditions. Supporting post-test analysis contributes to the characterization of solidification processes of binary non-eutectic melts. The results of the LIVE-L3 and LIVE-L3A tests are compared in order to characterize the impact of transient cooling condition on the crust solidification characteristics and melt pool behaviour including interface temperature, time to reach thermal hydraulic steady-state and the steady-state heat flux distribution.

The report summarizes the objectives of the LIVE program and presents the main results obtained in the LIVE-L3A test compared to the LIVE-L3 test.